

RADBOUD UNIVERSITY NIJMEGEN



FACULTY OF SCIENCE

The Astrophysical Gravitational Wave Background Produced by Merging Extra-Galactic White Dwarf Binaries

INVESTIGATING THE EFFECTS OF METALLICITY AND POPULATION
SYNTHESIS MODEL IN THE LISA FREQUENCY RANGE

THESIS MSc PHYSICS AND ASTRONOMY

Author:

Sophie HOFMAN

Supervisor:

Prof. Dr. Gijs NELEMANS

Student Number:

s1107492

Second reader:

Prof. Dr. Badri KRISHNAN

June 13th, 2024

Abstract

This work aims to show that binary white dwarfs (BWDs) are the dominant component of the astrophysical gravitational wave background (AGWB) detected by LISA, as well as study the effect of metallicity and choice of population synthesis model on the AGWB. This was built on previous work by Farmer & Phinney (2003); Staelens & Nelemans (2024), where the AGWB produced by merging WDs is determined by calculating the GW signal of each system per frequency bin, per redshift. This is repeated for six different metallicities and four different choices for population synthesis model. Moreover, both a metallicity independent and several metallicity dependent star formation rate density (SFRD) models are used. These metallicity dependent SFRD models each have a different total amount of SFRD. The results show that metallicity has a small, but almost negligible effect on the strength of the AGWB. Only one of the population synthesis models ($\alpha\alpha, \alpha = 1$) has a significant effect on the AGWB. The difference between the other three choices are pretty much negligible. The effect of the choice of metallicity dependent SFRD has the largest effect on the AGWB, as expected, since SFRD and AGWB signal increase (or decrease) approximately linearly. Therefore, it is concluded that metallicity and (most) population synthesis model choices only have a trivial effect on the AGWB, and the nature of the SFRD is the most important factor. The usage of different metallicity dependent SFRD models leads to an uncertainty margin of 7.1×10^{-12} in which the full AGWB signal can fall. In LISA's frequency range, and comparing to the AGWB signal of $\gamma\alpha$ with $\alpha = 4$ and the SFRD model MZ19, this leads to an average upper limit of $11.4 \cdot 10^{-12}$ and an average lower limit of $3.48 \cdot 10^{-12}$. Previous research indicates a choice of $\gamma\alpha$ with $\alpha = 4$ and a moderate metallicity dependent SFRD (MZ19) most accurately describes the universe, leading to this signal being the signal most expected to be detected by LISA.

Contents

1	Introduction	4
1.1	White Dwarfs	5
1.1.1	Binary White Dwarfs	6
1.1.2	Metallicity	8
1.2	Gravitational Waves	8
1.3	Gravitational Wave Detectors	10
1.3.1	Laser Interferometer Space Antenna (LISA)	11
1.4	The Astrophysical Gravitational Wave Background (AGWB)	12
1.5	Research Question, Aims and Motivation	13
2	Methods	14
2.1	Determining the AGWB	14
2.1.1	Existing Framework	14
2.1.2	Star Formation Rate	20
2.2	Preparations for Input Data	26
2.3	Population Synthesis	27
3	Results	32
3.1	AGWB Comparison with Previous Work	32
3.2	Effect of Different Population Synthesis Models and Metallicities on the AGWB	34
3.2.1	Comparison Between Models	37
3.3	Effect of a (Moderate) Metallicity Dependent SFRD on the AGWB	41
3.3.1	Comparison Between Models	46
3.4	Comparing Different Types of Metallicity Dependent SFRDs	48
3.4.1	Comparison Between Models	53
3.4.2	Comparison of the Differences Between the SFRDs and the AGWB Signals	55
3.5	Approximation of the Uncertainties	56
4	Discussion	59
4.1	Validity of the Results in this Work	59
4.1.1	Assumptions in this Work	60
4.1.2	Choice of Models	60
4.1.3	Comparison with Previous Work	61
4.2	Measuring the AGWB Cut-Off	63
4.3	Further Research	63

5 Conclusion	64
6 References	65
A Redshift Contribution Figures	71
A.1 Effect of Different Population Synthesis Models and Metallicities on the AGWB	71
A.2 Comparing Different Types of Metallicity Dependent SFRDs	71
B Research Data Management	81

Chapter 1

Introduction

Stars are all around us. The most known, and closest, one is our Sun, which is (often) visible to us during the day. During the night, many more stars are visible, especially when looking at the night sky from a remote location. These stars are much farther away than our Sun, but most of them have properties very similar to our Sun. Currently the Sun is 4.6×10^9 years (or 4.6 Gyr) old, and it is expected that it will stay in this state for the next 7 billion years (7 Gyr). Assuming no drastic changes, it is expected that our Sun (and other Sun-like stars) will at one point end up as white dwarfs (WDs). These stars are similar in mass to our Sun, but their radius has decreased to a size more Earth like. Therefore, WDs are classified as so-called compact objects (other examples of compact objects are black holes (BHs) and neutron stars (NSs)) (Carroll & Ostlie, 2014). It is expected that when two of these compact objects orbit around each other (i.e. are in a binary system together), at one point they can merge. This merger will create a ripple in space-time, a so-called gravitational wave (GW), that can travel unaffected throughout the whole universe, and pass through Earth. Using GW detectors it is possible to observe these ripples (Hartle, 2003). Going back to WDs, it is known that there are lots of WDs both as single stars and in binary systems inside our own Milky Way galaxy¹ and it is expected that there are many more outside our own galaxy. As of today, WD binaries have only been directly detected inside our own galaxy. This means that for this research the binaries will be extrapolated to the whole universe. All WD binary systems merging outside our galaxy are expected to create a single signal that will be observable by one of our future GW detectors, LISA (see e.g. Farmer & Phinney (2003) hereafter FP03 or Staelens & Nelemans (2024) hereafter SN24). LISA will be a space-based GW detector, which will be able to observe different sources compared to the current ground-based GW detectors (Amaro-Seoane et al., 2017). This single signal created by the merging of extra-galactic white dwarfs is expected to be a part of the background signal that LISA will detect.

This thesis aims to investigate the astrophysical gravitational wave background (AGWB)² produced by the mergers of extra-galactic WDs. In particular, the effects of metallicity and a different choice of formation model of BWDs will be explored. Therefore, first the formation and evolution, as well as the characteristics, of WDs will be explained, both as a single star and as a binary system. For the binary system different types of mass

¹For instance, relatively recently, Gaia EDR3 found approximately 360000 objects that have a probability of more than 75 percent of being a WD (see Gentile Fusillo et al. (2021) for more details).

²This is the gravitational wave background solely produced by astrophysical sources.

transfer need to be introduced, as these are some of the different parameters that will affect the formation of the BWD system. Afterwards, the concept of metallicity will be explained in detail, since this is also one of the effects that will be investigated in this thesis. Furthermore, since this thesis aims to investigate the AGWB, a brief introduction on GWs and GW detectors will be given. Subsequently, the specific (space-based) GW detector, LISA, that will detect the AGWB generated by merging extra-galactic WDs, will be explained. Then, the AGWB and its potential sources that will be touched upon thoroughly. Lastly, the research question and aims of this thesis will be explained in detail.

1.1 White Dwarfs

Our universe consists of approximately 10^{22} to 10^{24} stars (ESA, 2024b). These stars have a variety of masses that can go up to more than 100 solar masses (M_{\odot}) (e.g Figer (2005)). After evolving for a significant amount of time, there are multiple ways stars can come to an end. Stars with masses of $8M_{\odot}$ or lower, encompassing approximately 95-98 percent of the stars in our universe, end up as white dwarfs (WDs). The other percentage of stars, those with masses larger than $8M_{\odot}$, end up as either NSs or BHs (Koester, 2002).

The process of forming a WD starts from a point where roughly 90 percent of the stars, including our own Sun, currently reside, namely on the main sequence. A star is said to be on the main sequence when hydrogen (H) gets fused into helium (He) in its core leading to the generation of thermal energy (Carroll & Ostlie, 2014). Afterwards, when all H has been fused into He, He gets fused into carbon (C) and oxygen (O). The star then loses most of its outer layers as a consequence of extreme mass-loss phases, leaving behind only the carbon-oxygen (CO) core with an extremely thin H and He envelope (Althaus et al., 2010). Having no fuel anymore for the burning of elements, the core cools down, becoming a WD. It should be noted that not all WDs have the above described structure, since roughly 20-25% of all WDs do not have a significant or even any amount of H in their envelope. Furthermore, WDs with progenitor masses near $10M_{\odot}$, may reach high enough temperatures to be able to burn some of the carbon in the core, leading to an oxygen-neon (ONe) WD. However, on the other hand, WD progenitors with relatively low masses (smaller than $0.6M_{\odot}$) or stars in binary systems, might end up as a helium core WD, since their evolution stops before these stars can start fusing He in their cores (Saumon et al., 2022).

The masses of WDs range between the lowest observed mass of a WD of about $0.17M_{\odot}$ (Kilic et al., 2007) and an upper limit, an idea first postulated by Chandrasekhar (Chandrasekhar, 1931), of approximately $1.4M_{\odot}$ (Takahashi et al., 2013). In general, most WDs have the following characteristics: a mass of roughly $0.6M_{\odot}$ and a radius of roughly $0.013R_{\odot}$, where R_{\odot} represents the solar radius. This shows that WDs have a very high density (ρ) of about 10^6 g/cm³. These specific circumstances lead to the matter in the star being ionised as well as the electrons in the star becoming entirely degenerate. The reason why the WD does not collapse under its own gravity, is because of the counteracting pressure of these degenerate electrons. (Saumon et al., 2022).

1.1.1 Binary White Dwarfs

Occasionally, two WDs orbit each other in a binary system. The main formation channel is thought to start with two main sequence stars in a binary system, which individually, in this case meaning one after another, go through the process described in Section 1.1, and become a WD. Comparison of theory and observations has shown that to create the binary white dwarfs (BWDs) currently observed, the binary system must have lost the mass of its envelope two times, when each of the WDs went through the giant phase (Woods et al., 2011). This giant phase occurs when the star leaves the main sequence. Depending on the mass of the star different scenarios can occur during this phase, but the main effect is that the star's envelope, the region of the star around its core, expands (Carroll & Ostlie, 2014).

After one of the stars has already become a WD, the second mass transfer phase commences. During the second mass transfer stage, the initial secondary star of the system (the star with an initial lower mass) has to become a WD through a process known as the common envelope phase (Woods et al., 2011). To be able to fully understand the common envelope phase, first a concept called the Roche lobe needs to be explained. A Roche lobe is a tear-shaped volume surrounding a star. A binary system thus consists of two Roche lobes, for each of the two stars, leading to a figure eight shape (Carroll & Ostlie, 2014). A common envelope is created when the primary star has filled its Roche lobe and starts transmitting its mass to the secondary star in the system. This happens through the point (a Lagrangian point) where the two Roche lobes of the two stars meet. However, when the secondary is not able to fully accrete all the material it receives, the material piles up in a bubble of gas around the secondary. At some point, even the primary gets submerged in this bubble, which is described as the common envelope phase (Iben & Livio, 1993). It is thought to be the process which can significantly decrease the orbital separation of binaries (Livio & Soker, 1988). While the common envelope phase in WD binaries is occurring, large amounts of mass and orbital angular momentum are lost from the system (Taam & Ricker, 2010).

The difference in formation model for the BWDs, implied at the beginning of this thesis since this thesis aims to investigate different possibilities, comes from the first mass transfer phase. The second mass transfer phase is generally accepted as being described by the α -formalism, which will be explained in detail shortly. However, there is more discussion regarding the first mass transfer phase. Some believe that the first and second mass transfer phases both undergo the so-called α -formalism. However, there are two possible types of mass transfer processes that can occur that might lead to the observed BWD systems. The second possibility, aside from the α formalism, is the γ formalism.

The concept of the α -formalism was long thought to be the formalism accurately describing the formation of BWDs (Webbink, 1984). This concept uses the conservation of orbital energy as its starting point. In the form of an equation this can be expressed as:

$$E_{gr} = \alpha(E_{orb,init} - E_{orb,final}) \quad (1.1)$$

where α is the efficiency parameter, describing how efficient the process is of using the orbital energy to remove the common envelope, E_{orb} is the orbital energy and E_{gr} is the

binding energy, which can be defined as:

$$E_{gr} = \frac{GM M_{env}}{\lambda R} \quad (1.2)$$

where λ is a parameter characterising the structure of the envelope of the red giant and R is the radius of the donor (or primary) star.

The second possibility is the γ formalism, which states that the first mass transfer phase should, again, be unstable and non-conservative. This formalism declares that the angular momentum of a binary system is decreased by the mass loss as follows:

$$\frac{J_{init} - J_{final}}{J_{init}} = \gamma \frac{\Delta M}{M + m} \quad (1.3)$$

here, J_{init} and J_{final} are the angular momenta, where the initial angular momentum (J_{init}) describes the system before mass transfer occurred and the final angular momentum (J_{final}) describes the system after mass transfer has occurred. In the case of the γ formalism describing the first mass transfer case, this mass transfer phase is thought to be the result of the ejection of the common envelope, without the binary going through a spiral-in phase. In other words, the orbital separation before and after the first phase of mass transfer is thought to only have decreased slightly. It is even thought that the γ formalism could actually lead to widening of the orbit. For the α formalism, the orbit always shrinks (Toonen et al., 2012). As the second, and last, mass transfer phase has to be a spiral-in phase. Some possible energy sources that could lead to the removal of the envelope are the luminosity of the giant or tidal heating (Nelemans et al., 2000).

The parameter γ is assumed to be somewhere in the range between ~ 1.4 and ~ 1.7 (Nelemans et al., 2000). The exact numerical value for α is a bit more unclear. Formally, α should have a numerical value somewhere between 0 and 1, as it is impossible to use more energy than is generated. However, due to the complexity of the α -formalism, some authors argue that the numerical value of α can actually be larger than 1. The reason for this is that since this common envelope phase is so complex, a relatively simple explanation (the α -formalism) might not be able to accurately describe the process happening in nature and there might be extra factors contributing to the common envelope process (see e.g. Iben & Livio (1993) for a list of factors that could lead to a value for α larger than 1). One thing that is clear about the α formalism is that a larger numerical value for α means a wider orbit of the binary system.

After both main sequence stars in the binary have evolved to a WD, resulting in a BWD, some of these systems will merge. In our Milky Way, it has been established that the amount of BWDs that merge within the Hubble time (the age of the universe, 13.7 Gyr) is roughly $(5-7) \times 10^{-13} \text{ yr}^{-1} \text{ M}_\odot^{-1}$ (Maoz & Hallakoun, 2017; Maoz et al., 2018). This would lead to a local cosmic merger rate of approximately $(5-7) \times 10^5 \text{ Gpc}^{-3} \text{ yr}^{-1}$ (Sousa et al., 2023).

1.1.2 Metallicity

In general, there are three factors that affect the evolution of stars: the star's initial mass, it's metallicity (Z) and it's rotation rate. Other factors that have an effect on the evolution are magnetic fields and if the star is a part of a close binary system (Hirschi et al., 2007). In this thesis, the metallicity of the universe is the factor that will be investigated. Metallicity is often defined as the mass fraction Z , of heavy elements. This is made up of all the elements starting from carbon. These elements are often referred to as "metals", although not all elements are actually officially classified as metals. For example, here, metals also include elements like nitrogen and oxygen (Pagel, 2009). Representing the definition for Z in the form of an equation gives the following expression (Equation 1.4):

$$Z = \frac{M_{\text{metals}}}{M_{\text{baryons}}}. \quad (1.4)$$

This equation (Equation 1.4) is generally used in theory, however, in observational studies a different definition is used, as seen in the following expression:

$$Z_{O/H} = 12 + \log(O/H) \equiv 12 + \log(n_O/n_H) \quad (1.5)$$

where the n represents the number density of oxygen (O) and hydrogen (H), respectively. Converting between solar abundance ratios and the required abundance ratio, can be done in the following manner:

$$\log(Z/Z_\odot) = Z_{O/H} - Z_{O/H_\odot}. \quad (1.6)$$

Nonetheless, it should be noted that the values for both solar abundances and solar metallicity are unidentified as of yet and there are many different ways of determining these values, each giving slightly different results. In this thesis the value by Anders & Grevesse (1989) is used as the solar abundance, which is equal to $Z_{O/H_\odot} = 8.83$.

Metallicity is an important factor to consider since at star forming regions at different redshifts, stars with varying metallicities are created. In other words, not every region in our universe has stars with the same metallicity. Therefore, knowledge of the metallicity of different regions in the universe is essential (see e.g. Chruścińska & Nelemans (2019) and references herein).

1.2 Gravitational Waves

This section is based on the book: *Gravity: An Introduction to Einstein's General Relativity* (Hartle, 2003). Mass produces curvature in spacetime, and when its in motion, it is the source of so called ripples of curved spacetime. These ripples, moving at the speed of light, are called gravitational waves (GWs). This concept of GWs was first postulated by Albert Einstein, when he came up with his theory of general relativity. Some physical sources, which produce these GWs are for example binary systems, supernovae explosions and stars collapsing to a BH. In the simplest case, the GW propagates in one direction, the longitudinal direction, and is independent of the other two directions, the transverse directions.

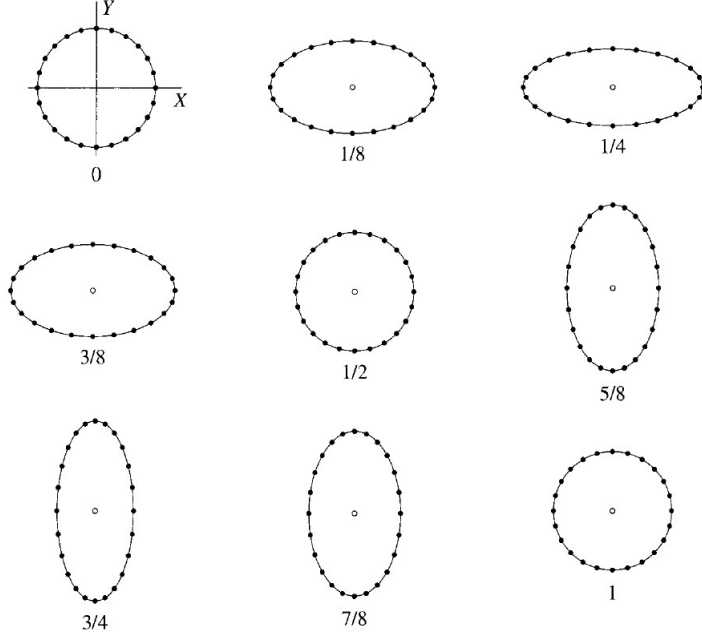


Figure 1.1: Signature of a GW.(Hartle, 2003).

The metric of a flat spacetime, in an inertial frame with coordinates (t, x, y, z) is described as seen in Equation 1.7:

$$g_{\alpha\beta}(x) = \eta_{\alpha\beta} \text{ with } \eta_{\alpha\beta} = \text{diag}(-1, 1, 1, 1). \quad (1.7)$$

Metrics that are close to flat spacetime, have an extra term in this formula:

$$g_{\alpha\beta}(x) = \eta_{\alpha\beta} + h_{\alpha\beta}(x). \quad (1.8)$$

The term $h_{\alpha\beta}(x)$ is the small perturbations to the metric of a flat spacetime, which describes the GW. Using a simple example where the GW is propagating in the z -direction, the following $h_{\alpha\beta}$ is defined:

$$h_{\alpha\beta}(t, z) = \begin{pmatrix} 0 & 0 & 0 & 0 \\ 0 & 1 & 0 & 0 \\ 0 & 0 & -1 & 0 \\ 0 & 0 & 0 & 0 \end{pmatrix} f(t - z). \quad (1.9)$$

In this formula, the function $f(t - z)$ describes the amplitude and shape of the GW. The only requirement is that $|f(t - z)| \ll 1$.

The GW metric does not alter the distance between test masses that are situated in the longitudinal direction (z -axis). Similarly to electromagnetic waves, transverse directions are the only directions affected by the GW, meaning that GWs are transverse, as well. The signature of a GW can best be described by an image (Figure 1.1).

In this figure, 24 test masses are placed around a mass at the origin and the term $f(t - z)$ is set equal to $a \sin[\omega(t - z)]$. This expresses a GW with an amplitude a and a frequency ω . The amplitude of the GW is set to 0.8, in this case. This figure only shows one of the possible polarisations of GWs. The second possible polarisation of a GW would have

a similar signature, but it would be rotated by 45° . The term $h_{\alpha\beta}(x)$ for this second polarisation would be:

$$h_{\alpha\beta}(t, z) = \begin{pmatrix} 0 & 0 & 0 & 0 \\ 0 & 0 & 1 & 0 \\ 0 & 1 & 0 & 0 \\ 0 & 0 & 0 & 0 \end{pmatrix} f(t - z). \quad (1.10)$$

The first polarisation (1.9) is known as the plus (+) polarisation, the second polarisation (1.10) is known as the cross (\times) polarisation. This leads to the following formula describing the general linearized GW:

$$h_{\alpha\beta}(t, z) = \begin{pmatrix} 0 & 0 & 0 & 0 \\ 0 & f_+(t - z) & f_\times(t - z) & 0 \\ 0 & f_\times(t - z) & -f_+(t - z) & 0 \\ 0 & 0 & 0 & 0 \end{pmatrix}. \quad (1.11)$$

1.3 Gravitational Wave Detectors

There are two main ideas that have been used to detect GWs. The first idea builds on the fact that GWs can oscillate a resonant bar. The amplitude of these oscillations is then measured (Weber, 1960). The second idea, perhaps the most well known type of GW detector, uses interferometry and measures the variations in space-time geometry detected by free falling test masses. The free falling masses are often represented as the mirrors of the interferometer. These interferometers have arms with lengths of kilometres, with the most well known examples being the Laser Interferometer Gravitational-Wave Observatory (LIGO) (B. Abbott et al., 2004), Virgo (Accadia et al., 2012) and the Kamioka Gravitational Wave Detector (KAGRA) (Aso et al., 2013). The lengths of the arms of the GW detector can be used to determine the strain of the GW, as follows (Equation 1.12):

$$\frac{\delta L(t)}{L_*} = \frac{1}{2} h_{ij}(t, 0) n^i n^j \quad (1.12)$$

here, L_* is the distance from one test mass, located at the origin, to the second test mass and δL is the small change in length caused by the GW. The second test mass is in the direction of unit vector \vec{n} in the $z = 0$ plane. This describes the set-up of most current GW detectors (Hartle, 2003). In general most ground-based detectors have a lay-out similar to the one in Figure 1.2.

The ground-based detectors are based on Michelson interferometers. GWs that travel parallel to the plane of the detector, result in one of the arms' length being shortened, while the other arms' length gets increased. This change in length of the arms of the detector, leads to the detected light from the laser having a slightly different intensity. The sensitivity of these detectors depends, among other things, greatly on the noise. Examples of the types of noise that affect the sensitivity of these instruments are seismic noise and thermal noise, which is noise due to the masses of the mirrors and their suspension (Pitkin et al., 2011).

LIGO, Virgo and KAGRA (LVK) have a similar frequency range of roughly 10 Hz to 10 kHz (e.g. Martynov et al. (2016), Acernese et al. (2018), Abe et al. (2022)). This

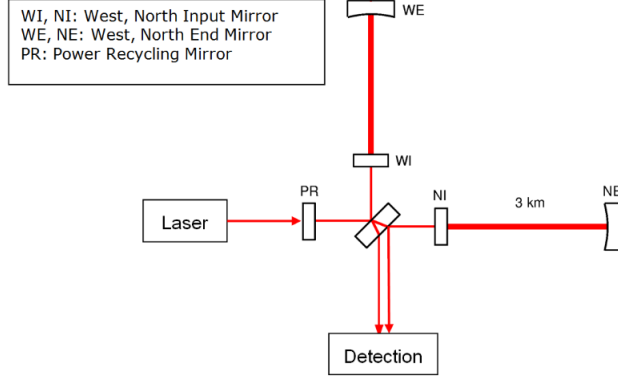


Figure 1.2: Optical Scheme of the Virgo detector (Accadia et al., 2012).

translates to these instruments having the ability to detect signals from the coalescence of compact binaries (consisting of BHs and NSs), general bursts, like supernovae, continuous waves from rotating NSs and the stochastic AGWB (Riles, 2013). Up until now, the ground-based GW detectors have only detected signals coming from the coalescence of compact binaries, e.g. merging binary black holes (BBHs) (see e.g. B. Abbott et al. (2016), merging neutron stars (BNSs) (see e.g. B. Abbott et al. (2017) and merging black holes and neutron stars (BHNSs) (see e.g. R. Abbott et al. (2021a)).

1.3.1 Laser Interferometer Space Antenna (LISA)

The Laser Interferometer Space Antenna (LISA) is a space-based, GW detector that has been officially "adopted" by the European Space Agency (ESA) as of the 25th of January, 2024 (ESA, 2024a). LISA will consist of three identical spacecraft with a length of 2.5 million kilometres between each spacecraft. Each spacecraft will be constituted of two free falling test masses. While not a Michelson interferometer as the above described ground-based detectors, LISA will act in a relatively similar way. The reason why LISA will not exactly act as a Michelson interferometer is because the distance between LISA's arms will change. On the one hand this is because LISA's arms are much larger than the arms of ground-based detectors. On the other hand, LISA will be in space, meaning it is extremely difficult to keep the exact same distance between the arms. Obviously, this is not a problem for ground-based detectors. LISA will be in orbit around the Sun, trailing the Earth at a distance of approximately 50 million kilometre (Amaro-Seoane et al., 2017). This was done for two main reasons, the first being that this distance leads to a stability in the orbit in the long-term. The second reason is that this distance is not too far to negatively impact the requirements for the communication between LISA and Earth (Jennrich, 2009). A schematic of the LISA set-up and its orbit around the Sun can be seen in Figure 1.3

LISA will be operating in the frequency range of 10^{-4} Hz to 10^{-1} Hz (LVK has a frequency range between 10 Hz and 10 kHz). In this undiscovered frequency range, detection of phenomena like merging supermassive black holes (SMBHs), extreme mass-ratio inspirals and mergers of galactic WDs will be possible (Klein et al., 2016; Amaro-Seoane et al., 2017). It is expected that the dominant signal for the LISA detector will come from the merging of millions of BWDs in our galaxy. At low frequencies, these galactic BWDs will be unresolved (i.e. it will be impossible to individually detect these sources). This

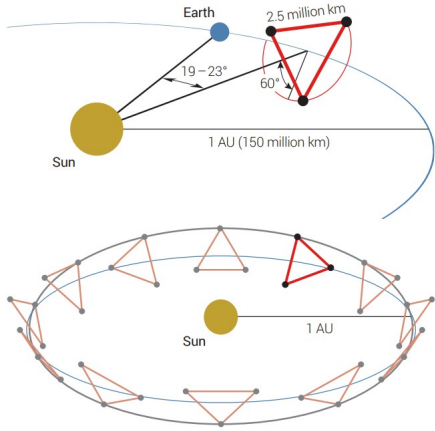


Figure 1.3: The LISA orbit (Amaro-Seoane et al., 2017).

unresolved signal is also known as the galactic foreground. However, some of the signals from BWDs will have a high enough signal to noise ratio, meaning it will be possible to individually detect some of these sources (see e.g. Nelemans et al., 2001; FP03; Korol et al., 2017; Amaro-Seoane et al., 2023). However, as with most detectors, LISA will also be detecting a background signal. It is still unclear what sources will be dominant in this AGWB (see e.g. FP03; SN24 for an AGWB dominated by BWDs and see Lehoucq et al. (2023) for an AGWB dominated by BNSs and BBHs).

1.4 The Astrophysical Gravitational Wave Background (AGWB)

The astrophysical gravitational wave background (AGWB), as the name suggests, is the background signal in GWs that is solely created by astrophysical sources. It is expected to be dominated by the sum of all signals of mergers of compact objects, with other astrophysical sources only playing a small role. These compact object binaries all reside outside our own galaxy. The different types of compact objects (e.g. BWDs, BBHs, BNSs, etc.) that merge each will have a different contribution to the background signal, however it is yet unclear what exact contribution each of the binary types have to the background signal. Moreover, this background signal is expected to be comprised of all in-spiralling binaries summed together, meaning it is impossible to retrieve the signal of one single source (e.g. it will be impossible to filter out the signal provided by a single merging extra-galactic BWD) (see e.g. Schneider et al., 2001; FP03; SN24).

It is important to understand the AGWB that LISA will detect, to be able to properly investigate the signals from single sources (e.g. SMBH mergers). As mentioned in the previous section (Section 1.3.1), it is thus far unclear what this background will precisely consist of. As mentioned before, research has shown that the AGWB will probably consist of extra-galactic mergers of compact binaries. Other (cosmological) possibilities aside from the astrophysical sources, are expected to have a significantly lower magnitude. Much research has been done on what type of compact binary will be the dominant source. Merging extra-galactic BHs and merging extra-galactic NSs, as

well as merging extra-galactic WDs have been pushed forward as promising candidates for the AGWB. Different past works have investigated the contribution of merging BHs and merging NSs (Lehoucq et al., 2023). However, other previous work has found convincing evidence that the background will be dominated by the mergers of extra-galactic WDs (see (FP03; SN24)). This thesis will aim to further confirm this claim, as well as investigate the actual nature of the AGWB signal produced by WDs.

1.5 Research Question, Aims and Motivation

This thesis aims to investigate several different factors that affect the AGWB produced by the merging of extra-galactic WDs. One of the components that will be investigated in particular is the different mass transfer possibilities to form BWDs. Furthermore, the effect of the metallicity of the universe will be investigated as well. This gives rise to the research question for this work: What are the effects of a different choice of mass transfer process and metallicity on the AGWB produced by extra-galactic WDs that will be detected by LISA? This question will be answered by simulating the AGWB for WD populations generated with different possibilities of mass transfer processes at different metallicities.

Considering the fact that the merging of WDs could potentially be the dominant type of mergers in the AGWB, research to this background is interesting and relevant. Understanding the AGWB will make it easier to interpret the GW signals detected by LISA. Moreover, this background signal might be able to give a better explanation about some characteristics and phenomena in our universe, e.g. the metallicity of the universe. However, it might also provide better insight on the formation of BWDs, for example giving hints on which mass transfer process might be the correct process.

The structure of this thesis will be as follows. Chapter 2 will introduce the method on how the AGWB was computed, as well as show the data for the different WD populations. Chapter 3 will introduce the results, while Chapter 4 will interpret them. Lastly, Chapter 5 will summarise the findings of this thesis and have an outlook.

Chapter 2

Methods

This chapter aims to describe the methods used to determine the AGWB produced by extra-galactic WDs. First, the existing framework will be described in detail (see Section 2.1). Following this, some basic parameters are explained which are needed throughout the whole process of determining the AGWB (see Section 2.2). Then, the subject of star formation history will be touched upon as well (see Section 2.1.2). Lastly, an explanation on the population synthesis models used in this thesis is provided as well as an overview of the WD populations used in this work (see Section 2.3).

2.1 Determining the AGWB

This work uses the code made by Seppe Staelens (SN24), with some small alterations to decrease the runtime of the code and to include different star formation histories (SFHs). This code determines the GW signal, Ω , as described below. The theory behind the code is based on Farmer and Phinney's paper (FP03) and on Seppe Staelens' Master Thesis (for the paper based on this thesis, see (SN24)).

2.1.1 Existing Framework

2.1.1.1 Main Contribution to AGWB Signal (Ω)

$\Omega_{gw}(f_r)$ is the GW signal produced by the mergers of BWDs. It can be defined as the energy density of the GW. This energy density of the GW is received in a specific frequency interval around a frequency, f_r . The frequency interval is logarithmic. The energy density is defined as follows:

$$\Omega_{gw}(f_r) = \frac{f_r F_f(f_r)}{\rho_c c^3} \quad (2.1)$$

here, in Equation 2.1, c is the speed of light, ρ_c is the critical mass density of the universe and F_{fr} is the specific flux received in gravitational waves today. The critical mass density can be defined as follows:

$$\rho_c = \frac{3H_0^2}{8\pi G} \quad (2.2)$$

where H_0 is the Hubble parameter and G is the gravitational constant. A definition for the specific flux is given as (Peacock, 1999):

$$F_{f_r} = \frac{L_{f_e}}{4\pi d_L(z)^2} \left(\frac{df_e}{df_r} \right). \quad (2.3)$$

In Equation 2.3, f_e stands for the emitted frequency, the frequency if measured directly when and where the merger was happening. The emitted frequency is expressed as $f_e = (1+z)f_r$, where f_r is the received frequency. The other unknown parameter, $d_L(z)$ is the luminosity distance to redshift z and can be defined as $d_L(z) = (1+z)d_M(z)$. The luminosity distance comes from the relation between bolometric (integrated over all frequencies) flux and bolometric luminosity. In the definition for the luminosity distance, $d_M(z)$ is the proper motion distance. The proper motion distance can be defined as the ratio of an object's velocity perpendicular to the line of sight or direction of motion ($\frac{\text{distance}}{\text{time}}$) to its proper motion , where the proper motion is the observed change of the location of an object in the sky, compared to the Sun ($\frac{\text{radians}}{\text{unit time}}$) (Hogg, 1999).

Assuming there is a large amount of GW sources, that are spread isotropically over the whole sky and range over all redshifts, it can be written that $dL_{f_e}(z) = \ell_{f_e}(z)dV(z)$. ℓ_{f_e} is the comoving specific luminosity density and $dV(z)$ is the comoving volume element defined as $dV(z) = 4\pi d_M^2 d\chi$. Here $d\chi$ is the comoving distance. The term comoving specific luminosity density can be split up to properly explain it. In general it is the energy output for a specific unit of mass (M_\odot , usually) of a group of objects, in this case extra-galactic WDs. This energy density is considered per unit volume, however, the expansion of our universe is taken into account as well (this is also known as the comoving volume element).

Knowing all this, Equation 2.3 can be rewritten:

$$F_{f_r} = \int_{z=0}^{\infty} \frac{\ell_{f_e}(z)}{(1+z)^2} \left(\frac{df_e}{df_r} \right) d\chi(z) . \quad (2.4)$$

To then get the specific flux received in a certain frequency bin, with f_{r1} and f_{r2} as the bounds of the bin, Equation 2.4 should be integrated between these bounds. This gives:

$$\begin{aligned} F_{f_{r1} \rightarrow f_{r2}} &= \int_{z=0}^{\infty} \int_{f_{r1}}^{f_{r2}} \frac{\ell_{f_e}(z)}{(1+z)^2} \left(\frac{df_e}{df_r} \right) d\chi(z) df_r = \\ &\int_{z=0}^{\infty} \int_{f_{r1}(1+z)}^{f_{r2}(1+z)} \frac{\ell_{f_e}(z)}{(1+z)^2} df_e d\chi(z) \end{aligned} \quad (2.5)$$

here, in the second expression (on the right of the second equal sign), the integral over received frequency (f_r) that was present in the first expression (on the left of the second equal sign) was eliminated. Furthermore, to rewrite the equation in terms that can be computed, the specific luminosity density (ℓ_{f_e}) is introduced, which can be defined as:

$$\ell_{f_e} = \sum_k \int_{\nu_0}^{\nu_{\text{merge}}} n_k(\nu, z) L_k(\nu) \delta(f_e - 2\nu) d\nu \quad (2.6)$$

where k indicates each of the WD binary systems and $n_k(\nu, z)$ is the specific number density (the total number of objects) at a redshift, z . Substituting Equation 2.6 into

Equation 2.5, leads to:

$$F_{f_{r1} \rightarrow f_{r2}} = \int_{z=0}^{\infty} \int_{f_{r1}(1+z)}^{f_{r2}(1+z)} \frac{1}{(1+z)^2} \cdot \int_{\nu_0}^{\nu_{merge}} \sum_k n_k(\nu, z) L_k(\nu) \delta(f_e - 2\nu) d\nu df_e d\chi(z). \quad (2.7)$$

The integral over the emitted frequency (f_e) can be removed by using the delta function. This leads to Equation 2.7 being adapted as follows:

$$F_{f_{r1} \rightarrow f_{r2}} = \sum_k \int_{z=0}^{\infty} \frac{d\chi(z)}{(1+z)^2} \int_{\nu_{min}}^{\nu_{max}} n_k(\nu, z) L_k(\nu) d\nu. \quad (2.8)$$

Here, the limits of the integration over orbital frequency (ν) have been changed from ν_0 and ν_{merge} , to $\nu_{min} = \max(\nu_0, \frac{f_{r1}(1+z)}{2})$ and $\nu_{max} = \min(\nu_{merge}, \frac{f_{r2}(1+z)}{2})$. Moreover, it can be reasoned that the specific number density at a certain redshift ($n_k(\nu, z)$) is proportional to $\nu^{-11/3}$ (see FP03). This can then be normalised by setting the following expression as true:

$$n_{\text{bin}} = \int_{\nu_{min}}^{\nu_{max}} A \nu^{-11/3} d\nu. \quad (2.9)$$

Here, n_{bin} is the number density of systems with a frequency between the integration limits stated above, ν_{min} and ν_{max} , and A is the proportionality constant. The number density of systems in this frequency range, can also be defined as:

$$n_{\text{bin}}(z) \approx \frac{\psi(z + z^*)}{3.4 \cdot 10^6 M_{\odot}} \cdot \Delta t(k; \text{bin}). \quad (2.10)$$

Here, in Equation 2.10, ψ is the (cosmic) star formation history (SFH). The exact choice for the SFH is defined and clarified in Section 2.1.2. The factor z^* is an increase in redshift to take into account the star formation rate of the universe at the redshift where the system was born. The factor $3.4 \cdot 10^6 M_{\odot}$ represents the total mass of WD binaries in the population. By equalising Equation 2.9 to Equation 2.10 the proportionality constant A can be found to be equal to:

$$A = \frac{8 \psi(z + z^*(\Delta t))}{3 (3.4 \cdot 10^6 M_{\odot})} \frac{1}{(\nu_{min}^{-8/3} - \nu_{max}^{-8/3})} \cdot \Delta t(k; \text{bin}). \quad (2.11)$$

In general, $\nu_{min} = \frac{f_{r1}(1+z)}{2}$ and $\nu_{max} = \frac{f_{r2}(1+z)}{2}$. Using these two definitions leads to the proportionality constant A to be equal to:

$$A \approx 0.42 \frac{\psi(z + z^*(\Delta t))}{(3.4 \cdot 10^6 M_{\odot})} \frac{(1+z)^{8/3}}{(f_{r1}^{-8/3} - f_{r2}^{-8/3})} \cdot \Delta t(k; \text{bin}). \quad (2.12)$$

Going back to Equation 2.8, the term $n_k(\nu, z)L_k(\nu)$ can be evaluated. First, the gravitational radiation emitted by a binary system coming from the systems orbital energy, L_{circ} is equal to the following:

$$L_{circ} = \frac{32}{5} \frac{G^4}{c^5} \frac{(M_1 M_2)^2 (M_1 + M_2)}{a^5}. \quad (2.13)$$

This binary system has a circular orbit, with masses M_1 and M_2 and the objects have an orbital separation of a (Peters & Mathews, 1963). Using Kepler's third law (Equation 2.33), the definition of the chirp mass (Equation 2.31) and by filling in the constants, G and c , Equation 2.13 can be rewritten as:

$$L = 2.2 \cdot 10^{38} \left(\frac{\mathcal{M}}{M_{\odot}} \right)^{10/3} \left(\frac{\nu}{\text{Hz}} \right)^{10/3} [\text{J s}^{-1}]. \quad (2.14)$$

Knowing that L is proportional to $\nu^{10/3}$ and n_{bin} is proportional to $\nu^{-11/3}$, it is easy to see that the term $n_k(\nu, z)L_k(\nu)$ is proportional to $\nu^{-1/3}$. The integration with respect to ν in Equation 2.8 is now straightforward:

$$\int_{\nu_{\min}}^{\nu_{\max}} n_k(\nu, z)L_k(\nu) d\nu \approx \int_{\nu_{\min}}^{\nu_{\max}} \nu^{-1/3} d\nu = \frac{3}{2}(\nu_{\max}^{2/3} - \nu_{\min}^{2/3}). \quad (2.15)$$

Adding the factors that were left out in the above equation (Equation 2.15), the numerical factor and the chirp mass factor, since these did not depend on the orbital frequency (ν) gives:

$$\begin{aligned} \int_{\nu_{\min}}^{\nu_{\max}} n_k(\nu, z)L_k(\nu) d\nu &= A \cdot (2.2 \cdot 10^{38}) \cdot \left(\frac{\mathcal{M}_k}{M_{\odot}} \right)^{10/3} \cdot \frac{3}{2} \cdot (\nu_{\max}^{2/3} - \nu_{\min}^{2/3}) \\ &= 3.3 \cdot 10^{38} \cdot A \cdot \left(\frac{\mathcal{M}_k}{M_{\odot}} \right)^{10/3} \cdot (\nu_{\max}^{2/3} - \nu_{\min}^{2/3}) [\text{J Hz}^{2/3} \text{s}^{-1}]. \end{aligned} \quad (2.16)$$

This result (Equation 2.16) can be used to get a more detailed version of the specific flux, by plugging it into Equation 2.8. The change in prefactor in the following equation comes from the multiplication of the prefactor of the previous equation (Equation 2.16) and the factor $\frac{8}{3}$ from the definition of A (Equation 2.11). This leads to:

$$\begin{aligned} F_{f_{r1} \rightarrow f_{r2}} &= 8.8 \cdot 10^{38} \sum_k \left(\frac{\mathcal{M}_k}{M_{\odot}} \right)^{10/3} \cdot \\ &\int_{z=0}^{\infty} \frac{d\chi(z)}{(1+z)^2} \frac{(\nu_{\max}^{2/3} - \nu_{\min}^{2/3})}{(\nu_{\min}^{-8/3} - \nu_{\max}^{-8/3})} \frac{\psi(z; k; \text{bin})}{3.4 \cdot 10^6 M_{\odot}} \cdot \Delta t(k; \text{bin}) [\text{J Hz}^{-10/3} \text{s}^{-1}]. \end{aligned} \quad (2.17)$$

As mentioned earlier, in general, the definitions of ν_{\min} and ν_{\max} can be inserted. This means that instead of using Equation 2.11 for the proportionality constant A , Equation 2.12 will be plugged into Equation 2.16. Moreover, by plugging in the definitions of ν_{\min} and ν_{\max} into Equation 2.16, the prefactor also needs to be multiplied by a factor of $\frac{1}{2}(\frac{2}{3})$, coming from the definitions of ν_{\min} and ν_{\max} . This yields the following result:

$$\begin{aligned} F_{f_{r1} \rightarrow f_{r2}} &= 8.7 \cdot 10^{37} \sum_k \left(\frac{\mathcal{M}_k}{M_{\odot}} \right)^{10/3} \cdot \\ &\int_{z=0}^{\infty} (1+z)^{4/3} d\chi(z) \frac{(f_{r2}^{2/3} - f_{r1}^{2/3})}{(f_{r1}^{-8/3} - f_{r2}^{-8/3})} \frac{\psi(k; \text{bin})}{3.4 \cdot 10^6 M_{\odot}} \cdot \Delta t(k; \text{bin}) [\text{J Hz}^{-10/3} \text{s}^{-1}]. \end{aligned} \quad (2.18)$$

If the integral in Equation 2.18 gets discretised and Mpc^2 gets converted to m^2 this Equation becomes:

$$F_{f_{r1} \rightarrow f_{r2}} = 9.17 \cdot 10^{-8} \frac{(f_{r2}^{2/3} - f_{r1}^{2/3})}{(f_{r1}^{-8/3} - f_{r2}^{-8/3})} \sum_{k,i} \left(\frac{\mathcal{M}_k}{\text{M}_\odot} \right)^{10/3} \cdot \frac{\psi(z_i + z_{k,\text{bin}}^*)}{3.4 \cdot 10^6 \text{M}_\odot} \cdot \frac{\Delta t(k; \text{bin}; z_i)}{\text{yr}} (1+z)^{4/3} \frac{\Delta \chi(z_i)}{\text{Mpc}} [\text{kg s}^{-3}]. \quad (2.19)$$

here, the units for some of the parameters ($\Delta t(k; \text{bin}; z_i)$ and $\Delta \chi(z_i)$) were added. To simplify this equation, a definition for $\Delta t(k; \text{bin}; z_i)$ can be found. This can be done by using the following equation:

$$\nu(t)^{-8/3} - \nu_0^{-8/3} = \frac{8K}{3}(t_0 - t). \quad (2.20)$$

This is a formula relating time (t) to orbital frequency (ν), introduced in FP03. The exact description of Equation 2.20 is that it is the evolution of $\nu(t)$, the orbital frequency, for a single source injected at frequency, ν_0 , and time, t_0 . Rearranging Equation 2.20 gives:

$$\Delta t = \frac{3}{8K}(\nu_0^{-8/3} - \nu(t)^{-8/3}). \quad (2.21)$$

where $\Delta t = t - t_0$. Using the definitions for ν_{\min} and ν_{\max} and inserting them into Equation 2.21 gives the needed expression for $\Delta t(k; \text{bin}; z_i)$:

$$\Delta t \approx 2.4 \cdot \frac{1}{K(\mathcal{M})} \cdot (1+z)^{-8/3} \cdot (f_{r1}^{-8/3} - f_{r2}^{-8/3}). \quad (2.22)$$

Using Equation 2.22 and filling it into Equation 2.19 gives the final expression for the specific flux, as seen in the following equation, Equation 2.23. The prefactor was retrieved by first converting seconds to years, and then by multiplying the result by the factor of 2.4 and the numerical value for K from Equation 2.22:

$$F_{f_{r1} \rightarrow f_{r2}} = 1.89 \cdot 10^{-9} (f_{r2}^{2/3} - f_{r1}^{2/3}) \sum_{k,i} \left(\frac{\mathcal{M}_k}{\text{M}_\odot} \right)^{5/3} \cdot \frac{\psi(k; \text{bin}; z_i)}{3.4 \cdot 10^6 \text{M}_\odot} \cdot (1+z_i)^{-4/3} \cdot \frac{\Delta \chi(z_i)}{\text{Mpc}} [\text{kg s}^{-3}]. \quad (2.23)$$

One of the last needed equations is an equation that describes the time a binary system takes to go from its birth frequency (ν_0) to the lower end of the frequency bin that has been redshifted. This equation can be defined as follows:

$$\tau_k = \frac{3}{8K(\mathcal{M}_k)} (\nu_0^{-8/3} - (f_{r1}(1+z)/2)^{-8/3}). \quad (2.24)$$

The above equation, Equation 2.24, comes from Equation 2.20.

For each binary system, a time ($t_{0,k}$) is known, which gives the time between the formation of the stars in the system and the formation of the binary. The parameter z^* , as defined above as the increase in redshift to take into account the star formation rate

of the universe at the redshift where the system was born, is then determined in the following way. z^* is defined so that the factor $z + z^*$ correlates to a time $\tau_k + t_{0,k}$. This time comes before the time that corresponds to a redshift, z . In this thesis the redshift region of interest ranges from $z = 0$, to $z = 8$. This means only binary systems where $\tau_k + t_{0,k} \leq \tau(z) - \tau(z = 8)$ are taken into account. $\tau(z)$ corresponds to the age of the universe at a specific redshift, z . The above also means that the definition of star formation rate is slightly altered, namely to $\psi(z + z^*)$.

Combining Equation 2.23, Equation 2.24 and Equation 2.1, as well as filling in the numerical values for the speed of light, c , and the critical mass density of the universe, $\rho_c \approx 8.5988 \cdot 10^{-27}$ (see Equation 2.2), where a Hubble parameter of $67.66 \frac{\text{km}}{\text{s} \cdot \text{Mpc}}$ was used, gives the following formula for Ω :

$$\Omega \approx 4.3 \cdot \frac{f_r F_{f_{r1} \rightarrow f_{r2}}}{f_{r2} - f_{r1}} = \\ 8.10 \cdot 10^{-9} \cdot f_r \frac{(f_{r2}^{2/3} - f_{r1}^{2/3})}{(f_{r2} - f_{r1})} \sum_{k,i} \left(\frac{\mathcal{M}_k}{\text{M}_\odot} \right)^{5/3} \cdot \frac{\psi(z_i + z_{k,\text{bin}}^*)}{3.4 \cdot 10^6 \text{M}_\odot} \cdot (1 + z_i)^{-4/3} \cdot \frac{\Delta\chi(z_i)}{\text{Mpc}}. \quad (2.25)$$

Finally, by getting rid of the normalisation factor of $3.4 \cdot 10^6 \text{ M}_\odot^1$ in Equation 2.25 and adding the units for the SFH, the final expression is retrieved:

$$\Omega = 2.4 \cdot 10^{-15} \cdot f_r \frac{(f_{r2}^{2/3} - f_{r1}^{2/3})}{(f_{r2} - f_{r1})} \sum_{k,i} \left(\frac{\mathcal{M}_k}{\text{M}_\odot} \right)^{5/3} \cdot \frac{\psi(z_i + z_{k,\text{bin}}^*)}{\text{M}_\odot \text{Mpc}^{-3} \text{yr}^{-1}} \cdot (1 + z_i)^{-4/3} \cdot \frac{\Delta\chi(z_i)}{\text{Mpc}}. \quad (2.26)$$

Equation 2.26 is used to determine the AGWB signal of merging BWDs per frequency bin.

2.1.1.2 Contributions of the Birth and the Merger to AGWB Signal (Ω)

The BWD systems each go through multiple frequency bins during their lifetime (from birth to merger). Most of the bins they traverse, the systems will traverse completely. However, for all systems, there are two bins that are not fully traversed. These two bins are the so-called birth bin (the frequency bin in which the system is "born") and the merger bin (the frequency bin in which the system merges). An important thing to note is that the birth and the merger bin have a slightly different contribution to the final signal that will be detected, since the systems do not traverse these frequency bins completely. To ensure that these contributions are taken into account correctly, some of the above described equations in the previous section (Section 2.1.1.1) need to be slightly

¹This normalisation factor is the total mass of all WD binaries in the population. In this thesis stars between a mass of 0.8M_\odot and 11M_\odot were selected, since these masses are expected to produce WDs. The previous work by SN24 uses stars with masses between 0.9M_\odot and 11M_\odot , meaning the normalisation factor in that work is $4 \cdot 10^6 \text{ M}_\odot$.

altered.

To include the contributions described above, Equation 2.17 will be the starting point. However, instead of inserting the definitions for ν_0 and $\nu(t)$ (or ν_{min} and ν_{max}), these variables are kept in the formula. This means that for the proportionality constant A , Equation 2.11 is used (as in Equation 2.17). Furthermore, instead of Equation 2.22, Equation 2.21 is used, as the Δt factor. Again, discretizing the integral and going from Mpc^2 to m^2 , as well as going from seconds to years leads to a specific flux of:

$$F_{f_{r1} \rightarrow f_{r2}} = 2.97 \cdot 10^{-9} \sum_{k,i} (\nu_{max}^{2/3} - \nu_{min}^{2/3}) \left(\frac{\mathcal{M}_k}{\text{M}_\odot} \right)^{5/3} \cdot \frac{\psi(k; bin; z_i)}{3.4 \cdot 10^6 \text{M}_\odot} \cdot (1 + z_i)^{-2} \cdot \frac{\Delta\chi(z_i)}{\text{Mpc}} [\text{kg s}^{-3}]. \quad (2.27)$$

Now, knowing the specific flux for the contribution of the birth and the merger, Ω can be found in a similar way as described in the previous section, above Equation 2.26:

$$\Omega \approx 4.3 \cdot \frac{f_r F_{f_{r1} \rightarrow f_{r2}}}{f_{r2} - f_{r1}} = 1.28 \cdot 10^{-8} \cdot f_r \sum_{k,i} \frac{(\nu_{max}^{2/3} - \nu_{min}^{2/3})}{f_{r2} - f_{r1}} \left(\frac{\mathcal{M}_k}{\text{M}_\odot} \right)^{5/3} \frac{\psi(k; bin; z_i)}{3.4 \cdot 10^6 \text{M}_\odot} (1 + z_i)^{-2} \cdot \frac{\Delta\chi(z_i)}{\text{Mpc}}. \quad (2.28)$$

Furthermore, if the normalisation factor $3.4 \cdot 10^6 \text{ M}_\odot^2$ is eliminated from Equation 2.28 and the units for the SFH are added, the final result for Ω for the birth and merger contributions becomes:

$$\Omega = 3.77 \cdot 10^{-15} \cdot f_r \sum_{k,i} \frac{(\nu_{max}^{2/3} - \nu_{min}^{2/3})}{f_{r2} - f_{r1}} \left(\frac{\mathcal{M}_k}{\text{M}_\odot} \right)^{5/3} \frac{\psi(k; bin; z_i)}{\text{M}_\odot \text{Mpc}^{-3} \text{yr}^{-1}} (1 + z_i)^{-2} \cdot \frac{\Delta\chi(z_i)}{\text{Mpc}}. \quad (2.29)$$

Knowing the expressions for Ω for all contributions, Equation 2.26, for the main contributions, and Equation 2.29, for the birth and merger contributions, the AGWB signal produced by extra-galactic BWDs can be determined.

2.1.2 Star Formation Rate

The star formation rate (SFR), as the name suggests is an expression that gives the rate of star formation in our universe. This is an extremely important factor in the study of our universe. A lot is still unclear regarding the cosmic SFR, however, it is thought that the SFR has changed over time. This gives rise to another important concept, namely the star formation history (SFH). This is the SFR for different points in time (or in the case of this thesis, for different redshifts) (Carroll & Ostlie, 2014). Another term

²Again, SN24 uses a normalisation factor of $4 \cdot 10^6 \text{ M}_\odot$.

describing the same concept is the star formation rate density (SFRD). This is the same as the SFH, where it describes the SFR for different redshift, except the SFRD also takes into account different metallicities (see e.g. Chruścińska & Nelemans (2019)). Again, the nature of the cosmic SFH (or SFRD) is still ambiguous. Previous work (SN24) investigating the AGWB looked at a constant SFH, meaning an SFR that only depends on redshift. This is why this work will also take a constant SFH into account, which will be further explained in Section 2.1.2.1. However, it is known that the SFRD (a SFR dependent on both redshift and metallicity) is most likely the correct way to describe the universe, which is why the SFRD is also investigated in this thesis. Moreover, since this work aims to investigate the effect of metallicity on the AGWB, looking at a metallicity dependent SFRD is of great importance. This will be explained in more detail in Section 2.1.2.2.

2.1.2.1 Metallicity Independent SFR

In the case of a constant metallicity, e.g. there is one specific metallicity that is true for the whole universe, the SFH described by Madau & Dickinson (2014) will be used:

$$\psi(z) = 0.015 \frac{(1+z)^{2.7}}{1 + ((1+z)/2.9)^{5.6}}. \quad (2.30)$$

As seen in Equation 2.30, this relation only depends on the redshift, z . This relation was determined with the help of several galaxy surveys, which were used to determine the SFH directly. The main thing done to retrieve this expression is to couple the equations of chemical evolution to the spectroscopic and photo-metric characteristics of the universe (Madau & Dickinson, 2014).

2.1.2.2 Metallicity Dependent SFR

Besides the constant SFR (only dependent on redshift), a SFR that depends on both redshift and metallicity will be investigated. This was done by using data made publicly available by Chruścińska & Nelemans (2019); Chruścińska et al. (2021). These papers use the observed properties of galaxies as well as the uncertainties in these galaxies at different redshifts. This is then used to construct several different models for the SFRD. These models give the stellar mass density per metallicity per redshift. The metallicity ranges between 0.13 and 0.000005, while the redshift ranges between 0 and 10. Since the extremely high redshifts are not of interest for this work, only redshifts between 0 and 8 were used. The redshift was binned on a logarithmic scale with smaller bins at lower redshifts and larger bins at higher redshifts. For this thesis, the data was binned in metallicity and the six bins are shown in Table 2.1. For each of the metallicity bins, an input file of the population synthesis is chosen. This input file has a metallicity somewhere in the bin. One limiting factor on the location of the metallicity of the input file in the metallicity bin was the SEBA code, which could only run with a metallicity up to 0.03, which is significantly lower than the largest metallicity provided with the data.

The data produced by Chruścińska & Nelemans (2019); Chruścińska et al. (2021) uses a variety of different assumptions on different important components of the SFRD. The

Table 2.1: The metallicity bins used to bin the data by Chrušlińska & Nelemans (2019); Chrušlińska et al. (2021) and the corresponding metallicity of the used population synthesis models.

Metallicity Bins	Population Synthesis Metallicity
$Z \geq 0.03$	$Z = 0.03$
$0.015 \leq Z < 0.03$	$Z = 0.02 = Z_{\odot}$
$0.008 \leq Z < 0.015$	$Z = 0.01$
$0.003 \leq Z < 0.008$	$Z = 0.005$
$0.0005 \leq Z < 0.003$	$Z = 0.001$
$Z < 0.0005$	$Z = 0.0001$

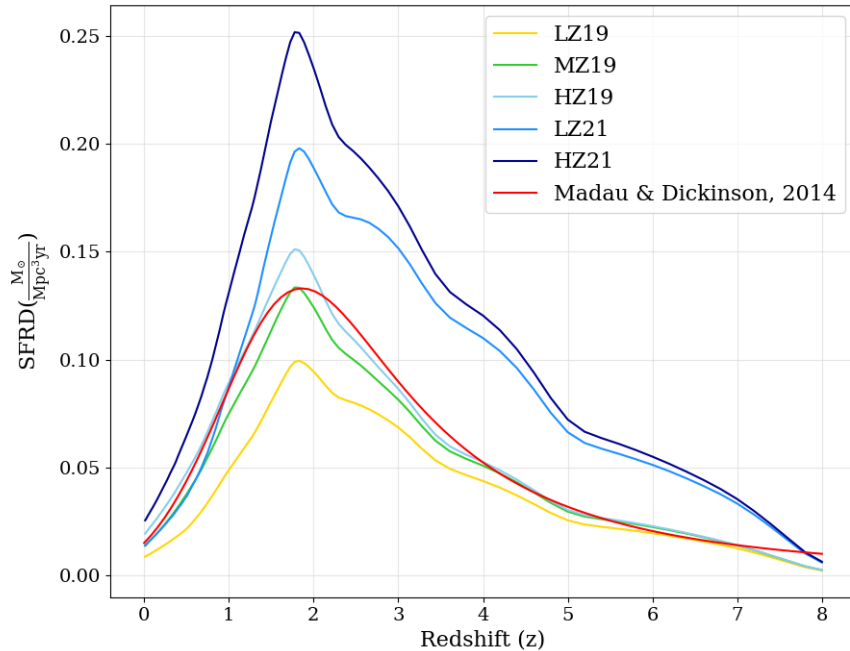


Figure 2.1: Total star formation rate density (SFRD) in $M_{\odot} \text{Mpc}^{-3} \text{yr}^{-1}$ vs redshift for the six different SFHs/SFRDs. The red line represents the SFH by Madau & Dickinson (2014). The green line represents the MZ19 model. The light blue and yellow line represent the HZ19 and LZ19 model, respectively. The sky blue and the dark blue line represent the HZ21 and LZ21 model, where starburst galaxies were included (see Section 2.1.2.2 or Chrušlińska et al. (2021)).

AGWB was reconstructed for five different types of models introduced in the two papers. The five different models, along with the SFH by Madau & Dickinson (2014), can be seen in Figure 2.1. The first model is the so-called moderate metallicity model from the 2019 paper (Chruścińska & Nelemans, 2019) (from here on out called MZ19). From this same paper, a high metallicity extreme model (HZ19) and a low metallicity extreme model (LZ19) were used. The high metallicity extreme, as the name suggests, has more mass formed at a higher metallicity. Similarly, the low metallicity extreme has more mass formed at the lower metallicities. The moderate metallicity model, lies somewhere in between the two. The two other models were introduced in the 2021 paper (Chruścińska et al., 2021). The models in this second paper were, again, the so-called high metallicity extreme (HZ21) and low metallicity extreme (LZ21) models. This paper did not provide a model similar to the moderate metallicity model from the 2019 paper. Once more, these names correspond to the metallicities at which these models generate the most mass. The difference between the models from the two papers comes mainly from the inclusion of starburst galaxies in the 2021 paper, which significantly increases the total SFRD (Chruścińska et al., 2021). A detailed description on the way these five models were constructed (i.e. what parameters were used to create them) can be found in the following works, Chruścińska & Nelemans (2019) and Chruścińska et al. (2021)³.

Figure 2.1 shows the total SFRD per redshift, z . All five metallicity dependent models, as well as the SFH by Madau & Dickinson (2014), show a peak of their respective SFRD (or SFH in the case of Madau & Dickinson (2014)) at a redshift of about 1.8. The MZ19 model peaks at roughly the same SFRD as the relation by Madau & Dickinson (2014). The HZ19 and LZ19 models, lie higher and lower than the MZ19 model, respectively. Due to the inclusion of starburst galaxies in the models from 2021, HZ21 and the LZ21 models both lie significantly higher than the models from 2019.

The SFRD per metallicity bin, again see Table 2.1 for the exact bins, is shown in Figure 2.2 to Figure 2.4. Figure 2.2 shows the total SFRD per metallicity bin per redshift (z) for the MZ19 model. The three bins with the highest amount of SFRD in them, are those with a metallicity ranging approximately between 0.02 and 0.005. Both the highest and the lowest metallicity bins contribute less to the total SFRD. Moreover, the three aforementioned metallicities peak around a redshift of 1.8 (where the total SFRD of the models also peaked, see Figure 2.1). The two lowest metallicities (0.001 and 0.0001) peak at a slightly higher redshift of $z = 3$. The highest metallicity ($Z = 0.03$) seems to peak at 1.8, however, the peak is broader than the three metallicities that also peak there.

Figure 2.3 shows the total SFRD per metallicity bin for the LZ21 model. While the name suggests that most SFRD should be in the lower metallicity bins, evidently, this is not the case. The highest amounts of SFRD can be found in the bins surrounding the following metallicities: $Z = 0.005$, $Z = 0.01$ and $Z = 0.001$. Interestingly, the dark yellow line, corresponding to a metallicity of 0.001 seems to have two peaks. The line relating to the lowest metallicity ($Z = 0.0001$) seems to be significantly higher compared

³The three models that were used from the 2019 data are named as follows: LZ19 = low-Z_extreme_FOH_z_dM, MZ19 = moderate_FOH_z_dM and HZ19 = high-Z_extreme_FOH_z_dM (Chruścińska & Nelemans, 2019). The data files used from the 2021 paper are called 204f14SBBiC_FMR270_FOH_z_dM for the LZ21 model and 302f14SBBiC_FMR270_FOH_z_dM for the HZ21 model, respectively (Chruścińska et al., 2021).

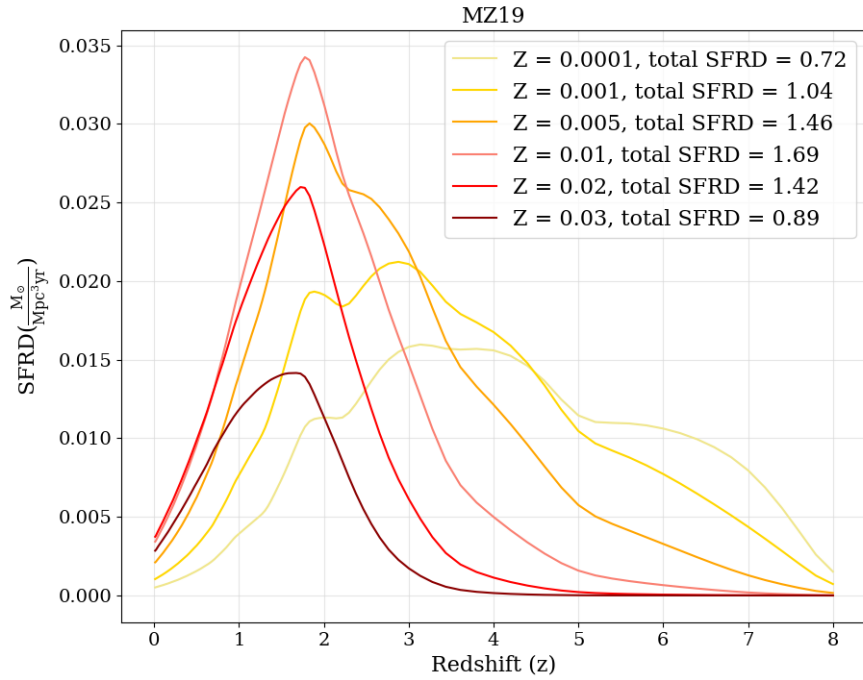


Figure 2.2: Total SFRD in $M_{\odot} \text{Mpc}^{-3} \text{yr}^{-1}$ vs redshift for the six metallicity bins. The model represented here is the MZ19 model.

to where it lies for the other models, MZ19 and HZ21, respectively. This is expected, since most of the SFRD is expected to be in the lower metallicity bins in the case of the LZ21 model. The two highest metallicity bins encompass the lowest amounts of the SFRD.

Figure 2.4 shows the SFRD distributed among the six metallicities bins for the HZ21 model. As the name suggests, the higher metallicities (the more red-ish colours) have a higher peak in SFRD than the lower metallicities. These lower metallicities do not have just a single peak at a redshift of 1.8 like the higher metallicities. Instead, these metallicities have two peaks, one at a redshift of 1.8 and one at a redshift of approximately 2.8.

Figures 2.3 and 2.4 only show the models with the inclusion of starburst galaxies (the models from the 2021 paper). The corresponding models from the 2019 paper, look very similar to the ones shown in Figures 2.3 and 2.4, with the only difference being the fact that the SFRD values are lower for the models from the 2019 paper.

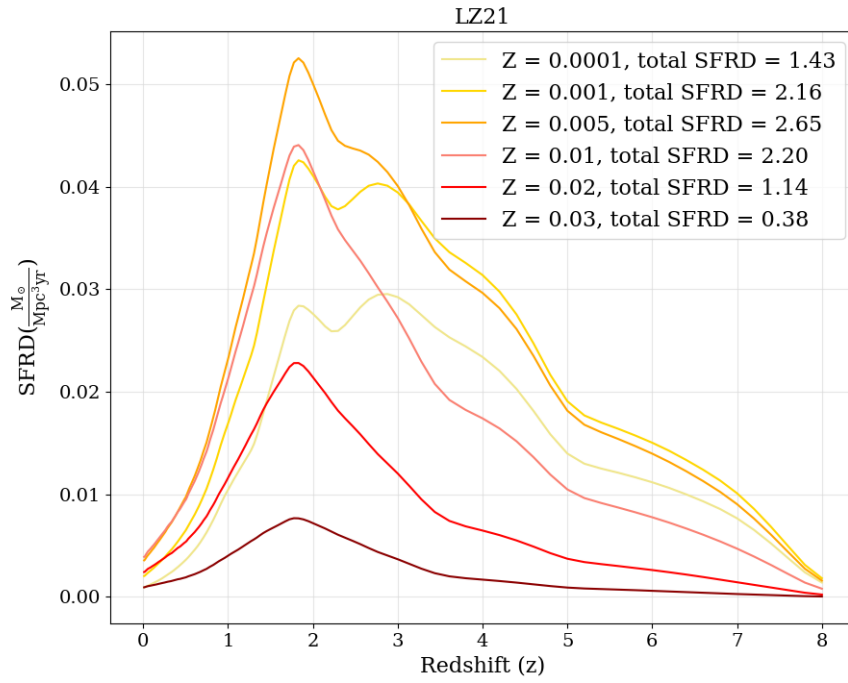


Figure 2.3: Total SFRD in $M_{\odot} \text{Mpc}^{-3} \text{yr}^{-1}$ vs redshift for the six metallicity bins. The model represented here is the LZ21 model.

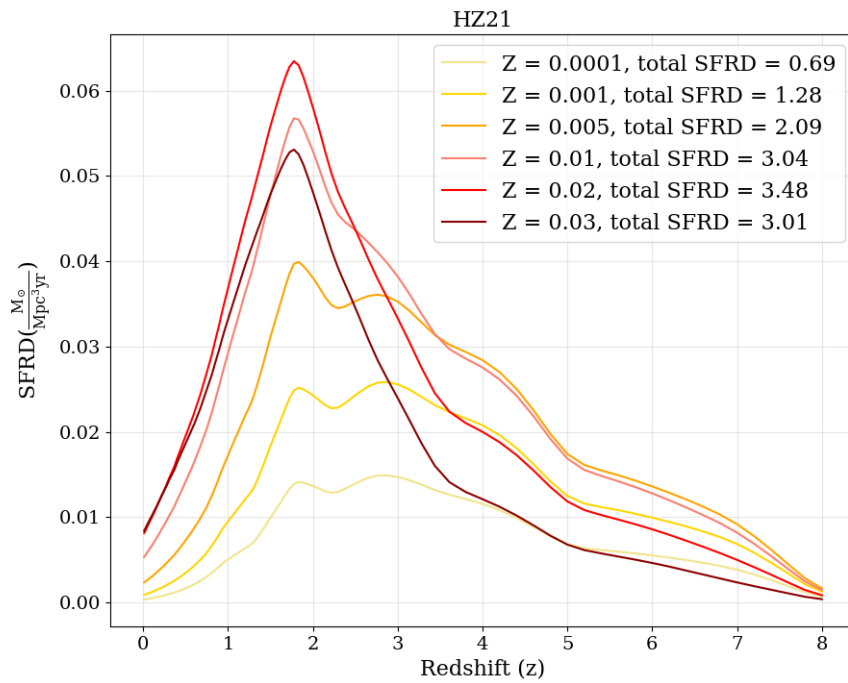


Figure 2.4: Total SFRD in $M_{\odot} \text{Mpc}^{-3} \text{yr}^{-1}$ vs redshift for the six metallicity bins. The model represented here is the HZ21 model.

2.2 Preparations for Input Data

Some essential parameters of the BWDs have to be computed, which are used in the determination of the AGWB. The first one of these parameters is the chirp mass (\mathcal{M}), which can be defined as follows:

$$\mathcal{M} = \frac{M_1^{3/5} M_2^{3/5}}{(M_1 + M_2)^{1/5}}. \quad (2.31)$$

In Equation 2.31, M_1 and M_2 are the masses (in M_{\odot} , of stars 1 and 2, respectively. Besides the chirp mass, K , a constant dependent on the chirp mass is needed as well:

$$K = \frac{96}{5} (2\pi)^{8/3} \left(\frac{G\mathcal{M}}{c^3} \right)^{5/3} \approx (3.7 \cdot 10^{-6}) \left(\frac{\mathcal{M}}{M_{\odot}} \right)^{5/3} [\text{s}^{5/3}]. \quad (2.32)$$

Kepler's third law, defined in Equation 2.33 is an important equation, since it can be used to determine both the initial orbital frequency (ν_0) and the maximum orbital frequency (ν_{max}) of the binary system:

$$a^3 \nu^2 = \frac{G(M_1 + M_2)}{4\pi^2}. \quad (2.33)$$

The initial orbital frequency (ν_0) can be determined by plugging in the two masses of the stars and the initial orbital separation (a_i), into Equation 2.33. As the name of the parameter suggests, this gives the orbital separation of the system at the time of its birth. Finding the maximum orbital frequency (ν_{max}) requires more calculation. First, the radii of both WDs in the binary system are determined. If the mass of the WD is larger than or equal to the Chandrasekhar limit ($M_{ch} = 1.44M_{\odot}$), the radius of the WD is set to a predetermined value of $0.001R_{\odot}$. However, if the WD has a mass lower than the Chandrasekhar limit, the following formula on the mass-radius relation in close binaries can be used to determine the radius of the WD (Verbunt & Rappaport, 1988):

$$\frac{R}{R_{\odot}} = 0.0114 \left[\left(\frac{M}{M_{ch}} \right)^{-2/3} - \left(\frac{M}{M_{ch}} \right)^{2/3} \right]^{1/2} \times \left[1 + 3.5 \left(\frac{M}{M_p} \right)^{-2/3} + \left(\frac{M}{M_p} \right)^{-1} \right]^{-2/3}. \quad (2.34)$$

Here, in Equation 2.34, M_p is a constant with a value of $0.00057M_{\odot}$ and M_{ch} is the aforementioned Chandrasekhar limit, which has a value of $1.44M_{\odot}$. If both radii of both WDs have been calculated, the minimum orbital separation (a_{min}) can be determined. This is the orbital separation at the time of the merger, since the orbit of the binary shrinks during the period of time between the birth of the binary and the merger, as it loses orbital energy in the form of GWs during this so-called inspiral. Moreover, the minimum orbital separation corresponds to the maximum orbital frequency. The formula for the minimum orbital separation if the primary star in the binary system fills its Roche lobe, is as follows (Eggleton, 1983):

$$\frac{a_{p,min}}{R_{\odot}} = R_1 \cdot \frac{0.6q^{-2/3} + \ln(1 + q^{-1/3})}{0.49q^{-2/3}}. \quad (2.35)$$

Similarly, if the secondary star is the star filling its Roche lobe, the following equation can be used:

$$\frac{a_{s,min}}{R_{\odot}} = R_2 \cdot \frac{0.6q^{2/3} + \ln(1 + q^{1/3})}{0.49q^{2/3}}. \quad (2.36)$$

In both Equations 2.35 and 2.36, q is the mass ratio, defined as $q = \frac{M_2}{M_1}$. The minimum orbital separation (a_{min}) of the binary system is then easily determined by finding the largest value between the results of Equations 2.35 and 2.36. With the minimum orbital separation defined, it is trivial to see how to determine the maximum orbital frequency (ν_{max}). This can be done in a very similar way as to how the initial orbital frequency (ν_0) was defined, namely by simply plugging in the minimum orbital separation into Kepler's third law, Equation 2.33. This gives the penultimate parameter that is needed.

To get the last initial parameter, Equation 2.21 is used. Using the definition for the orbital frequency ($\nu = f/2$), leads to this equation becoming:

$$\tau = \frac{2.381 \cdot (f_0^{-8/3} - f_1^{-8/3})}{K} [\text{Myr}]. \quad (2.37)$$

In Equation 2.37, τ is the time it takes for a binary to evolve from frequency f_0 to f_1 , where the binary is characterised by constant K (see Equation 2.32). This gives all the essential parameters based on the population of the WD binaries, needed for the determination of the AGWB.

2.3 Population Synthesis

The above introduced equations require some parameters that are specific to the BWD systems, like both masses of the WDs (M_1, M_2) and the orbital separation of the system at the time of birth (a_i). The BWDs and their corresponding parameters were simulated using the SEBA code (Portegies Zwart & Verbunt, 1996; Nelemans et al., 2001; Toonen et al., 2012). It is a code that simulates both stellar and binary evolution, starting from stars at the zero-age main-sequence (ZAMS) stage, the moment a star stars fusing hydrogen, thus getting on the main sequence, up until and including the remnant phases of the stars. Different metallicities can be chosen as input, as well as choices to include processes like mass loss through stellar winds, supernovae and interactions occurring in binary systems. As mentioned in Chapter 1 (Section 1.1.1), in this thesis, two possibilities to form BWDs are considered. These possibilities can be translated into population synthesis models. To investigate the effect of different population synthesis models, four different population synthesis models were created, two of which had two α mass transfer phases, while the other two first went through a γ mass transfer phase and afterwards went through an α mass transfer phase. For both cases, a numerical value of α of 1 or 4 was used. γ was set to a value of 1.75⁴. So, four different population synthesis models were run. For each of these four population synthesis models α , six metallicities were chosen and run, leading to a total of 24 datasets. The six metallicities are shown in the second column of Table 2.1. The output of these 24 datasets contained four different initial parameters. The time of birth of the system (t_0), the masses of both the primary and the secondary star in the binary system (M_1 and M_2 , respectively) and the initial orbital separation (a_i).

⁴In Section 1.1.1, the range for γ is defined as being between ~ 1.4 and ~ 1.7 . 1.75 obviously does not fall in this range, however, this value was chosen since the original range did not take into account stellar winds, while a value of 1.75 does take this into account (Nelemans et al., 2000).

The different input values for the mass transfer processes as well as the metallicities lead to some differences for the characteristics of the population of BWDs. To get a visualisation of this, all models were plotted in density plots, as seen in Figures 2.5 and 2.6. The black dashed line in this plot indicates the border at which the orbital frequency (ν_0) changes with less (or more) than 10 percent. Systems on the left of the black dashed line have a change of less than 10 percent during 13.7 Gyr (the age of the universe, or the Hubble time), while systems on the right of the black dashed line can have an increase in orbital frequency of more than 10 percent during the Hubble time. The black line was determined with the use of Equation 2.20. Since LISA's operational frequency range is only between 10^{-4} to 10^{-1} Hz and systems to the left of the black dashed line barely move along the x-axis during their lifetime, it can be said that the part of the population that is most relevant, is the population in this frequency range (between 10^{-4} to 10^{-1} Hz).

The two plots in Figure 2.5 show roughly the same shape. For the higher metallicities ($Z = 0.01, 0.02, 0.03$) the chirp masses are closer to 1 for $\alpha = 1$, compared to $\alpha = 4$. Furthermore, for the same metallicities, for $\alpha = 1$, there is a more prominent second subset of the population at a frequency of roughly 10^{-6} Hz, which does not exist for $\alpha = 4$. However, as mentioned before, it should be noted that this part of the population will be less relevant for this study, since it lays outside LISA's frequency range and will not be able to move towards this range in the Hubble time. For $\alpha = 4$, the main part of the population resides at about 10^{-4} Hz.

Looking at both plots in Figure 2.6 and first comparing these with both plots in 2.5, it is evident that the choice of input parameters for the population synthesis has a significant effect on the population of BWDs. The shape of the density plots in Figure 2.6 are distinctly different compared to the density plots in Figure 2.5. Again, it seems that the difference in populations between the two different values of α can be most clearly seen at higher metallicities ($Z = 0.01, 0.02, 0.03$). For a numerical value of α of 4, the population of BWDs seem to have a wider range in frequency compared to a numerical value of α of 4.

Table 2.2 shows the average chirp masses for each of the six metallicities for each of the population synthesis models. It is clear to see that the average chirp masses are highest for the lowest metallicities ($Z = 0.0001$ and $Z = 0.001$), which can also be seen in the figures. The other metallicities only have extremely small differences, both when comparing metallicities as well as when comparing population synthesis models.

One thing that should be noticed, however, is that this table only represents the average value for the chirp masses. When looking at the figures (Figure 2.5 and Figure 2.6) it is clear that the full distribution of the chirp masses does change a lot when looking both at different metallicities for each of the population synthesis models, as well as when looking at one metallicity and comparing it to the other three population synthesis models.

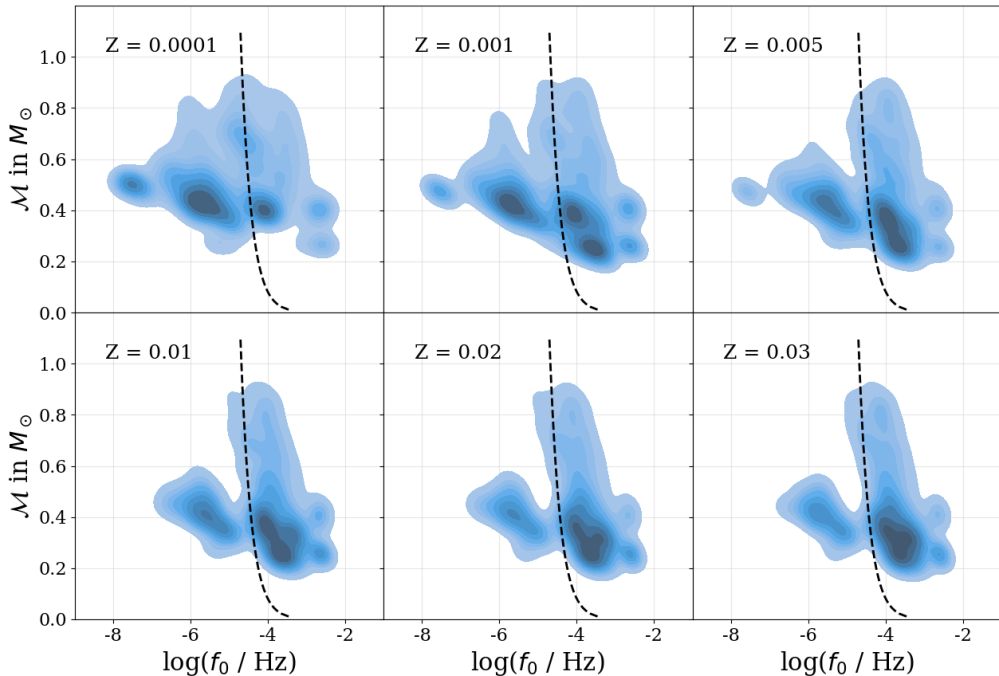
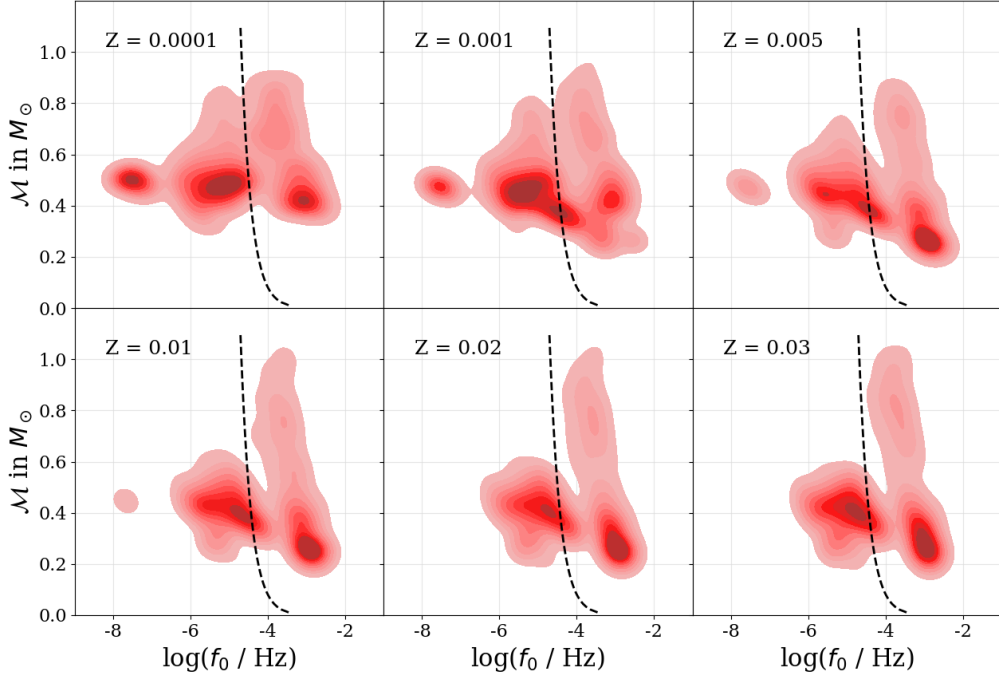


Figure 2.5: Density plot of chirp mass (\mathcal{M}) in M_\odot vs frequency ($\log(f_0/\text{Hz})$) for the models with two α mass transfer phases. Here the upper plots (red) represent α with a numerical value of 1, whereas the lower plots (blue) represent α with a numerical value of 4. The black dashed line in each of the plots represents the point where the frequencies of the BWD systems do not evolve more than 10 percent of their initial frequency in the Hubble time (13.7 Gyr).

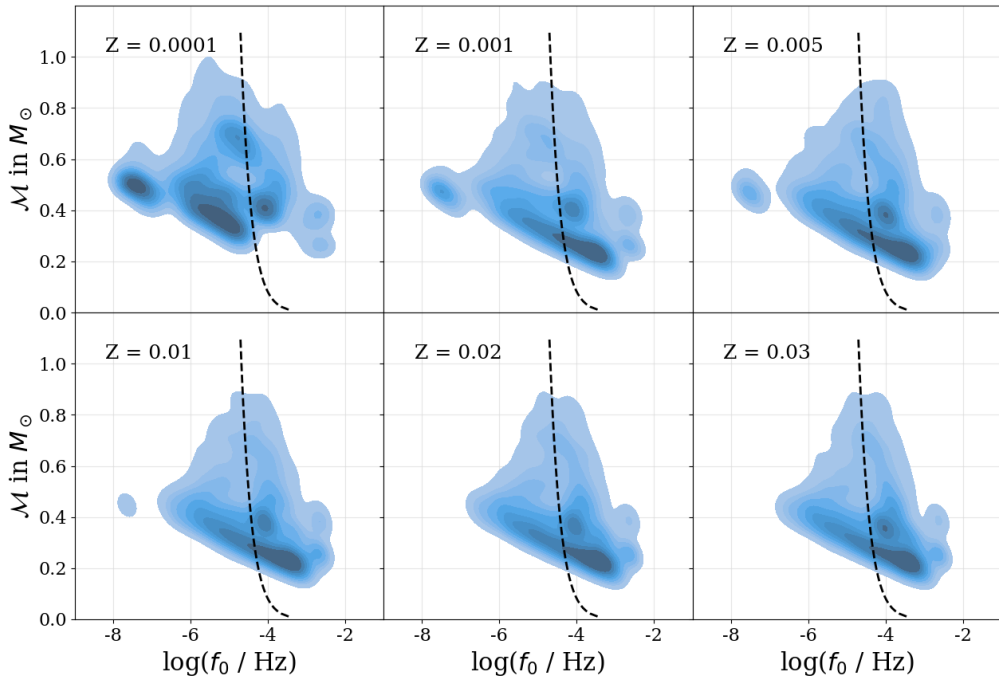
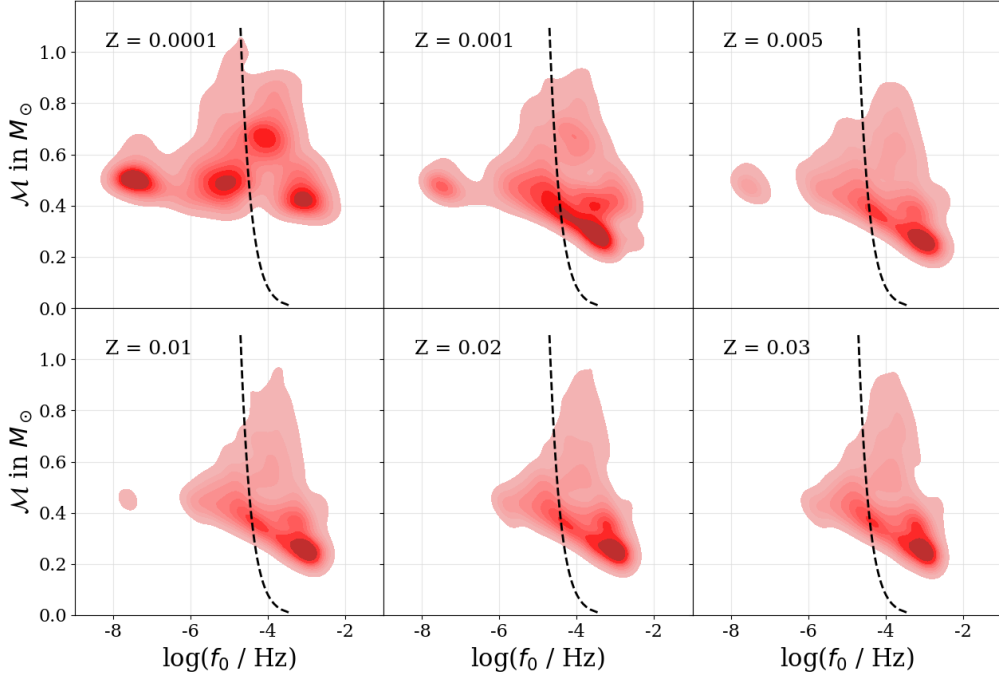


Figure 2.6: Density plot of chirp mass (\mathcal{M}) in M_\odot vs frequency ($\log(f_0/\text{Hz})$) for the models with one γ and one α mass transfer phase. Here the upper plots represent α with a numerical value of 1, whereas the lower plots represent α with a numerical value of 4. The black dashed line in each of the plots represents the point where the frequencies of the BWD systems do not evolve more than 10 percent of their initial frequency in the Hubble time (13.7 Gyr).

Table 2.2: The average chirp masses retrieved from the SEBA code for each of the metallicities for each of the population synthesis models. All values are in units of solar mass (M_{\odot}).

Z	$\alpha\alpha, \alpha = 1$	$\alpha\alpha, \alpha = 4$	$\gamma\alpha, \alpha = 1$	$\gamma\alpha, \alpha = 4$
0.0001	0.54	0.51	0.56	0.51
0.001	0.48	0.45	0.47	0.43
0.005	0.44	0.44	0.43	0.43
0.01	0.43	0.43	0.42	0.41
0.02	0.42	0.42	0.41	0.40
0.03	0.43	0.42	0.41	0.40

Chapter 3

Results

This chapter shows the results of this thesis. First a comparison is made to the previous work by SN24. After this section, the specific results of this work are shown. These results include the effects of different population synthesis models and different metallicities. Furthermore, the results demonstrate the effect of a metallicity dependent SFRD. This is shown by looking at one metallicity dependent SFRD model in detail, as well as looking at the sums of five different metallicity dependent SFRD models. Moreover, a connection between the total SFRD models and the corresponding AGWB signals is investigated. Lastly, an approximation of the uncertainties of the AGWB signal is shown. These uncertainties are produced using the results of this work.

3.1 AGWB Comparison with Previous Work

To ensure that the results for the AGWB in the upcoming sections are valid, first, one of the results of this work was compared with the previous work on which this thesis is based (SN24). The results in the work by SN24 are obtained by using a population synthesis model with two alpha mass transfer phases ($\alpha\alpha$) with a numerical value of α of 4. Moreover, the data used had a solar metallicity ($Z = Z_\odot = 0.02$).

Figure 3.1 shows the comparison between the previous work and this work. In this figure, the two straight lines, blue and green, respectively, represent the binary neutron star (BNS) and binary black hole (BBH) signal detected by the LVK detectors. The shaded areas around the blue and green line represent their corresponding errors. Their exact numerical values for the BNS and BBH AGWB signal are as follows (R. Abbott et al., 2021b):

$$\Omega_{\text{BNS}}(25\text{Hz}) = 2.0^{+3.2}_{-1.4} \times 10^{-10}$$

$$\Omega_{\text{BBH}}(25\text{Hz}) = 4.7^{+1.6}_{-1.4} \times 10^{-10}$$

The black dashed line represents the upper limits of the LVK collaboration, which are defined as (R. Abbott et al., 2021b):

$$\Omega_{\text{GW}}(f) \leq 3.4 \times 10^{-9}$$

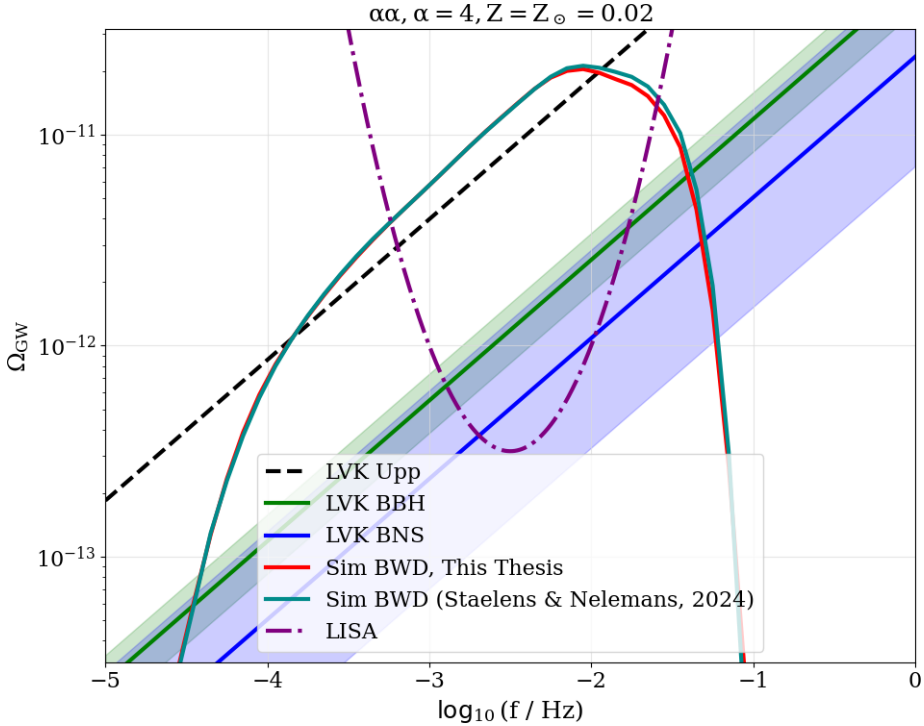


Figure 3.1: The AGWB (Ω) as a function of frequency (f) in Hz on a logarithmic scale. The black dashed line represents the upper limits by the LVK collaboration. The green and blue line represent the BBH and BNS signal, both with an error margin, respectively (R. Abbott et al., 2021b). The purple line represents an approximation to LISA’s range in which GW signals will be detected. The teal line is the AGWB signal from SN24. The red line is the AGWB signal from this work.

The purple parabola represents an approximation of the future range of LISA. The teal curve shows the AGWB signal from SN24. The red curve shows the AGWB signal from this thesis.

Certainly, when looking at Figure 3.1 it can be seen that there is indeed no discrepancy when using the two slightly different data sets. Only at relatively high frequencies, there seems to be a minor difference in AGWB. This can be explained by the fact that the two populations, while having the same input parameters, are still slightly different from each other, because it is impossible to identically recreate a dataset in SEBA. However, as can be seen in the figure, the differences between the two models are so small that they are practically negligible.

Moreover, the signal is also significantly higher than the AGWB signal produced by BBHs and BNSs (the green and blue line, respectively). This means that the AGWB signal produced by BWDs is clearly dominant in the AGWB that will be detected by LISA.

3.2 Effect of Different Population Synthesis Models and Metallicities on the AGWB

Now that the results of this thesis have been compared to previous work to ensure accuracy, one of the aims of this thesis can be investigated, namely what the effects of different population synthesis models and metallicities are on the AGWB. To investigate the effect of different population synthesis models on the AGWB signal produced by the mergers of BWDs, the four population synthesis models described in Section 2.3, were each run for the six different metallicities described in the second column of Table 2.1. Each of these results used the SFH as described in Equation 2.30 (Madau & Dickinson, 2014).

Population Synthesis Models with $\alpha\alpha, \alpha = 1$

Figure 3.2 shows the AGWB when the two WDs underwent two α mass transfer phases with α set to 1. The recurring lines in the figure are as in Figure 3.1. The other six colours embody the six different metallicities that were investigated and their corresponding AGWB signal. In general, the shape of each of the lines is similar, it rises relatively steeply, to then flatten slightly, but still continue rising. Afterwards, there is a peak somewhat above a frequency of 10^{-2} Hz, after which it declines. The two smallest metallicities ($Z = 0.0001$ and $Z = 0.001$, the two yellow lines in the figure) give the highest signal. The other four metallicities, especially in the region of interest (LISA's range), are mostly indistinguishable. However, right when the signals pass the edge of LISA's range, the four other metallicities become slightly separated from each other again. But, since this is outside the detectable range for LISA, this will not be observed and is therefore less relevant.

Population Synthesis Models with $\alpha\alpha, \alpha = 4$

The standard features in Figure 3.3 are as in Figure 3.2. The lines for the signal for the AGWB in Figure 3.3 have roughly the same shape compared to the signals in Figure 3.2, especially at the lower frequencies. The difference in input for Figure 3.3 compared to Figure 3.2 is in the population synthesis model. Both common envelope processes are still described by two α mass transfer phases. However, instead of using a numerical value for α of 1, this model uses a numerical value of 4. This change in input parameter gives a clear difference in detected AGWB signal. In this model, the lowest metallicity ($Z = 0.0001$, the lightest yellow line), clearly leads to the lowest signal. All other metallicities are pretty much indistinguishable from each other in the region of interest. Another feature that stands out in this frequency range, is the signal produced using a metallicity of 0.001 (the dark yellow line). It stands out from the other signals, since it does not immediately decrease to 0, but seems to have an intermediate step. This is most likely caused by a single binary system being present at this frequency for this specific population synthesis model and this specific metallicity. Again, this is less relevant since it does not fall in LISA's frequency range, but it is interesting to note. Another important thing to mention is that the signal with the bright red colour ($Z = 0.02$) is the same as the signal shown in the previous section in Figure 3.1, since the previous work only

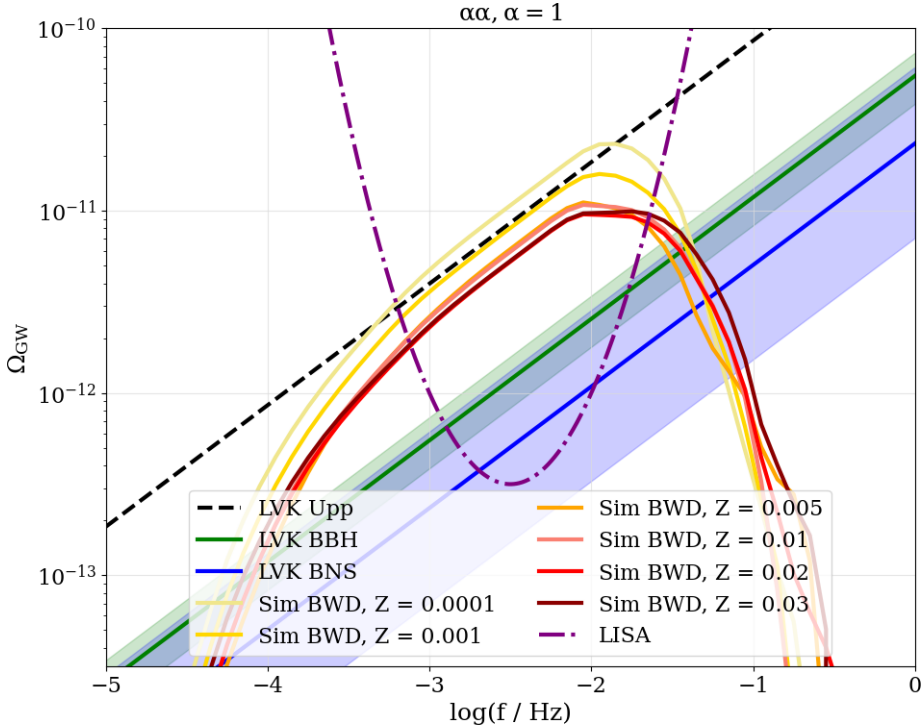


Figure 3.2: As in Figure 3.1, the AGWB for the population synthesis models with two α mass transfer phases ($\alpha\alpha$), with a numerical value for α of 1. Six different metallicities were used, ranging from 0.0001 to 0.03. The SFH is that of Equation 2.30.

looked at the signal for a population synthesis model with two α mass transfer phases and a solar metallicity of the universe ($Z = Z_{\odot} = 0.02$).

Population Synthesis Models with $\gamma\alpha, \alpha = 1$

The AGWB produced by merging BWDs in Figure 3.4 is plotted with the use of a different population synthesis model, compared to the two previous figures (Figure 3.2 and Figure 3.3). The standard elements in Figure 3.4 are the same as those introduced in Figure 3.1. As explained in detail in Chapter 1 (Section 1.1.1) or in Chapter 2 (Section 2.3), instead of two α mass transfer phases, this model uses a γ mass transfer phase as the first phase. This model once again uses a numerical value of 1 for α . The main feature that stands out in this figure, compared to the previous two in this section, is that there are not one or two metallicities that clearly lie above or below the other metallicities. In most of LISA's frequency range, the six metallicities are relatively indistinguishable. However, once all signals have reached their peak (slightly above a frequency of 10^{-2} Hz), some of the metallicities stand out from the rest. Especially the two lowest metallicities ($Z = 0.0001$ and $Z = 0.001$, the two yellow lines), clearly lie higher than the other four metallicities at this frequency.

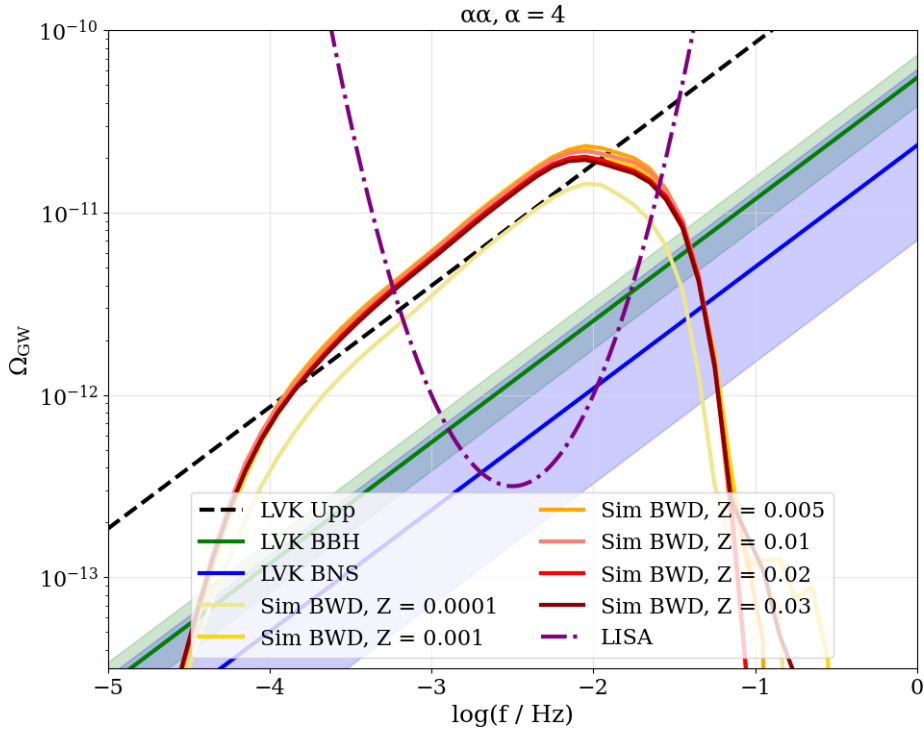


Figure 3.3: As in Figure 3.1, the AGWB for the population synthesis models with two α mass transfer phases ($\alpha\alpha$), with a numerical value for α of 4. Six different metallicities were used, ranging from 0.0001 to 0.03. The SFH is that of Equation 2.30.

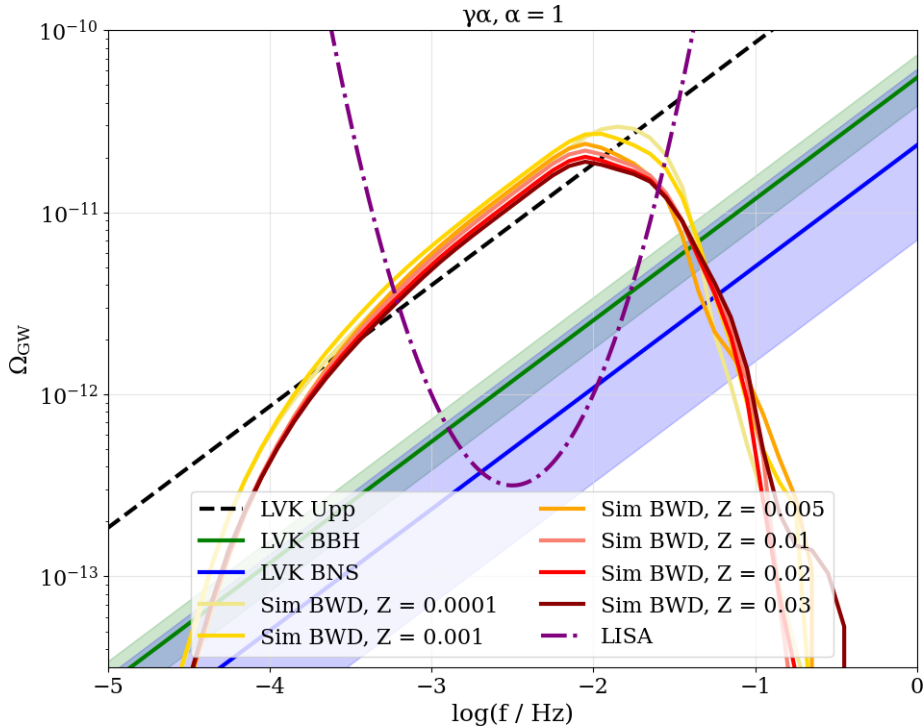


Figure 3.4: As in Figure 3.1, the AGWB for the population synthesis models with one γ and one α mass transfer phase ($\gamma\alpha$), with a numerical value for α of 1. Six different metallicities were used, ranging from 0.0001 to 0.03. The SFH is that of Equation 2.30.

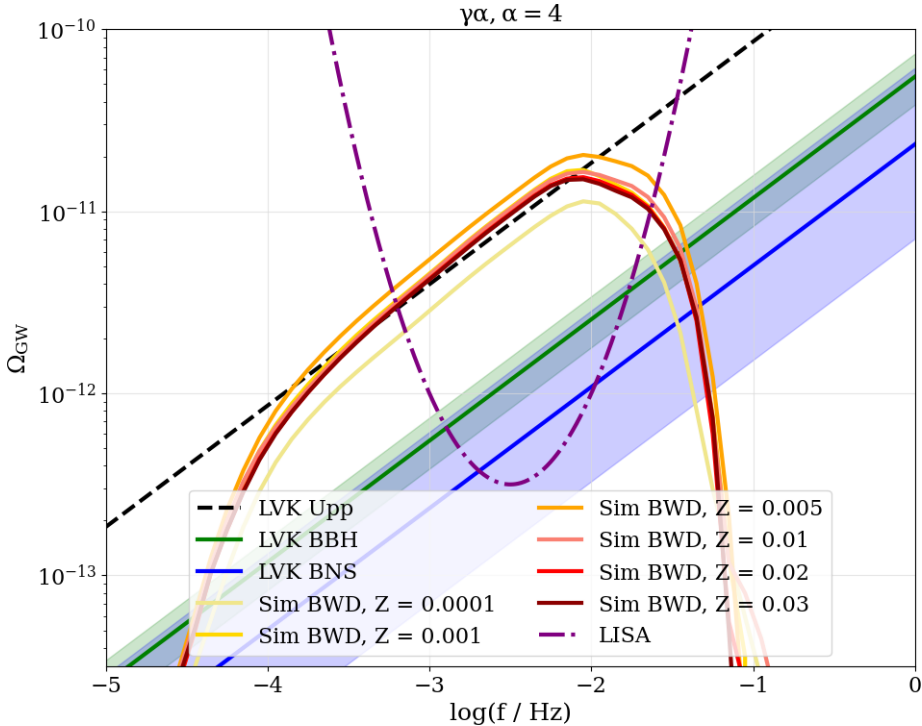


Figure 3.5: As in Figure 3.1, the AGWB for the population synthesis models with one γ and one α mass transfer phase ($\gamma\alpha$), with a numerical value for α of 4. Six different metallicities were used, ranging from 0.0001 to 0.03. The SFH is that of Equation 2.30.

Population Synthesis Models with $\gamma\alpha, \alpha = 4$

The last of the four population synthesis models, with, again, the first mass transfer phase described by γ and the second mass transfer phase described by α , can be seen in Figure 3.5. Here, α has a numerical value of 4. The standard components of Figure 3.5 are the same as those seen in Figure 3.1. Figure 3.5, again has two metallicities that stand out from the rest. The lowest metallicity ($Z = 0.0001$, the light yellow line) is clearly lower than the other metallicities. On the other hand, the orange line, corresponding to a metallicity of $Z = 0.005$, lies slightly higher than the other metallicities. The other four metallicities are again indistinguishable.

3.2.1 Comparison Between Models

There does not seem to be a trend regarding what AGWB signal of what metallicities will lie higher than others. For example, in Figure 3.2, the smallest metallicity, $Z = 0.0001$ lies higher than all others. However, in both models with a numerical value for α of 4, Figures 3.3 and 3.5, the AGWB signal with the lowest metallicity lies below all other metallicities. In Figure 3.4, the line corresponding to $Z = 0.0001$ is indistinguishable from the others, up until the peak. Only at the peak, slightly above 10^{-2} Hz, the lowest metallicity does correspond to the highest signal, as in the other model with a numerical value of α of 1, see Figure 3.2. Thus, aside from possibly the lowest metallicity, there seems to be no direct trend that a certain metallicity leads to a higher or lower AGWB signal.

Comparing all four figures (Figure 3.2 to Figure 3.5), it can be seen that for a population synthesis model of $\alpha\alpha$, $\alpha = 1$, the signals of all six different metallicities are lower than those of the other three models. The signals for the population synthesis model of $\gamma\alpha$, $\alpha = 4$, all lie around the upper limit for the LVK collaboration. The other two population synthesis models ($\alpha\alpha$, $\alpha = 4$ and $\gamma\alpha$, $\alpha = 1$, respectively), have the highest signals of all four population synthesis models.

An explanation that can help understand the difference in AGWB signal between the first two models ($\alpha\alpha$, with $\alpha = 1$ and $\alpha = 4$, respectively) is the fact that a higher numerical value for α leads to a wider orbit (see Section 1.1.1). This means that for the model with α with a numerical value of 1 (which leads to tighter orbits), it is very possible that the system merges before it can go through the second common envelope phase and actually become a BWD. In other words, since it is expected that a higher numerical value for α leads to the creation of more BWD systems, it is not shocking that the AGWB signal for this model is higher than that of the model where α had a numerical value of 1.

On the other hand, using the other models ($\gamma\alpha$, with again α equal to either 1 or 4), the above described issue, where for a numerical value for α of 1 some systems merge before they can become a BWD, is not relevant. The first common envelope phase is exactly the same for both $\gamma\alpha$ models, meaning that only the second common envelope phase (the α phase) has an effect on the AGWB signal. It seems that when the α mass transfer phase in the $\gamma\alpha$ formalism, has a smaller numerical value (i.e. the orbit is tighter), the AGWB signal is slightly greater than when the numerical value for α is larger (i.e. the orbit is wider).

One thing that can be noticed when looking at the shapes of the AGWB signal, is that for models with α equal to 4, the signal decreases very steeply after the peak (around a frequency of 10^{-1} Hz), whereas the signal for the $\alpha = 1$ models, decreases much less steep. The reason for this is the fact that for the population synthesis models with α equal to 1, there is a small but significant portion of the total number of systems that reside at these frequencies (10^{-1} Hz). These systems have high chirp masses (around $1M_\odot$, while the average chirp mass of the full population is somewhere between $0.4M_\odot$ and $0.5M_\odot$, see Table 2.2) which leads to them significantly contributing to the AGWB signal, which means the signal only decreases gradually. For the models where α is equal to 4, there are fewer systems (compared to the total number of systems) present at this frequency, meaning that the contribution of these systems to the AGWB is pretty much negligible. This leads to the drastic steep decrease in AGWB signal for these population synthesis models.

Physically, a higher AGWB signal can come from three different factors. The first factor is chirp masses, higher chirp masses lead to a higher signal. This can clearly be seen when looking at Equation 2.26, where Ω is dependent on the chirp mass. Also the number of systems has an effect on the AGWB signal, where a higher number of systems leads to a higher signal. The last factor that has an influence on the detected AGWB signal is the redshift of the systems. If there are for example 10 systems at a redshift of 1 and 10 systems at a redshift of 8, the signal produced by the systems at a redshift of 1 will be larger than the signal produced by the (same number of) systems at a redshift of 8.

Table 3.1: The number of systems for each of the choices of population synthesis model and each of the six metallicities, respectively. The SFH used is that of Madau & Dickinson (2014)

Z	$\alpha\alpha, \alpha = 1$	$\alpha\alpha, \alpha = 4$	$\gamma\alpha, \alpha = 1$	$\gamma\alpha, \alpha = 4$
0.0001	$9.06 \cdot 10^{16}$	$2.15 \cdot 10^{17}$	$1.72 \cdot 10^{17}$	$1.86 \cdot 10^{17}$
0.001	$6.31 \cdot 10^{16}$	$2.65 \cdot 10^{17}$	$2.03 \cdot 10^{17}$	$2.95 \cdot 10^{17}$
0.005	$3.14 \cdot 10^{16}$	$2.55 \cdot 10^{17}$	$1.33 \cdot 10^{17}$	$2.87 \cdot 10^{17}$
0.01	$2.90 \cdot 10^{16}$	$2.51 \cdot 10^{17}$	$1.48 \cdot 10^{17}$	$2.84 \cdot 10^{17}$
0.02	$2.63 \cdot 10^{16}$	$2.44 \cdot 10^{17}$	$1.40 \cdot 10^{17}$	$2.70 \cdot 10^{17}$
0.03	$2.89 \cdot 10^{16}$	$2.39 \cdot 10^{17}$	$1.36 \cdot 10^{17}$	$2.69 \cdot 10^{17}$

The number of systems can be determined, using the following formula:

$$N(z, f) = (4\pi \cdot \chi(z)^2 \cdot \Delta\chi(z)) \cdot n(z, f) \quad (3.1)$$

where $n(z, f)$ is the number density of systems in each bin, which is defined as follows:

$$n(z, f) = \sum_k \frac{\psi(z; k)}{3.4 \cdot M_\odot} \cdot \tau(z, f; k). \quad (3.2)$$

Table 3.1 shows the number of systems per metallicity for each of the possibilities for the population synthesis model. The first thing that can be seen is that column 2 (representing the population synthesis model $\alpha\alpha, \alpha = 1$), clearly has the lowest number of systems. This explains the fact that the corresponding AGWB signals are clearly lower compared to other population synthesis models. As mentioned before, the reason for this is most likely the fact that several systems have already merged before a BWD was formed. Table 3.1 also shows that the two population synthesis models with a numerical value for α of 4 clearly lead to the most number of systems. However, $\gamma\alpha, \alpha = 1$ is only slightly lower. The number of systems can therefore be considered an important factor that affects the corresponding strength of the AGWB, however, it is not the only factor (as mentioned before) that has to be taken into account. This is because with just the table, the conclusion might be that the two population synthesis models with a numerical value for α of 4 lead to the highest AGWB signals. However, looking at the figures, it seems that $\gamma\alpha$ with a numerical value of 1 for α leads to higher signals than $\gamma\alpha$ with a numerical value of 4 for α .

As mentioned in Section 2.3 (see Table 2.2), the average chirp masses are fairly close to each other. This suggests that the strength of the AGWB is less influenced by this, in the sense that each of the metallicities and population synthesis models will have a roughly equal contribution of chirp masses to the AGWB signal strength.

Finally looking at the redshift where the systems are situated gives Figure 3.6. The bottom panel in this figure, shows the contribution of each redshift, per frequency bin, to the full AGWB signal. The top panel shows the number of systems per frequency bin. The specific model plotted is $\gamma\alpha$, with $\alpha = 4$, with a metallicity of $Z = 0.02 (Z_\odot)$. The SFH by Madau & Dickinson (2014) was used. When looking at this figure, it is clear to see that high redshifts (higher than 4.40) do not contribute to the AGWB signal. Only for low frequencies do the higher redshifts (roughly between 2 and 4.40) contribute marginally

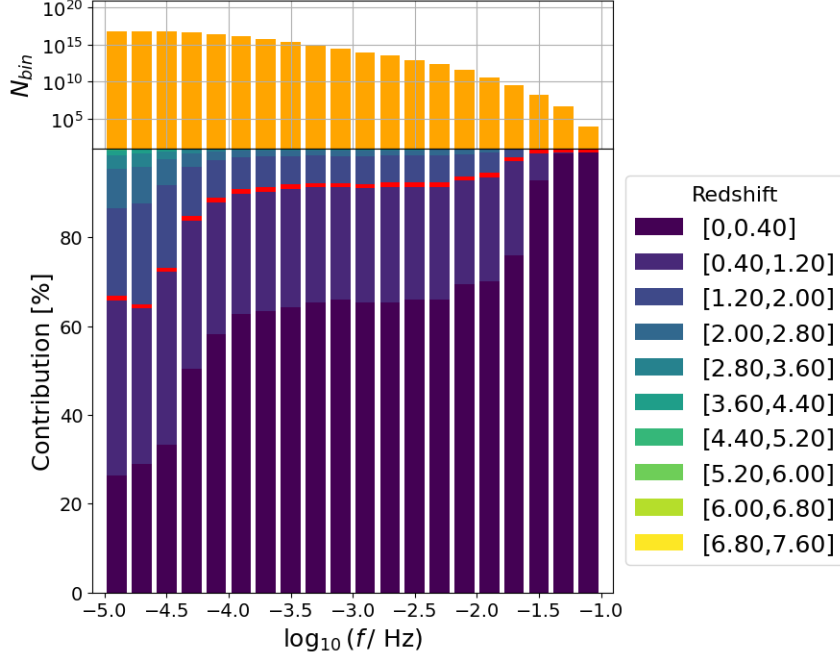


Figure 3.6: The bottom panel shows the contribution (in percentage) of each redshift bin to the AGWB signal. The red line represents a redshift of 0.46. The AGWB signal’s contribution is binned in 20 frequency bins. The top panel shows the number of systems present in each of the frequency bins, respectively. The population synthesis model plotted here is $\gamma\alpha$, with $\alpha = 4$ and with a metallicity of $Z = 0.02$ (Z_\odot). The SFH by Madau & Dickinson (2014) was used.

to the AGWB signal. It is clear to see that the main contribution to the AGWB signal comes from systems residing below a redshift of about 1.2, especially when moving to higher frequencies. This figure is used as an example, since other population synthesis models lead to roughly similar results (see Appendix A for all figures), namely that only low redshifts contribute to the AGWB. Since there are no large differences between population synthesis models, it is safe to say that the redshifts at which the systems reside all have a similar effect for their corresponding AGWB signal. Since the redshift contributions are not identical, there can be a small difference in effect, but this will be almost negligible.

It again is clear to see in all four figures, that the AGWB signal produced by BWDs is dominant over the AGWB signal produced by BBHs and BNSs. This means that the AGWB detected by LISA will be largely made up of the BWD AGWB signal.

3.3 Effect of a (Moderate) Metallicity Dependent SFRD on the AGWB

The SFH used in the previous section (Section 3.2) will never correctly describe the SFH of the whole universe. This is because it assumes that there is just one single SFH at a certain redshift, while this is not the case in our universe. Using a SFH that is dependent on metallicity as well as redshift, more accurately describes the universe. The results for the AGWB produced by merging BWDs when this is taken into account, is shown in this section. One thing to take into account is that in Section 3.2, the total SFH is used for each of the input files with initial values. In this section, only the SFRD that falls in one of the six corresponding bins (see Section 2.1.2.2, second column of Table 2.1) is used. This means that comparing the two SFHs (or SFRDs) per metallicity cannot be done accurately, since one describes the total SFH while the other only describes part of the total SFRD.

Population Synthesis Models with $\alpha\alpha, \alpha = 1$

Figure 3.7 shows the AGWB signal (Ω) for each of the six metallicity bins, the dashed lines (with the exception of the dashed black line), as well as the sum of all six lines (the solid light green line) for the population synthesis model $\alpha\alpha$ with α equal to a numerical value of 1. The other lines are as described in Figure 3.1. The AGWB signal due to the metallicity bin around a metallicity of 0.01 (dashed salmon line) is clearly the highest, while the AGWB signal due to the metallicity bin around a metallicity of 0.03 (dashed dark red line) is the lowest (at least in LISA's frequency range). This is not necessarily surprising, since the metallicity bin around a metallicity of 0.01 consists of the highest value of SFRD, as seen in Figure 2.2. Similarly, the metallicity bin around 0.03 contains one of the lowest amounts of SFRD as seen in aforementioned Figure 2.2. The other four dashed lines are pretty much indistinguishable from each other in LISA's range. An important thing to note again, is that the signals represented by the dotted lines are relatively low compared to the plots in the previous section, since only a part of the total SFRD was used to determine the AGWB signal, whereas in the previous section, the total SFH was used.

Population Synthesis Models with $\alpha\alpha, \alpha = 4$

Figure 3.8 is similar to the previous figure, Figure 3.7, with the difference being the population synthesis model that was used. Again the usual components as introduced in Figure 3.1 are also shown in this figure. To be precise, in this figure, $\alpha\alpha$ with α with a numerical value of 4 was used as the population synthesis model. Similarly to before, the AGWB signal that lies highest is the one simulated using the bin with a metallicity around 0.01 (dashed salmon line). This signal is closely followed by the AGWB signals from the metallicity bins around 0.005 (dashed orange line) and 0.02 (dashed red line), respectively. The three aforementioned metallicity bins are also the three bins pertaining to the highest values of total SFRD. The signals representing the metallicity bins around 0.001 (dashed (darker) yellow line) and 0.03 (dashed dark red line) lie even slightly lower.

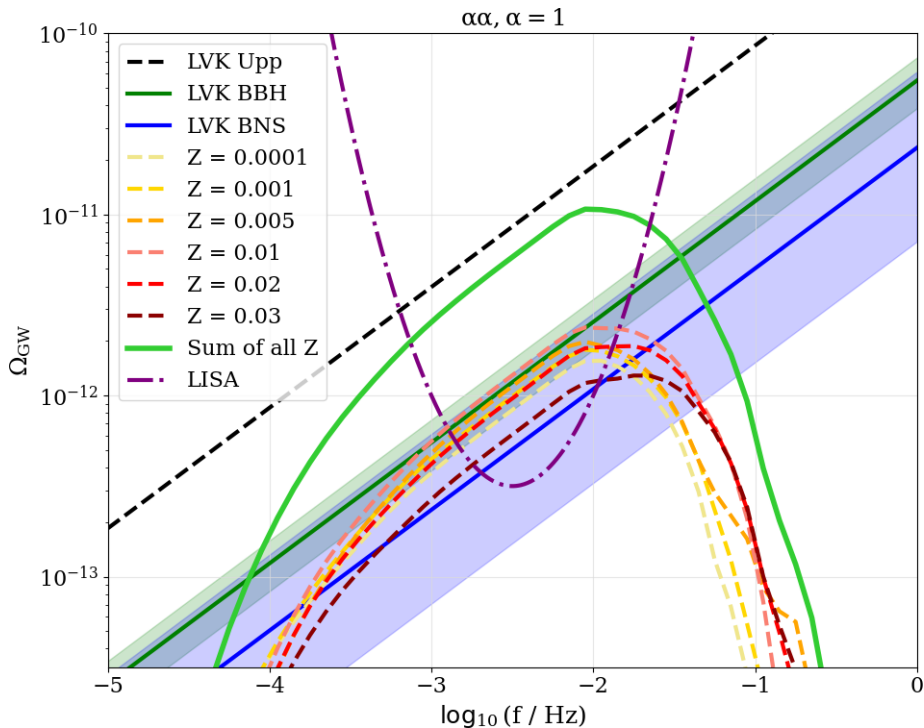


Figure 3.7: As in Figure 3.1, the AGWB for the population synthesis models with two α mass transfer phases ($\alpha\alpha$), with a numerical value for α of 1. Six different metallicities were used, ranging from 0.0001 to 0.03. The MZ19 SFRD model was used. The dashed lines (with the exception of the black dashed line) are the AGWB signals from each of the six separate metallicity bins, the solid light green line is the sum of all six AGWB signals.

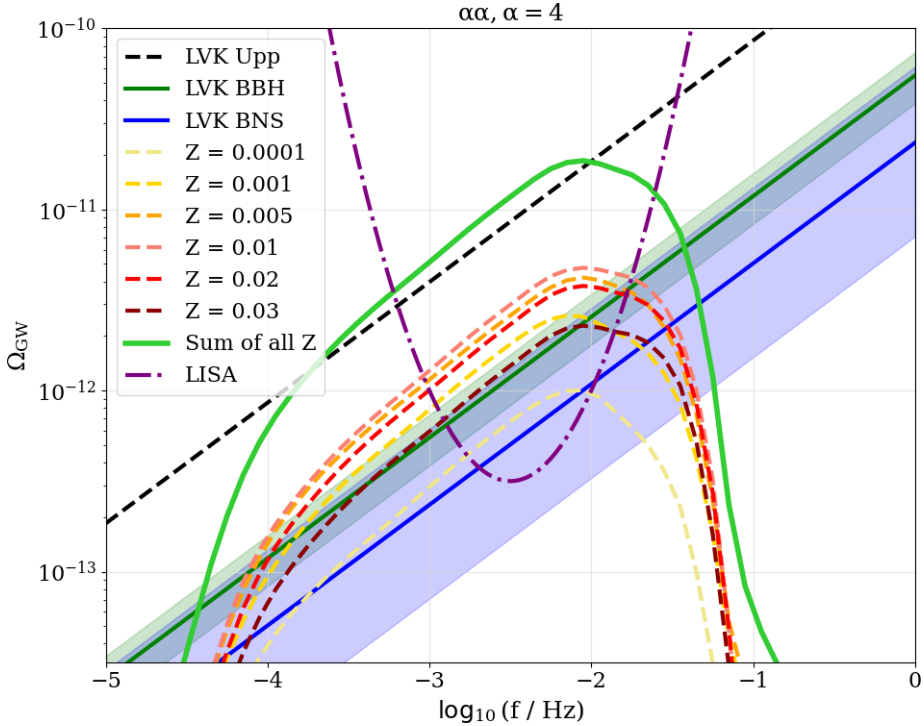


Figure 3.8: As in Figure 3.1, the AGWB for the population synthesis models with two α mass transfer phases ($\alpha\alpha$), with a numerical value for α of 4. Six different metallicities were used, ranging from 0.0001 to 0.03. The MZ19 SFRD model was used. The dashed lines (with the exception of the black dashed line) are the AGWB signals from each of the six separate metallicity bins, the solid light green line is the sum of all six AGWB signals.

Evidently, the lowest metallicity bin (around 0.0001, the dashed lightest yellow line) produces the lowest AGWB signal. Again, the order of the last three lines roughly follows the order shown in Figure 2.2. However, the fact that here the lowest AGWB signal is the signal surrounding the metallicity 0.0001, while in the previous figure (Figure 3.7) it was the signal relating to a metallicity of 0.03, shows that a different population synthesis model has a different effect on the AGWB signal. In other words, the total values of SFRD present in each of the metallicity bins is not the dominant factor that affects the strength of the AGWB signal, since the choice of population synthesis model leads to different possibilities. Nevertheless, Figure 2.2 does give a rough approximation of the strength of the AGWB signals coming from each of the metallicity bins, even if the exact order might be slightly changed. The sum (the solid light green line) clearly lies higher than the sum of the previous plot (Figure 3.7). This solidifies the conclusion from the previous section (Section 3.2) that a population synthesis model with two α mass transfer processes with a numerical value of 4, yields a higher AGWB signal than the same population synthesis model with a numerical value of 1.

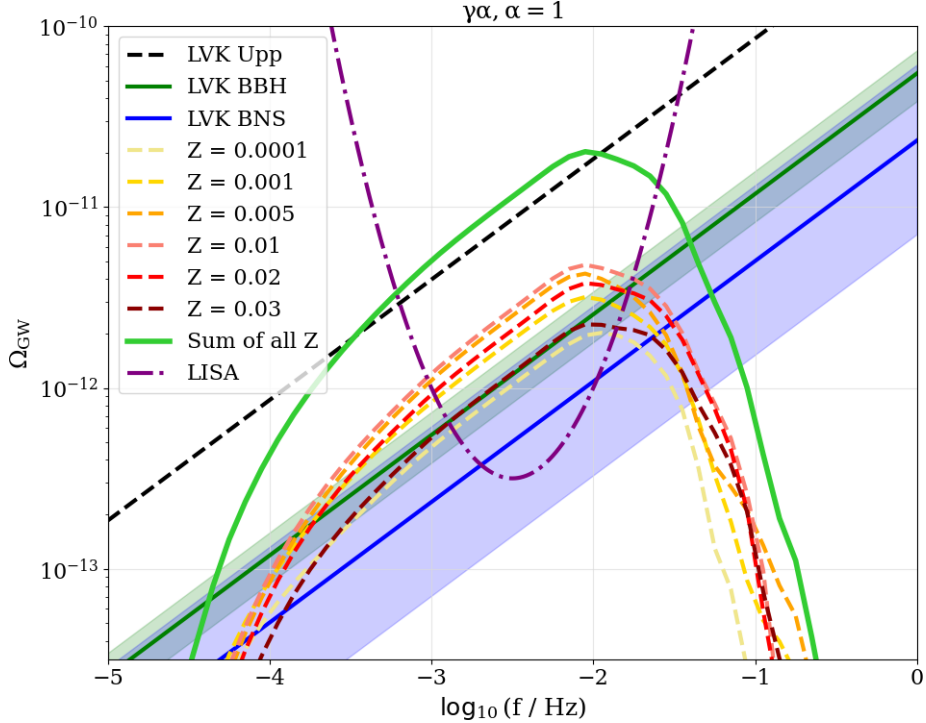


Figure 3.9: As in Figure 3.1, the AGWB for the population synthesis models with one γ and one α mass transfer phase ($\gamma\alpha$), with a numerical value for α of 1. Six different metallicities were used, ranging from 0.0001 to 0.03. The MZ19 SFRD model was used. The dashed lines (with the exception of the black dashed line) are the AGWB signals from each of the six separate metallicity bins, the solid light green line is the sum of all six AGWB signals.

Population Synthesis Models with $\gamma\alpha, \alpha = 1$

Changing the population synthesis model from $\alpha\alpha$ to $\gamma\alpha$ and changing the numerical value for α back to 1, leads to the results as shown in Figure 3.9. Again, the standard features are as those described in Figure 3.1. Figure 3.9 also has the AGWB signal corresponding to the metallicity bin around 0.01 (dashed salmon line) as the highest signal. Following this are the AGWB signal for the metallicity bins corresponding to a metallicity of 0.005, 0.02 and 0.001 (the dashed orange, red and dark yellow line, respectively). Then, slightly lower come the other metallicities. First, the AGWB signal corresponding to the highest metallicity bin (the dashed dark red line, a metallicity of 0.03), and as the lowest AGWB signal the lowest metallicity bin of 0.0001 (the dashed light yellow line). Once more, the order of the AGWB signals for each of the six metallicity bins is relatively close to the order shown in Figure 2.2. Furthermore, the sum of all six metallicity bins (the solid light green line) is (again) higher than that of the first figure shown in this section (Figure 3.7). The strength of the AGWB signal is somewhat comparable to the AGWB signal from the previous figure, Figure 3.8.

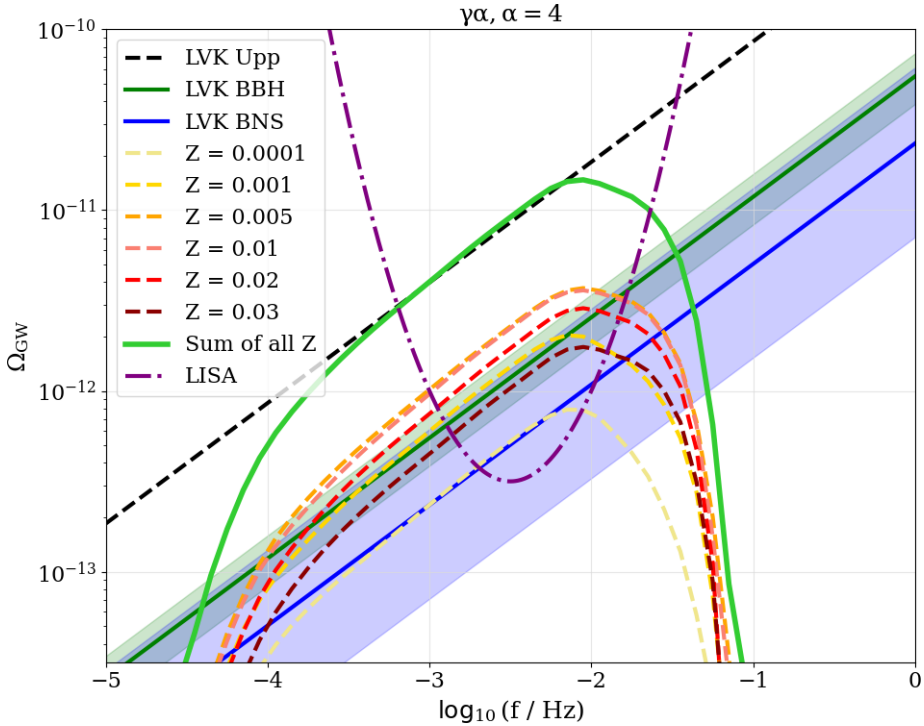


Figure 3.10: As in Figure 3.1, the AGWB for the population synthesis models with one γ and one α mass transfer phase ($\gamma\alpha$), with a numerical value for α of 4. Six different metallicities were used, ranging from 0.0001 to 0.03. The MZ19 SFRD model was used. The dashed lines (with the exception of the black dashed line) are the AGWB signals from each of the six separate metallicity bins, the solid light green line is the sum of all six AGWB signals.

Population Synthesis Models with $\gamma\alpha, \alpha = 4$

Figure 3.10 shows the last result of this section, namely the AGWB signal when using a population synthesis model $\gamma\alpha$ with a numerical value of α of 4. The usual components of this figure are as seen and described in Figure 3.1. The metallicity bins leading to the highest AGWB signal are those surrounding a metallicity of 0.01 and of 0.005 (or the dashed salmon or orange line, respectively). Following these metallicity bins, are the bins surrounding the metallicities of 0.02, 0.001 and 0.03 (the dashed red, dark yellow and dark red line, respectively). The lowest AGWB signal comes from the metallicity bin encompassing the lowest metallicity, namely 0.0001 (the lightest yellow line). Again, somewhat expectedly, the order of the AGWB signals is relatively similar to the order of the total amounts of SFRD in each of the metallicity bins (as seen in Figure 2.2). The sum of all six bins (the solid light green line) lies slightly lower than the sum in both Figure 3.8 and Figure 3.9. However, it does lie significantly higher than that in Figure 3.7.

3.3.1 Comparison Between Models

Comparing all four figures (Figure 3.7 to Figure 3.10) of the different population synthesis models, there does seem to be a trend present in the order of the metallicity bins, when using the metallicity dependent SFRD. For all four possibilities of the population synthesis models, the two lowest signals in LISA’s range come from the two outermost metallicity bins, namely the metallicity bin surrounding the lowest metallicity (0.0001, the dashed light yellow line in all plots) and the metallicity bin surrounding the highest metallicity (0.03, the dashed dark red line in all plots). In general the bin surrounding the lowest metallicity (0.0001, the light yellow dashed line in all plots) is the lowest, with the exception for the population synthesis model where $\alpha\alpha$ has a numerical value for α of 1, where this bin leads to the penultimate AGWB signal. The fact that these two metallicity bins lead to the lowest AGWB signals is not surprising, since it is expected that our universe will not be comprised of large volumes of these extreme metallicities. As mentioned before, these two bins being the lowest, can also already be seen in the distribution of SFRD per metallicity bin, as seen in Figure 2.2. This figure clearly shows the lowest amounts of SFRD in these two metallicity bins (surrounding 0.03 and 0.0001). It also shows that the metallicity bin surrounding 0.01 has the highest amount of SFRD, which is then shown in the figures in this current section, where the AGWB signal using this metallicity bin is (one of) the highest AGWB signal compared to the other metallicity bins.

Furthermore, the finding from the previous section (Section 3.2) that the population synthesis models with $\alpha\alpha$, $\alpha = 4$, and $\gamma\alpha$, $\alpha = 1$, lead to higher AGWB signals than the other two possibilities, is confirmed in this section. Moreover, in this section it is also, again, clearly shown that the population synthesis model that leads to the lowest predicted AGWB signal is that of the $\alpha\alpha$ population synthesis model with α with a numerical value of 1. As explained in Section 3.2.1, the reason that the $\alpha\alpha$, $\alpha = 1$ model leads to the lowest AGWB signal is most likely because in this case some binaries do not survive after the first common envelope phase, because of the tight orbits that result from the first common envelope phase. For the other $\alpha\alpha$ model this is not a problem, since here the orbits are a lot wider. On top of that, again, the γ common envelope phase does not differ between the two $\gamma\alpha$ models, meaning that in this case there is no difference after the first common envelope phase. In the case of a $\gamma\alpha$ population synthesis model, it seems that a lower α might lead to more systems and thus a higher AGWB signal than a higher numerical value for α . Aside from the number of systems, a higher AGWB signal can also come from at what redshift these systems reside at, as well as the chirp masses of the systems, as mentioned in Section 3.2.1

Moreover, the figures shown in this section, also show the characteristic described in the previous section, namely that population synthesis models with α equal to 4, decrease much more steeply at a frequency around 10^{-1} Hz, than the models where α is equal to 1. Again this can be explained by the fact that around these frequencies, there are relatively more systems (compared to the total amount of systems) for models with α is equal to 1. These systems have significantly higher chirp masses than compared to the average of the full population, which leads to them being able to lead to some AGWB signal at these frequencies.

Table 3.2: The number of systems for each of the choices of population synthesis model and each of the six metallicities, respectively. The bottom row shows the total number of systems for each of the population synthesis models. The SFRD used is the MZ19 model.

Z	$\alpha\alpha, \alpha = 1$	$\alpha\alpha, \alpha = 4$	$\gamma\alpha, \alpha = 1$	$\gamma\alpha, \alpha = 4$
0.0001	$1.11 \cdot 10^{16}$	$2.22 \cdot 10^{16}$	$2.08 \cdot 10^{16}$	$1.95 \cdot 10^{16}$
0.001	$1.05 \cdot 10^{16}$	$4.23 \cdot 10^{16}$	$3.32 \cdot 10^{16}$	$4.67 \cdot 10^{16}$
0.005	$6.33 \cdot 10^{15}$	$5.20 \cdot 10^{16}$	$2.71 \cdot 10^{16}$	$5.81 \cdot 10^{16}$
0.01	$5.69 \cdot 10^{15}$	$5.00 \cdot 10^{16}$	$2.97 \cdot 10^{16}$	$5.78 \cdot 10^{16}$
0.02	$3.66 \cdot 10^{15}$	$3.40 \cdot 10^{16}$	$2.01 \cdot 10^{16}$	$3.98 \cdot 10^{16}$
0.03	$2.10 \cdot 10^{15}$	$1.78 \cdot 10^{16}$	$1.05 \cdot 10^{16}$	$2.16 \cdot 10^{16}$
Sum	$3.94 \cdot 10^{16}$	$2.18 \cdot 10^{17}$	$1.41 \cdot 10^{17}$	$2.44 \cdot 10^{17}$

Table 3.2 shows the number of systems for each of the four population synthesis models. The number of systems for each of the separate metallicities is shown, as well as the sum of all six metallicities. Again, the number of systems for each of the metallicities cannot be directly compared to the number of systems for each of the metallicities in Table 3.1, since here the SFRD is binned in six bins. The highest metallicity ($Z = 0.03$) and the lowest metallicity ($Z = 0.0001$) lead to the lowest number of systems, which can also be seen in the corresponding figures. Looking at the sums, it is clear to see that $\alpha\alpha$ with $\alpha = 4$ and $\gamma\alpha$ with $\alpha = 4$, again have the highest number of systems. $\gamma\alpha$ with $\alpha = 1$ is relatively close in number of systems, the sum only being a factor of roughly 1.5 smaller than the two highest population synthesis. The lowest number of systems is clearly from the $\alpha\alpha$ with α equal to 1 model, which again can also be seen in the corresponding figure.

As mentioned in Section 3.2.1, since the (average) chirp masses barely show any differences. While the chirp mass does have a significant effect on the AGWB, since the (average) chirp masses are practically identical, the effect of the chirp mass on the AGWB will be practically identical as well.

Again, since the redshift contribution figures (as the one in Figure 3.6, see Appendix A for all figures, here Figure A.6 is most relevant), are relatively similar for each of the choices in population synthesis model, it is expected that this property will not be the cause of very clear distinctions between the AGWBs. Perhaps only the $\alpha\alpha, \alpha = 1$ shows that some systems reside at slightly higher redshifts compared to the other three models, but again, this difference is very small.

In general, the separate AGWB signals per metallicity bins (the dashed lines) are either of the same order of magnitude or perhaps slightly larger than the AGWB signal emitted by BBHs and BNSs. However, since it will be the sum (the solid light green line) that will be measured by LISA and this signal clearly lies a lot higher than the signals produced by BBHs and BNSs, it can be said quite confidently that the AGWB signal detected by LISA will be dominated by BWDs.

3.4 Comparing Different Types of Metallicity Dependent SFRDs

To investigate the effect that different metallicity dependent SFRD models have on the AGWB, the total signals (sums) of all five models (LZ19, MZ19, HZ19, LZ21 and HZ21, for more information see Section 2.1.2.2) are studied. The total signal was already represented in the previous section (Section 3.3) as the solid light green line. In this section, this was repeated for the four other models. The total results from the previous section (solid light green line) were plotted among the other four models, leading to the following results.

Population Synthesis Models with $\alpha\alpha, \alpha = 1$

Figure 3.11 shows the sums of the AGWB signals from the five different metallicity dependent SFRD models. The standard features are as in Figure 3.1. The light green line shows the MZ19 model, which is the same as shown in the figures in Section 3.3 (Figures 3.7 to 3.10). Below this line is the sum of the AGWB signal coming from the LZ19 model (yellow line). Slightly above this line is the HZ19 model (light blue line). The LZ21 and HZ21 models (a sky blue line and a dark blue line, respectively) lead to the two highest AGWB signals, with the HZ21 model leading to the highest AGWB signal. Looking at the total amounts of SFRD present in each of these models (see Figure 2.1), this result is not extremely surprising. The way the models are ordered in total SFRD is the exact same sequence as that of the sum of the AGWB signals.

Population Synthesis Models with $\alpha\alpha, \alpha = 4$

Figure 3.12 is very similar to Figure 3.11. Again, the standard features in this plot are the same as seen in Figure 3.1. The main difference is the numerical value for α , which was increased to a numerical value of 4 instead of 1. The order of the AGWB signals is exactly the same as in the previous figure. The models from 2019 lead to the lowest AGWB signal, going from the LZ19 model, to the MZ19 model and lastly to the HZ19 model. The two highest AGWB signals are the models from 2021, with the LZ21 model slightly lower than the HZ21 model. Again, this sequence was expected when comparing the sequence to the way the total amounts of SFRD present in each of the models were ordered, as seen in Figure 2.1. One thing that differs between Figure 3.11 and Figure 3.12 is the strength of the AGWB signal. The AGWB signal coming from a population synthesis model with α equal to a numerical value of 4 is clearly significantly higher than the AGWB signal when α is equal to a numerical value of 1. This result further solidifies the claim from the previous two sections (Section 3.2 and 3.3) that from the population synthesis models with two α mass transfer processes, α with a numerical value of 4 leads to a higher AGWB signal.

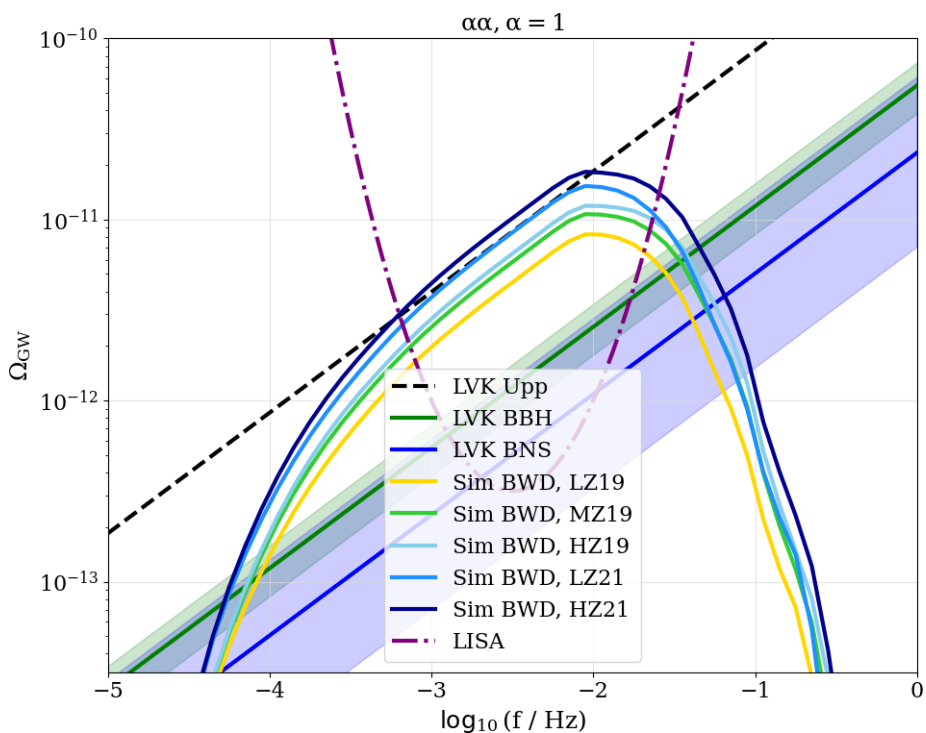


Figure 3.11: As in Figure 3.1, the AGWB for the population synthesis models with two α mass transfer phases ($\alpha\alpha$), with a numerical value for α of 1. Six different metallicities were used, ranging from 0.0001 to 0.03. A metallicity dependent SFRD was used. Each line represents the sum of the AGWB signal for a different SFRD model.

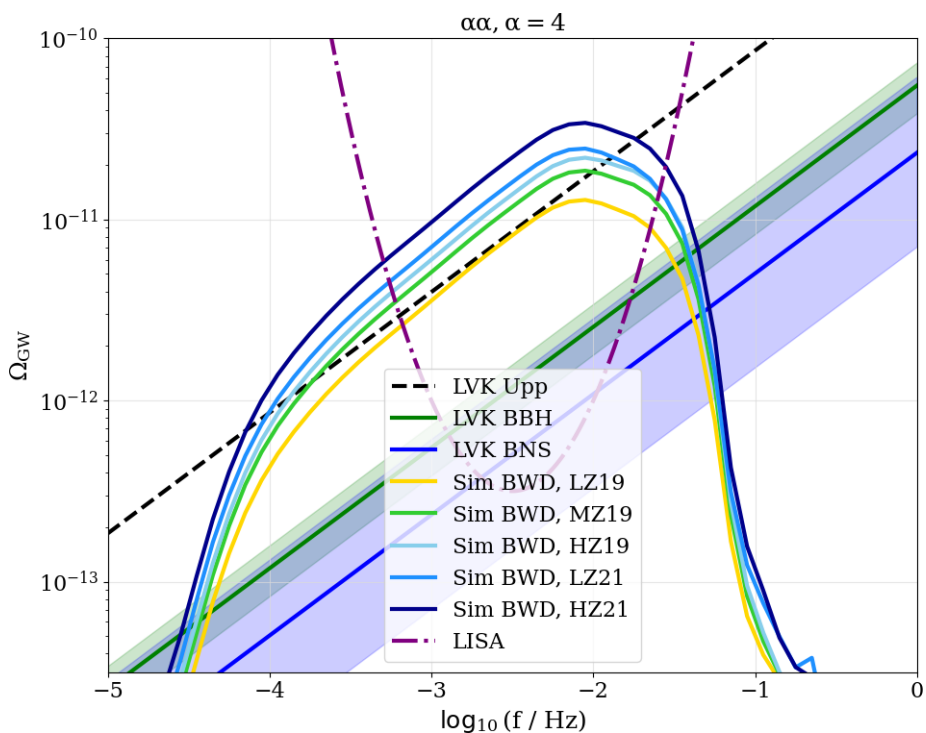


Figure 3.12: As in Figure 3.1, the AGWB for the population synthesis models with two α mass transfer phases ($\alpha\alpha$), with a numerical value for α of 4. Six different metallicities were used, ranging from 0.0001 to 0.03. A metallicity dependent SFRD was used. Each line represents the sum of the AGWB signal for a different SFRD model.

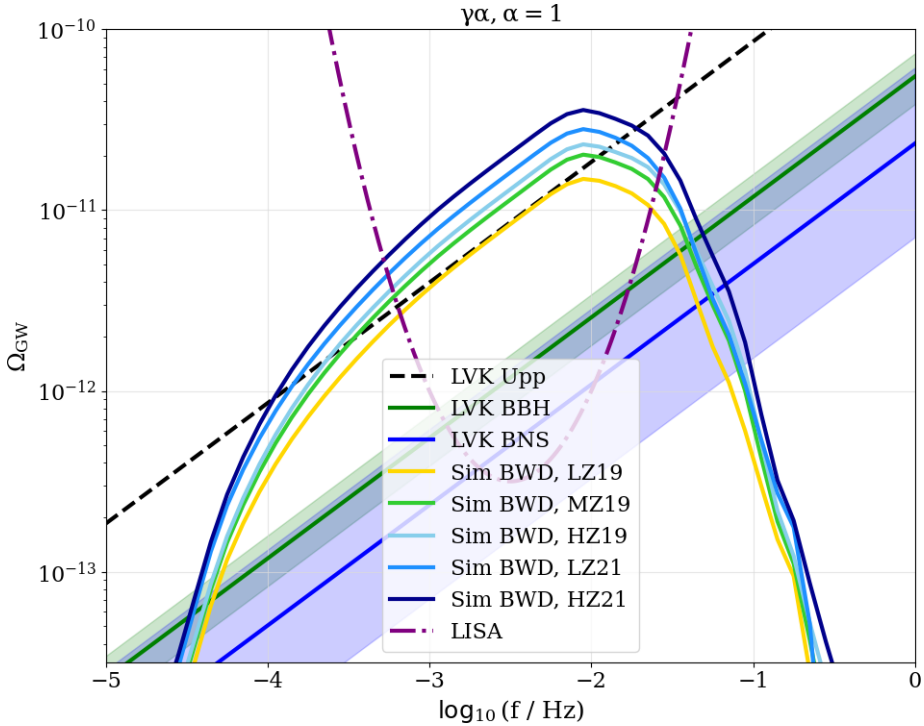


Figure 3.13: As in Figure 3.1, the AGWB for the population synthesis models with one γ and one α mass transfer phase ($\gamma\alpha$), with a numerical value for α of 1. Six different metallicities were used, ranging from 0.0001 to 0.03. A metallicity dependent SFRD was used. Each line represents the sum of the AGWB signal for a different SFRD model.

Population Synthesis Models with $\gamma\alpha, \alpha = 1$

Going from the population synthesis models with two α mass transfer processes, to the models where the first mass transfer process is described by γ and the second mass transfer process is described by α (with α equal to 1) gives the results as shown in Figure 3.13. This figure contains the same standard elements as in Figure 3.1. A bit unsurprisingly, the sequence of the five different models is the same as in the previous two figures in this section (Figures 3.11 and 3.12). Moreover, as mentioned in previous section, the choice for population synthesis model (in this case $\gamma\alpha, \alpha = 1$), leads to a higher AGWB signal than that of the $\alpha\alpha, \alpha = 1$ population synthesis model. The resulting AGWB signal is however, again, similar in strength compared to the $\alpha\alpha, \alpha = 4$ population synthesis model.

Population Synthesis Models with $\gamma\alpha, \alpha = 4$

Lastly, the results for the population synthesis model with the $\gamma\alpha$ mass transfer processes with α with a numerical value of 4, are shown in Figure 3.14. The standard features in the figure are again the same as in Figure 3.1. As expected, the order of the five models is unchanged, going from the LZ19 model, to the MZ19 model, to the HZ19 model. To then go from the LZ21 model to the HZ21 model. Again, the AGWB signal is slightly larger than for the $\alpha\alpha, \alpha = 1$ population synthesis model.

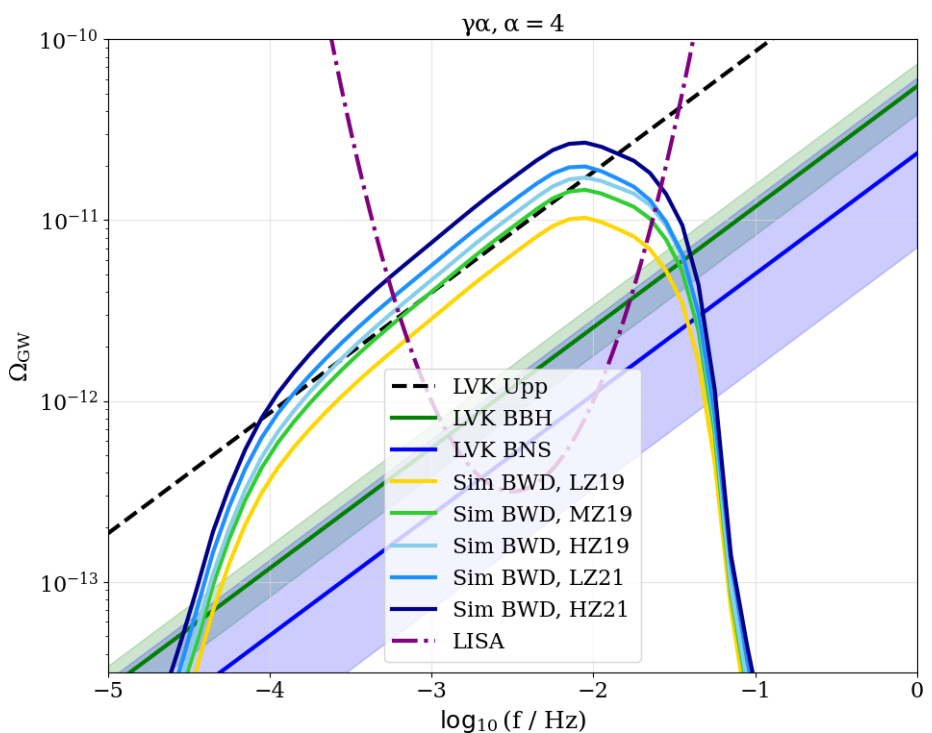


Figure 3.14: As in Figure 3.1, the AGWB for the population synthesis models with one γ and one α mass transfer phase ($\gamma\alpha$), with a numerical value for α of 4. Six different metallicities were used, ranging from 0.0001 to 0.03. A metallicity dependent SFRD was used. Each line represents the sum of the signal for a different SFRD model.

3.4.1 Comparison Between Models

Similarly to previous sections, the population synthesis model with $\alpha\alpha$, $\alpha = 1$, leads to the lowest AGWB signal. $\alpha\alpha$, $\alpha = 4$ and $\gamma\alpha$, $\alpha = 1$, again lead to the highest AGWB signal. However, in this case $\gamma\alpha$, $\alpha = 4$ does not seem to differ that much in AGWB signal strength. Again, the explanation for the relative low AGWB signal for the $\alpha\alpha$, $\alpha = 1$ model is that some systems in this population synthesis model do not survive the first common envelope phase, as explained in more detail in Section 3.2.1, while for a higher value of α more systems survive. Moreover, also as explained before, the first common envelope phase in the $\gamma\alpha$ population synthesis models is exactly the same for both models, meaning only the second common envelope phase (α) has an effect on the AGWB signal. Once more, a more detailed explanation can be found in Section 3.2.1.

Furthermore, as also mentioned in previous sections, the shape of the AGWB signal at high frequencies again differs between the different numerical values for α . As aforementioned, this can be explained by the fact that there are relatively more systems (when set against the total number of systems) for models with α equal to 1, than when the numerical value is 4. This leads to the more gradual decrease at high frequencies for models where α is equal to 1, compared to the steep and drastic decrease when α is equal to 4.

Tables 3.3 to 3.6 represent the number of systems per metallicity per population synthesis model for each of the four SFRD models used in this work (LZ19, HZ19, LZ21 and HZ21), MZ19 was shown in the previous section (see Table 3.2). Something that all four tables have in common, when looking at the sums, is the fact that population synthesis models with a numerical value for α of 4, lead to the highest number of systems. Close to these numbers, is the number of systems for a population synthesis model of $\gamma\alpha$ where α is equal to 1. Again, this is not immediately visible when looking at the corresponding figures, meaning that aside from number of systems there are indeed other factors affecting the strength of the AGWB signal. $\alpha\alpha$ with α equal to 1 clearly leads to the lowest number of systems. However, this is as expected, since it is anticipated that some of the systems in this model will merge before being able to become a BWD. The low metallicity models (LZ19 and LZ21) clearly have the lowest number of systems at the highest metallicities, as expected. The high metallicity have a peak of number of systems at a metallicity of either 0.01 or 0.02, again, also as expected.

Table 3.3: The number of systems for each of the choices of population synthesis model and each of the six metallicities, respectively. The bottom row shows the total number of systems for each of the population synthesis models. The SFRD used is the LZ19 model.

Z	$\alpha\alpha, \alpha = 1$	$\alpha\alpha, \alpha = 4$	$\gamma\alpha, \alpha = 1$	$\gamma\alpha, \alpha = 4$
0.0001	$1.30 \cdot 10^{16}$	$2.72 \cdot 10^{16}$	$2.46 \cdot 10^{16}$	$2.37 \cdot 10^{16}$
0.001	$1.19 \cdot 10^{16}$	$4.86 \cdot 10^{16}$	$3.79 \cdot 10^{16}$	$5.39 \cdot 10^{16}$
0.005	$5.82 \cdot 10^{15}$	$4.77 \cdot 10^{16}$	$2.48 \cdot 10^{16}$	$5.35 \cdot 10^{16}$
0.01	$3.31 \cdot 10^{15}$	$2.92 \cdot 10^{16}$	$1.74 \cdot 10^{16}$	$3.38 \cdot 10^{16}$
0.02	$1.14 \cdot 10^{15}$	$1.06 \cdot 10^{16}$	$6.24 \cdot 10^{15}$	$1.23 \cdot 10^{16}$
0.03	$3.03 \cdot 10^{14}$	$2.57 \cdot 10^{15}$	$1.52 \cdot 10^{15}$	$3.11 \cdot 10^{15}$
Sum	$3.55 \cdot 10^{16}$	$1.66 \cdot 10^{17}$	$1.12 \cdot 10^{17}$	$1.80 \cdot 10^{17}$

Table 3.4: The number of systems for each of the choices of population synthesis model and each of the six metallicities, respectively. The bottom row shows the total number of systems for each of the population synthesis models. The SFRD used is the HZ19 model.

Z	$\alpha\alpha, \alpha = 1$	$\alpha\alpha, \alpha = 4$	$\gamma\alpha, \alpha = 1$	$\gamma\alpha, \alpha = 4$
0.0001	$7.65 \cdot 10^{15}$	$1.52 \cdot 10^{16}$	$1.44 \cdot 10^{16}$	$1.34 \cdot 10^{16}$
0.001	$8.81 \cdot 10^{15}$	$3.51 \cdot 10^{16}$	$2.77 \cdot 10^{16}$	$3.87 \cdot 10^{16}$
0.005	$6.35 \cdot 10^{15}$	$5.21 \cdot 10^{16}$	$2.73 \cdot 10^{16}$	$5.81 \cdot 10^{16}$
0.01	$6.96 \cdot 10^{15}$	$6.09 \cdot 10^{16}$	$3.61 \cdot 10^{16}$	$7.00 \cdot 10^{16}$
0.02	$5.41 \cdot 10^{15}$	$5.04 \cdot 10^{16}$	$2.96 \cdot 10^{16}$	$5.85 \cdot 10^{16}$
0.03	$3.75 \cdot 10^{15}$	$3.17 \cdot 10^{16}$	$1.87 \cdot 10^{16}$	$3.83 \cdot 10^{16}$
Sum	$3.89 \cdot 10^{16}$	$2.45 \cdot 10^{17}$	$1.54 \cdot 10^{17}$	$2.77 \cdot 10^{17}$

Table 3.5: The number of systems for each of the choices of population synthesis model and each of the six metallicities, respectively. The bottom row shows the total number of systems for each of the population synthesis models. The SFRD used is the LZ21 model.

Z	$\alpha\alpha, \alpha = 1$	$\alpha\alpha, \alpha = 4$	$\gamma\alpha, \alpha = 1$	$\gamma\alpha, \alpha = 4$
0.0001	$2.11 \cdot 10^{16}$	$4.57 \cdot 10^{16}$	$4.01 \cdot 10^{16}$	$3.95 \cdot 10^{16}$
0.001	$2.14 \cdot 10^{16}$	$8.65 \cdot 10^{16}$	$6.76 \cdot 10^{16}$	$9.57 \cdot 10^{16}$
0.005	$1.19 \cdot 10^{16}$	$9.73 \cdot 10^{16}$	$5.09 \cdot 10^{16}$	$1.08 \cdot 10^{17}$
0.01	$8.56 \cdot 10^{15}$	$7.43 \cdot 10^{16}$	$4.35 \cdot 10^{16}$	$8.32 \cdot 10^{16}$
0.02	$3.77 \cdot 10^{15}$	$3.50 \cdot 10^{16}$	$2.02 \cdot 10^{16}$	$3.90 \cdot 10^{16}$
0.03	$1.33 \cdot 10^{15}$	$1.11 \cdot 10^{16}$	$6.37 \cdot 10^{15}$	$1.27 \cdot 10^{16}$
Sum	$6.80 \cdot 10^{16}$	$3.50 \cdot 10^{17}$	$2.29 \cdot 10^{17}$	$3.78 \cdot 10^{17}$

Table 3.6: The number of systems for each of the choices of population synthesis model and each of the six metallicities, respectively. The bottom row shows the total number of systems for each of the population synthesis models. The SFRD used is the HZ21 model.

Z	$\alpha\alpha, \alpha = 1$	$\alpha\alpha, \alpha = 4$	$\gamma\alpha, \alpha = 1$	$\gamma\alpha, \alpha = 4$
0.0001	$1.04 \cdot 10^{16}$	$2.25 \cdot 10^{16}$	$1.98 \cdot 10^{16}$	$1.95 \cdot 10^{16}$
0.001	$1.31 \cdot 10^{16}$	$5.29 \cdot 10^{16}$	$4.15 \cdot 10^{16}$	$5.84 \cdot 10^{16}$
0.005	$9.69 \cdot 10^{15}$	$7.93 \cdot 10^{16}$	$4.16 \cdot 10^{16}$	$8.78 \cdot 10^{16}$
0.01	$1.17 \cdot 10^{16}$	$1.01 \cdot 10^{17}$	$5.92 \cdot 10^{16}$	$1.13 \cdot 10^{17}$
0.02	$1.09 \cdot 10^{16}$	$1.01 \cdot 10^{17}$	$5.83 \cdot 10^{16}$	$1.13 \cdot 10^{17}$
0.03	$9.48 \cdot 10^{15}$	$7.92 \cdot 10^{16}$	$4.55 \cdot 10^{16}$	$9.10 \cdot 10^{16}$
Sum	$6.54 \cdot 10^{16}$	$4.36 \cdot 10^{17}$	$2.66 \cdot 10^{17}$	$4.82 \cdot 10^{17}$

Similarly to before, here the effect of chirp mass will be comparable for each of the population synthesis models, since the (average) chirp masses barely differ from each other.

Furthermore, when investigating the contribution of BWD systems to the AGWB per redshift, it was again found that there are only negligible differences when comparing the different AGWBs. This is especially the case when looking at the SFRD models from 2019, for these models there are barely any differences in redshift contribution. Only $\alpha\alpha, \alpha = 1$ consists of slightly more systems at somewhat higher redshifts, but this can be seen in all 3 plots for the SFRD models from 2019. Similarly to before, most systems that

contribute reside at low redshifts. One thing to note is that when looking at the SFRD models from 2021, the contributions seem to come from slightly higher redshifts, than for the 2019 models (see Appendix A, Figure A.5 to Figure A.7 and Figure A.8 to Figure A.9, respectively). Again, these discrepancies between models are so small, that they can be ignored, since they will not have a significant effect on the AGWB signal strength.

Again, all AGWB signals in the figure shown in this section, lie significantly higher than the AGWB signals produced by BBHs and BNSs. So this work further cements the conclusion from the work by SN24 that the AGWB background that will be detected by LISA will be dominated by the merging of extra-galactic BWDs.

Comparing all four figures in this section (Figures 3.11 to 3.14), does not give extremely surprising results. In all four figures, the order of models is the same. This order comes from the amount of SFRD present in each of the models, as can be seen in Figure 2.1. Models with more SFRD (e.g. the models from the 2021 paper) lead to higher AGWB signals than models with less SFRD. It seems that the differences between all five models in all four figures are pretty similar. To investigate this further, the factors between the AGWB signals of all models were determined, as well as the factors between the total SFRDs (seen in Figure 2.1).

3.4.2 Comparison of the Differences Between the SFRDs and the AGWB Signals

To determine whether the differences between the five different metallicity dependent SFRD models come from the differences in total SFRD per model, the factors between the total SFRDs were determined, as well as the factors between the AGWB signals (Ω) over the whole frequency range (i.e. the average Ω). The results are shown in Table 3.7. All models are compared to the MZ19 model. This table shows that the factors between the total SFRDs are very close to the factors between the AGWB signals (Ω). The factors between the SFRDs and each of the AGWB signals, differ between roughly 2 and 7% of each other. So, it is relatively safe to say that the differences in factors between the AGWB signals as seen in Figures 3.11 to 3.14 arise from the difference in total SFRD for each of the models.

For both low metallicity extreme models (LZ19 and LZ21, respectively) the factors between the AGWB signals are slightly larger than the factors between the SFRD. However, interestingly, for the high metallicity extreme models (HZ19 and HZ21, respectively), the factors between the AGWB signals are slightly smaller than the factor between the SFRDs. So, in other words, a high metallicity extreme model (HZ19 and HZ21) means that relatively more Ω is produced compared to SFRD, when comparing both quantities to MZ19. Whereas, a low metallicity extreme model (LZ19 and LZ21) means that relatively more SFRD is produced compared to Ω , when again comparing both quantities to MZ19. However, it should be noted that the differences are obviously very small.

Table 3.7: The factors between all SFRDs and AGWB signals, respectively. Each of the models is compared to the MZ19 model. The first column describes the model with which the MZ19 model is compared. The second column shows the difference between the total SFRDs for each of these models. The third to sixth column show the factors between the AGWB signals, where each of the columns represents a different population synthesis model possibility.

AGWB Signal (Ω_{GW})					
Model	SFRD	$\alpha\alpha, \alpha = 1$	$\alpha\alpha, \alpha = 4$	$\gamma\alpha, \alpha = 1$	$\gamma\alpha, \alpha = 4$
HZ19	1.20	1.14	1.16	1.16	1.16
LZ19	0.69	0.74	0.71	0.73	0.71
HZ21	1.92	1.79	1.87	1.83	1.85
LZ21	1.36	1.39	1.40	1.39	1.39

3.5 Approximation of the Uncertainties

Using all previous results that used a metallicity dependent SFRD, an approximation on the uncertainties of the AGWB signal can be made. For every frequency of every AGWB signal, the upper and lower limit were determined. Then for each frequency the lowest lower limit and the highest upper limit were selected. Using these upper and lower limits a band can be created around the AGWB signal, representing the uncertainties. To show the uncertainties, the AGWB signal produced with the $\alpha\alpha$ mass transfer process, where α was set to a numerical value of four, was plotted again. Here the SFH of Madau & Dickinson (2014) was used and the metallicity of the universe was set to the solar metallicity ($Z = Z_{\odot} = 0.02$). This is the same signal as shown in Figure 3.1 (the red line). Moreover, the $\gamma\alpha, \alpha = 4$ AGWB signal produced with the MZ19 SFRD model was plotted as well. This was done since it is expected that this combination of choices (on the formation of BWDs as well as the SFRD) describes the universe more accurately than the choice where $\alpha\alpha$ with α equal to 4 was used. This AGWB signal and the band of uncertainties are shown in Figure 3.15.

Figure 3.15 shows that the AGWB signal using a metallicity independent SFH (red line), lies higher than the average of the uncertainties. In other words, this AGWB signal is on average higher than most of the AGWB signals shown in this thesis. This is somewhat expected since this signal comes from an $\alpha\alpha, \alpha = 4$ population synthesis model, which has been shown, throughout this work, to be (one of) the population synthesis model(s) that lead to the highest AGWB signal. The AGWB signal (green line) produced when using a metallicity dependent SFRD, in this case the MZ19 model, is significantly lower than the red line. The green line seems to be closer to the middle of the uncertainties, suggesting that this choice for population synthesis model and SFRD model lead to a rough average when compared to all results in this work. The band itself has an (average) size of 7.1×10^{-12} over the whole signal, and is clearly tighter at low frequencies and then gets slightly broader at higher frequencies. Once the AGWB signal decreases again, the band gets tighter again, to then broaden at the last part of the AGWB again. This broadening at the highest frequencies can be explained by the difference in shape of the AGWB signal at high frequencies, as mentioned in previous sections.

Only looking at some frequencies in LISA's frequency range, gives the following values for Ω as well as the width of the uncertainty band (or upper and lower limits) compared

Table 3.8: Ω_{GW} at different frequencies with the corresponding uncertainties. Frequencies are in Hz. Ω_{GW} and the corresponding errors are all multiplied by 10^{-12} .

$\log_{10}(f/\text{Hz})$	Ω_{GW}
-3.30	$2.39^{+3.39}_{-1.32}$
-2.85	$5.18^{+7.30}_{-2.62}$
-2.40	$10.6^{+15.0}_{-5.40}$
-1.95	$14.0^{+20.4}_{-5.78}$
-1.50	$6.58^{+11.2}_{-2.28}$

to the AGWB signal for $\gamma\alpha$, with α equal to 4 and the SFRD model, MZ19 (the green line). These results are shown in Table 3.8. The table shows that when the values for Ω increase, so do the upper limits of the uncertainty band. When Ω decreases again at higher frequencies, the numerical values for the upper limits decrease again. The lower limits of the uncertainty band also increase when Ω increases (and decrease when Ω decreases), however, it can be seen that the values with which the lower limits of the uncertainty band increase (or decrease) are significantly lower than those of the upper limits of the uncertainty band. Looking at the average of the upper limits of the uncertainty band of the five frequencies in LISA's frequency range, gives a rough average of $1.14 \cdot 10^{-11}$ (or in the format of the table: $11.4 \cdot 10^{-12}$). The average of the lower limits of the uncertainty band of the five frequencies in LISA's frequency range, is roughly equal to $3.48 \cdot 10^{-12}$. This shows that the band is slightly broader above the AGWB signal for $\gamma\alpha$, $\alpha = 4$ with the SFRD model, MZ19, than below this AGWB signal. This is also clear to see in Figure 3.15.

One thing to note is that while these uncertainties are meaningful to use in the case of this work, the uncertainties obviously do not encompass all possible uncertainties present in the future AGWB signal. So, while the uncertainties are more accurate than the uncertainties used in the previous work by SN24, where the uncertainties were an educated guess, they are not yet the full uncertainties that will come with this signal.

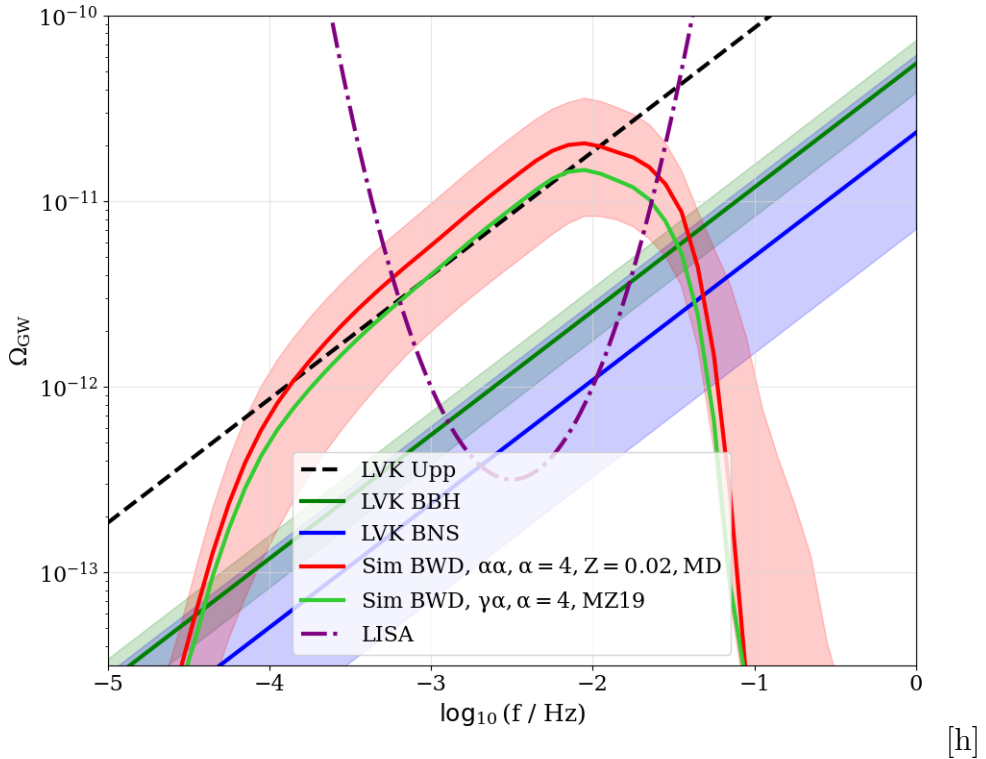


Figure 3.15: As in Figure 3.1, the red line represents the AGWB for the population synthesis model with two α mass transfer phases ($\alpha\alpha$), with a numerical value for α of 4 and the metallicity set to $Z = 0.02$ (Z_\odot). The SFH used here is that of Madau & Dickinson (2014). The green line represents the AGWB signal produced when using the population synthesis model $\gamma\alpha$ with α equal to 4. The SFRD used here is the MZ19 model. The band was created using the upper and lower limits of the results from this thesis and represents the uncertainties.

Chapter 4

Discussion

This chapter aims to discuss the validity of the results presented in this work. Firstly, some of the assumptions of this work are mentioned, as well as if these assumptions are accurate or not. Moreover, the used models (both population synthesis model and SFRD model) are touched upon and the effect of using different models not used in this work is discussed. Then, a comparison is made to the previous work by FP03, which was the first work which found that the AGWB signal by BWDs would be dominant. Afterwards, the results of this thesis in general are discussed, to be more precise, whether or not it will be possible to measure the GWB signal cut-off with LISA. Lastly, some possibilities for future research are suggested.

4.1 Validity of the Results in this Work

In most scientific works, one of the main questions is whether the results are valid and accurate when describing the way the universe works. In this work, several assumptions were made regarding the formation of WDs, since a lot is still unclear on this subject. However, the question is whether these assumptions are correct and if, subsequently, the results are then correct as well. Unfortunately, until now, there is no way to confirm the results of this work, yet. Nevertheless, in the future the results of this work can possibly be confirmed, once the LISA detector is launched (LISA is currently scheduled for a 2035 launch (ESA, 2024a)). LISA will detect an AGWB signal, and from this signal, it will be possible to investigate the validity of this work and see if the results in this work are correct. It might even be possible to get a more definite answer on the still unknown formation of BWDs. Aside from LISA, there might be other future observations/detections or theories that can be used to validate the results in this thesis.

4.1.1 Assumptions in this Work

Some of the assumptions made in this work are regarding the formation of BWDs. For starters, the choice is made to use the α and γ formalism in 4 slightly different ways, as mentioned before, the four possible population synthesis models:

- $\alpha\alpha$ where α is equal to 1
- $\alpha\alpha$ where α is equal to 4
- $\gamma\alpha$ where α is equal to 1
- $\gamma\alpha$ where α is equal to 4

The choice of the numerical values for both α and γ come from previous work (see e.g. Nelemans et al. (2000)), however, other possibilities are possible as well, since there is no direct proof that these numerical values indeed describe the formation of BWDs correctly. For example, as mentioned before, formally, α can have a numerical value between 0 and 1. The usage of a numerical value of less than 1 for α might lead to interesting results. Furthermore, the question is whether the formation of BWDs indeed occurs through unstable and unconservative mass transfer. Picco et al. (2024) state that stable mass transfer could be a possibility as well. Moreover, it is unclear whether the relatively simple formalisms α and γ correctly describe the formation of BWDs, or whether there are more factors that complicate this process. Furtermore, there might even be a completely different process that is happening when the formation of BWDs is occurring that is simply not understood as of yet.

4.1.2 Choice of Models

The population synthesis code that is used in this work is SEBA, as mentioned before. It should be noted that there are several other population synthesis codes that also produce BWDs like SEBA, for example BPASS (J. Eldridge et al. (2017); Stanway & Eldridge (2018); J. J. Eldridge & Stanway (2022)) or BSE (Hurley et al. (2002)). Using other population synthesis codes might lead to a significant change in AGWB signal, something which is important to take into account. The difference between the population synthesis codes is that SEBA and BSE are so-called rapid population synthesis codes, in the sense that they are efficient. Most rapid population synthesis codes use analytic fits that are used on models of single stars. BPASS, for example, is not a rapid population synthesis code and models stellar and binary evolution in much more detail. This leads to differences in the output, e.g. the number of systems of BWDs, specifically (see e.g. Tang et al. (2024)). This can lead to a significant difference in AGWB signal, as shown in this work, where models with an order of 10 lower number of systems, leads to clearly weaker AGWB signals.

Aside from the population synthesis code that is used in this work, another model that might affect the results is the model used for the metallicity dependent SFRD. The idea that the SFRD is dependent on both redshift and metallicity is not new, there are several different models that take into account the metallicity dependency of the SFRD. Some examples of different SFRD models are e.g. Neijssel et al. (2019); Santoliquido et

al. (2021); Broekgaarden et al. (2021); Briel et al. (2022). Obviously, using a different SFRD model will lead to a different AGWB. This is clear since even using different types of models by Chruścińska & Nelemans (2019); Chruścińska et al. (2021) leads to a significant change in the AGWB. Therefore, it might be an interesting thing to investigate.

4.1.3 Comparison with Previous Work

In this work, a comparison with previous work by SN24 is done extensively. However, both this work and the work by SN24 are based on earlier work by FP03. FP03 is the first work that suggests that the signal from BWDs will be dominant in the AGWB. Their methods are very similar to the methods used in this work, with the exception of the choice on whether to discretize the integral over redshift or cosmic time. This work, as shown in Chapter 2, discretizes the integral over redshift, while the FP03 discretizes the integral over cosmic time. SN24 showed that this difference does not have an effect on the results (i.e. both methods give the same results), meaning that it is possible to make a comparison between the results in this work and the results in FP03.

FP03 find for the AGWB signal produced by BWDs the following results at a frequency of 1 mHz¹:

$$\Omega_{\text{WD}}(1\text{mHz}) = 3.57 \cdot 10^{-12}$$

Using the population synthesis model $\alpha\alpha$, $\alpha = 4$, and a metallicity of 0.02 (Z_\odot), as well as the SFH by Madau & Dickinson (2014), as in Figure 3.15, the AGWB signal at 1 mHz is as follows:

$$\Omega_{\text{WD}}(1\text{mHz}) = 5.75 \cdot 10^{-12}$$

Using the other AGWB signal in Figure 3.15, for the population synthesis model with $\gamma\alpha$, $\alpha = 4$ and using the MZ19 (metallicity dependent) SFRD model instead of Madau & Dickinson (2014), gives the following AGWB signal at 1 mHz:

$$\Omega_{\text{WD}}(1\text{mHz}) = 4.01 \cdot 10^{-12}$$

Ω at 1 mHz for the population synthesis model where two α mass transfer phases were used as well as a metallicity of 0.02 and a metallicity independent SFH, is about 1.6 times larger than the Ω that was found in FP03. This difference most likely comes from the different SFH that was used. The Ω at 1 mHz that was found using the population synthesis model where $\gamma\alpha$ with $\alpha = 4$ was used, as well as the metallicity dependent SFRD model (MZ19, to be precise) was used, differs less compared to FP03. It only differs about a factor of 1.1 compared to FP03. It should be noted however, that FP03 only looked at one (constant) metallicity of the universe, while the MZ19 does not. This makes comparing the two somewhat harder, since there are a lot more factors that differ between both results, meaning there are a lot of different factors (e.g. usage of γ instead of α , using a metallicity dependent SFRD) that affect the AGWB signal at a frequency

¹This is the AGWB signal (Ω_{WD}) at 1 mHz FP03 find for their model A. A brief discussion on the parameters used in this model, as well as a comparison to the models used in this work can be found at the end of this section.

Table 4.1: Average AGWB signal (Ω_{WD}) at 1 mHz for each of the five SFRD models. The SFRD models are retrieved from Chruścińska & Nelemans (2019); Chruścińska et al. (2021). Column 1 represents the choice of SFRD model. Column 2 to 5 show the $\Omega_{WD}(1\text{mHz})$ of the sum of all metallicities for each population synthesis model. Column 6 shows the average of column 2 to 5.

SFRD	$\Omega_{WD}(1\text{mHz})$				
	$\alpha\alpha, \alpha = 1$	$\alpha\alpha, \alpha = 4$	$\gamma\alpha, \alpha = 1$	$\gamma\alpha, \alpha = 4$	Average
MZ19	$2.54 \cdot 10^{-12}$	$5.11 \cdot 10^{-12}$	$5.04 \cdot 10^{-12}$	$4.01 \cdot 10^{-12}$	$4.17 \cdot 10^{-12}$
HZ19	$2.82 \cdot 10^{-12}$	$5.99 \cdot 10^{-12}$	$5.75 \cdot 10^{-12}$	$4.65 \cdot 10^{-12}$	$4.80 \cdot 10^{-12}$
LZ19	$1.97 \cdot 10^{-12}$	$3.55 \cdot 10^{-12}$	$3.71 \cdot 10^{-12}$	$2.84 \cdot 10^{-12}$	$3.02 \cdot 10^{-12}$
HZ21	$4.43 \cdot 10^{-12}$	$9.63 \cdot 10^{-12}$	$9.14 \cdot 10^{-12}$	$7.49 \cdot 10^{-12}$	$7.67 \cdot 10^{-12}$
LZ21	$3.71 \cdot 10^{-12}$	$7.03 \cdot 10^{-12}$	$7.17 \cdot 10^{-12}$	$5.61 \cdot 10^{-12}$	$5.88 \cdot 10^{-12}$

of 1 mHz. Looking at the average AGWB signal for each of the different SFRD models in this work, gives the results as seen in Table 4.1.

In Table 4.1 columns 2 to 5 each represent one of the population synthesis models used. For each of the models, the average Ω at 1 mHz for all 6 different metallicities is computed. Each row corresponds to one of the 5 possibilities for the SFRD, each row representing one of the metallicity dependent SFRDs. The table clearly shows one of the conclusions from the previous chapter, namely that choosing the population synthesis model $\alpha\alpha$, with $\alpha = 4$ or the population synthesis model $\gamma\alpha$, with $\alpha = 1$, lead to the highest AGWB signal. On average the Ω 's in Table 4.1 are approximately a factor of 1.4 larger than the Ω found in FP03. With outliers to both higher and lower numbers than the factor of 1.4, for LZ19 and HZ21 specifically, as seen in the table.

In general the reason for the difference is the difference in choice for the SFH (or SFRD) model. While in this work, Madau & Dickinson (2014) is used for the non-metallicity dependent case and Chruścińska & Nelemans (2019); Chruścińska et al. (2021) are used for the metallicity dependent case, FP03 use a method as described in Cole et al. (2001) and Schneider et al. (2001). The choice in formation model might also have an effect. FP03 use $\alpha = 3$ for the efficiency for the common envelope phase², while this work uses α equal to either 1 or 4. Furthermore, the model in FP03 leading to the aforementioned Ω uses a solar metallicity ($Z = 0.02 = Z_\odot$), while this work uses 6 different metallicities. Lastly, FP03 use the BSE code to create the population synthesis models that are used in their work, while this work uses SEBA. As mentioned in a previous section, a different choice in stellar and binary evolution code leads to considerable differences in the population, and thus in the AGWB signal emitted by this population.

²This is the numerical value which is used for their Model A. This is also the model which gives an $\Omega_{WD}(1\text{mHz})$ of $3.57 \cdot 10^{-12}$. Some of the other models that are used are altered in e.g. the numerical values for α .

4.2 Measuring the AGWB Cut-Off

While the AGWB signal in itself is extremely interesting, one of the most interesting aspects is the question whether or not it will be possible for LISA to detect the cut-off. As can be seen in all figures (Figure 3.1 to Figure 3.15) the AGWB signal rises, until it peaks, after which it decreases again. The region of interest, this cut-off, is the moment when the AGWB signal peaks and starts to decrease. It seems that in most of the figures, the peak and the start of the decline are clearly within LISA's range, except for Figure 3.2. In this case, only the lowest metallicities lead to the possibility of detecting the cut-off, while for the higher metallicities ($Z = 0.005$ to $Z = 0.03$) this cut-off will be outside LISA's range. However, in general, it seems to be possible to detect this cut-off in most cases of mass transfer, metallicity and SFRD model.

4.3 Further Research

As mentioned before in Section 4.1.2, the choice of code to produce the population synthesis models has an effect on the population and therefore the AGWB signal. Further research could consist of investigating exactly how large the effect is of this choice. The same goes for the use of the specific metallicity dependent SFRD model used in this thesis, investigating the effect of choosing this specific model instead of another might be of interest. Moreover, for the two different formalisms, three numerical values were used in this entire work (α either equal to 1 or 4 and γ equal to 1.75). It could be interesting to see what the effect is of choosing a different numerical value for γ , as well as looking at the effect of using a value smaller than 1 for α , since this is (formally) the only possibility for α . However, it should be noted that currently $\gamma = 1.75$ and $\alpha = 4$ are generally most accepted as the correct way to describe the formation of BWDs (see e.g. Nelemans et al. (2000); Toonen et al. (2012)). Furthermore, since the two formalisms used in this work both define the two mass transfer phases as unstable, it might be interesting to investigate what AGWB is produced when forming the BWDs with stable mass transfer. Since stable mass transfer has recently been introduced as being able to describe the observations of BWD systems (see Picco et al. (2024)).

Finally, if future theories and/or observations lead to new ideas on the theory behind the formation of BWDs, it is meaningful to implement these theories in a population synthesis code (e.g. SEBA) and explore the effects this new theory might have on the AGWB signal emitted by BWDs.

Chapter 5

Conclusion

The aim of this work was to answer the research question: What are the effects of a different choice of mass transfer process and metallicity on the AGWB produced by extra-galactic WDs that will be detected by LISA? Looking at the AGWB signals produced with the metallicity independent SFH (Madau & Dickinson, 2014), only the small metallicities seem to have a significant effect on the strength of the AGWB signal. Most other metallicities are indistinguishable from each other, suggesting that the effect of metallicity in this case is extremely small. This claim is further supported, when knowing that our universe will not primarily consist of small metallicities, meaning that these metallicities are most likely not contributing significantly to the actual AGWB. A better way to investigate the effect of metallicity, is to look at the metallicity dependent SFRD. Here again, two extreme metallicities (in this case $Z = 0.0001$ and $Z = 0.03$) clearly lead to the weakest AGWB signal. However, this is because these metallicities have a smaller amount of SFRD. A smaller amount of SFRD leads to less sources (since there is less star formation), giving a sound explanation for the relative weakness of these AGWB signals. Lastly, different metallicity dependent SFRD models were used and the result of this usage is again the fact that models which contain more SFRD lead to a higher AGWB signal. So, to summarise, metallicity clearly does have an effect, but it is relatively small and the choice of SFRD model has a much larger effect, as expected.

The second part of the research question was regarding the choice of mass transfer process (or population synthesis model) and the effect this choice has on the AGWB signal. The most notable effect is that the choice of $\alpha\alpha$, $\alpha = 1$, clearly leads to the lowest AGWB signal. This is expected, since this choice in population synthesis model can lead to the merger of binary systems before these systems are able to become BWDs. The other three choices give negligible differences, with $\gamma\alpha$, $\alpha = 4$ leading to a slightly lower AGWB signal compared to the other two possibilities, however, again, these differences are trivial.

Previous research (see e.g. Nelemans et al. (2000); Toonen et al. (2012)) find that a choice of $\gamma\alpha$ with α equal to 4, best describe a sample of BWDs in our neighbourhood. Therefore, this work uses this choice as the main result. The AGWB signal produced with this choice of population synthesis for a metallicity dependent SFRD (in this case MZ19) is clearly dominant over the merging BBHs and BNSs that LISA might detect. Moreover, this work shows that (at least the beginning of) the cut-off should be in LISA's range, and therefore be detectable in the future.

Chapter 6

References

- Abbott, B., Abbott, R., Abbott, T., Abernathy, M., Acernese, F., Ackley, K., ... Zweizig, J. (2016, February). Observation of gravitational waves from a binary black hole merger. *Physical Review Letters*, 116(6). Retrieved from <http://dx.doi.org/10.1103/PhysRevLett.116.061102> doi: 10.1103/physrevlett.116.061102
- Abbott, B., Abbott, R., Abbott, T., Acernese, F., Ackley, K., Adams, C., ... Zweizig, J. (2017, October). Gw170817: Observation of gravitational waves from a binary neutron star inspiral. *Physical Review Letters*, 119(16). Retrieved from <http://dx.doi.org/10.1103/PhysRevLett.119.161101> doi: 10.1103/physrevlett.119.161101
- Abbott, B., Abbott, R., Adhikari, R., Ageev, A., Allen, B., Amin, R., ... others (2004). Detector description and performance for the first coincidence observations between ligo and geo. *Nuclear Instruments and Methods in Physics Research Section A: Accelerators, Spectrometers, Detectors and Associated Equipment*, 517(1-3), 154–179.
- Abbott, R., Abbott, T., Abraham, S., Acernese, F., Ackley, K., Adams, A., ... others (2021b). Upper limits on the isotropic gravitational-wave background from advanced ligo and advanced virgo's third observing run. *Physical Review D*, 104(2), 022004.
- Abbott, R., Abbott, T. D., Abraham, S., Acernese, F., Ackley, K., Adams, A., ... others (2021a). Observation of gravitational waves from two neutron star–black hole coalescences. *The Astrophysical journal letters*, 915(1), L5.
- Abe, H., Akutsu, T., Ando, M., Araya, A., Aritomi, N., Asada, H., ... others (2022). The current status and future prospects of kagra, the large-scale cryogenic gravitational wave telescope built in the kamioka underground. *Galaxies*, 10(3), 63.
- Accadia, T., Acernese, F., Alshourbagy, M., Amico, P., Antonucci, F., Aoudia, S., ... others (2012). Virgo: a laser interferometer to detect gravitational waves. *Journal of instrumentation*, 7(03), P03012.
- Acernese, F., Adams, T., Agatsuma, K., Aiello, L., Allocca, A., Amato, A., ... others (2018). Status of advanced virgo. In *Epj web of conferences* (Vol. 182, p. 02003).
- Althaus, L. G., Córscico, A. H., Isern, J., & García-Berro, E. (2010). Evolutionary and pulsational properties of white dwarf stars. *The Astronomy and Astrophysics Review*, 18, 471–566.

- Amaro-Seoane, P., Audley, H., Babak, S., Baker, J., Barausse, E., Bender, P., ... Zweifel, P. (2017, February). Laser Interferometer Space Antenna. *arXiv e-prints*, arXiv:1702.00786. doi: 10.48550/arXiv.1702.00786
- Amaro-Seoane, P., Andrews, J., Arca Sedda, M., Askar, A., Baghi, Q., Balasov, R., ... others (2023). Astrophysics with the laser interferometer space antenna. *Living Reviews in Relativity*, 26(1), 2.
- Anders, E., & Grevesse, N. (1989). Abundances of the elements: Meteoritic and solar. *Geochimica et Cosmochimica acta*, 53(1), 197–214.
- Aso, Y., Michimura, Y., Somiya, K., Ando, M., Miyakawa, O., Sekiguchi, T., ... others (2013). Interferometer design of the kagra gravitational wave detector. *Physical Review D*, 88(4), 043007.
- Briel, M. M., Eldridge, J. J., Stanway, E. R., Stevance, H. F., & Chrimes, A. A. (2022, 04). Estimating transient rates from cosmological simulations and BPASS. *Monthly Notices of the Royal Astronomical Society*, 514(1), 1315–1334. Retrieved from <https://doi.org/10.1093/mnras/stac1100> doi: 10.1093/mnras/stac1100
- Broekgaarden, F. S., Berger, E., Neijssel, C. J., Vigna-Gómez, A., Chattopadhyay, D., Stevenson, S., ... Mandel, I. (2021). Impact of massive binary star and cosmic evolution on gravitational wave observations i: black hole–neutron star mergers. *Monthly Notices of the Royal Astronomical Society*, 508(4), 5028–5063.
- Carroll, B. W., & Ostlie, D. A. (2014). *An introduction to modern astronomy*. Pearson Education Limited.
- Chandrasekhar, S. (1931). The maximum mass of ideal white dwarfs. *Astrophysical Journal*, vol. 74, p. 81, 74, 81.
- Chruścińska, M., & Nelemans, G. (2019). Metallicity of stars formed throughout the cosmic history based on the observational properties of star-forming galaxies. *Monthly Notices of the Royal Astronomical Society*, 488(4), 5300–5326.
- Chruścińska, M., Nelemans, G., Boco, L., & Lapi, A. (2021). The impact of the fmr and starburst galaxies on the (low metallicity) cosmic star formation history. *Monthly Notices of the Royal Astronomical Society*, 508(4), 4994–5027.
- Cole, S., Norberg, P., Baugh, C. M., Frenk, C. S., Bland-Hawthorn, J., Bridges, T., ... others (2001). The 2df galaxy redshift survey: near-infrared galaxy luminosity functions. *Monthly Notices of the Royal Astronomical Society*, 326(1), 255–273.
- Eggleton, P. P. (1983). Approximations to the radii of roche lobes. *Astrophysical Journal, Part 1 (ISSN 0004-637X)*, vol. 268, May 1, 1983, p. 368, 369., 268, 368.
- Eldridge, J., Stanway, E. R., Xiao, L., McClelland, L., Taylor, G., Ng, M., ... Bray, J. (2017). Binary population and spectral synthesis version 2.1: construction, observational verification, and new results. *Publications of the Astronomical Society of Australia*, 34, e058.

- Eldridge, J. J., & Stanway, E. R. (2022). New insights into the evolution of massive stars and their effects on our understanding of early galaxies. *Annual Review of Astronomy and Astrophysics*, 60, 455–494.
- ESA. (2024a, January). *Capturing the ripples of spacetime: Lisa gets go-ahead*. (https://www.esa.int/Science_Exploration/Space_Science/Capturing_the_ripples_of_spacetime_LISA_gets_go-ahead [Accessed: 05/02/2024])
- ESA. (2024b, February). *How many stars are there in the universe?* (https://www.esa.int/Science_Exploration/Space_Science/Herschel/How_many_stars_are_there_in_the_Universe [Accessed: 20/02/2024])
- Farmer, A. J., & Phinney, E. S. (2003). The gravitational wave background from cosmological compact binaries. *Monthly Notices of the Royal Astronomical Society*, 346(4), 1197–1214.
- Figer, D. F. (2005). An upper limit to the masses of stars. *Nature*, 434(7030), 192–194.
- Gentile Fusillo, N., Tremblay, P.-E., Cukanovaite, E., Vorontseva, A., Lallement, R., Hollands, M., ... Jordan, S. (2021). A catalogue of white dwarfs in gaia edr3. *Monthly Notices of the Royal Astronomical Society*, 508(3), 3877–3896.
- Hartle, J. B. (2003). *Gravity: an introduction to einstein's general relativity*. Addison Wesley.
- Hirschi, R., Chiappini, C., Meynet, G., Maeder, A., & Ekström, S. (2007). Stellar evolution at low metallicity. *Proceedings of the International Astronomical Union*, 3(S250), 217–230.
- Hogg, D. W. (1999). Distance measures in cosmology. *arXiv preprint astro-ph/9905116*.
- Hurley, J. R., Tout, C. A., & Pols, O. R. (2002). Evolution of binary stars and the effect of tides on binary populations. *Monthly Notices of the Royal Astronomical Society*, 329(4), 897–928.
- Iben, I., & Livio, M. (1993). Common envelopes in binary star evolution. *Publications of the Astronomical Society of the Pacific*, 105(694), 1373.
- Jennrich, O. (2009). Lisa technology and instrumentation. *Classical and Quantum Gravity*, 26(15), 153001.
- Kilic, M., Prieto, C. A., Brown, W. R., & Koester, D. (2007). The lowest mass white dwarf. *The Astrophysical Journal*, 660(2), 1451.
- Klein, A., Barausse, E., Sesana, A., Petiteau, A., Berti, E., Babak, S., ... Wardell, B. (2016, January). Science with the space-based interferometer elISA: Supermassive black hole binaries. *Phys. Rev. D*, 93(2), 024003. doi: 10.1103/PhysRevD.93.024003
- Koester, D. (2002). White dwarfs: Recent developments. *The Astronomy and Astrophysics Review*, 11, 33–66.

- Korol, V., Rossi, E. M., Groot, P. J., Nelemans, G., Toonen, S., & Brown, A. G. A. (2017, 05). Prospects for detection of detached double white dwarf binaries with Gaia, LSST and LISA. *Monthly Notices of the Royal Astronomical Society*, 470(2), 1894–1910. Retrieved from <https://doi.org/10.1093/mnras/stx1285> doi: 10.1093/mnras/stx1285
- Lehoucq, L., Dvorkin, I., Srinivasan, R., Pellouin, C., & Lamberts, A. (2023, 09). Astrophysical uncertainties in the gravitational-wave background from stellar-mass compact binary mergers. *Monthly Notices of the Royal Astronomical Society*, 526(3), 4378–4387. Retrieved from <https://doi.org/10.1093/mnras/stad2917> doi: 10.1093/mnras/stad2917
- Livio, M., & Soker, N. (1988). The common envelope phase in the evolution of binary stars. *Astrophysical Journal, Part 1 (ISSN 0004-637X)*, vol. 329, June 15, 1988, p. 764–779., 329, 764–779.
- Madau, P., & Dickinson, M. (2014). Cosmic star-formation history. *Annual Review of Astronomy and Astrophysics*, 52, 415–486.
- Maoz, D., & Hallakoun, N. (2017). The binary fraction, separation distribution and merger rate of white dwarfs from spy. *Monthly Notices of the Royal Astronomical Society*, 467(2), 1414–1425.
- Maoz, D., Hallakoun, N., & Badenes, C. (2018). The separation distribution and merger rate of double white dwarfs: improved constraints. *Monthly Notices of the Royal Astronomical Society*, 476(2), 2584–2590.
- Martynov, D. V., Hall, E., Abbott, B., Abbott, R., Abbott, T., Adams, C., ... others (2016). Sensitivity of the advanced ligo detectors at the beginning of gravitational wave astronomy. *Physical Review D*, 93(11), 112004.
- Neijssel, C. J., Vigna-Gómez, A., Stevenson, S., Barrett, J. W., Gaebel, S. M., Broekgaarden, F. S., ... Mandel, I. (2019). The effect of the metallicity-specific star formation history on double compact object mergers. *Monthly Notices of the Royal Astronomical Society*, 490(3), 3740–3759.
- Nelemans, G., Verbunt, F., Yungelson, L. R., & Zwart, S. F. P. (2000). Reconstructing the evolution of double helium white dwarfs: envelope loss without spiral-in. *arXiv preprint astro-ph/0006216*.
- Nelemans, G., Yungelson, L. R., Zwart, S. P., & Verbunt, F. (2001). Population synthesis for double white dwarfs-i. close detached systems. *Astronomy & Astrophysics*, 365(3), 491–507.
- Pagel, B. E. J. (2009). *Nucleosynthesis and chemical evolution of galaxies*. Cambridge University Press.
- Peacock, J. (1999). *Cosmological physics*. Cambridge University Press.
- Peters, P. C., & Mathews, J. (1963, July). Gravitational Radiation from Point Masses in a Keplerian Orbit. *Physical Review*, 131(1), 435–440. doi: 10.1103/PhysRev.131.435

- Picco, A., Marchant, P., Sana, H., & Nelemans, G. (2024). Forming merging double compact objects with stable mass transfer. *Astronomy & Astrophysics*, 681, A31.
- Pitkin, M., Reid, S., Rowan, S., & Hough, J. (2011). Gravitational wave detection by interferometry (ground and space). *Living Reviews in Relativity*, 14, 1–75.
- Portegies Zwart, S., & Verbunt, F. (1996). Population synthesis of high-mass binaries. *Astronomy and Astrophysics*, 309, 179–196.
- Riles, K. (2013). Gravitational waves: Sources, detectors and searches. *Progress in Particle and Nuclear Physics*, 68, 1–54.
- Santoliquido, F., Mapelli, M., Giacobbo, N., Bouffanais, Y., & Artale, M. C. (2021, 02). The cosmic merger rate density of compact objects: impact of star formation, metallicity, initial mass function, and binary evolution. *Monthly Notices of the Royal Astronomical Society*, 502(4), 4877–4889. Retrieved from <https://doi.org/10.1093/mnras/stab280> doi: 10.1093/mnras/stab280
- Saumon, D., Blouin, S., & Tremblay, P. (2022). Current challenges in the physics of white dwarf stars. *Physics Reports*, 988, 1–63.
- Schneider, R., Ferrari, V., Matarrese, S., & Portegies Zwart, S. F. (2001). Low-frequency gravitational waves from cosmological compact binaries. *Monthly Notices of the Royal Astronomical Society*, 324(4), 797–810.
- Sousa, M., Coelho, J., de Araujo, J., Guidorzi, C., & Rueda, J. (2023). On the optical transients from double white-dwarf mergers. *The Astrophysical Journal*, 958(2), 134.
- Staelens, S., & Nelemans, G. (2024). The astrophysical gravitational wave background in the mhz band is likely dominated by white dwarf binaries. *arXiv preprint arXiv:2310.19448*.
- Stanway, E. R., & Eldridge, J. (2018). Re-evaluating old stellar populations. *Monthly Notices of the Royal Astronomical Society*, 479(1), 75–93.
- Taam, R. E., & Ricker, P. M. (2010). Common envelope evolution. *New Astronomy Reviews*, 54(3-6), 65–71.
- Takahashi, K., Yoshida, T., & Umeda, H. (2013). Evolution of progenitors for electron capture supernovae. *The Astrophysical Journal*, 771(1), 28.
- Tang, P., Eldridge, J., Meyer, R., Lamberts, A., Boileau, G., & van Zeist, W. (2024). Predicting gravitational wave signals from bpss white dwarf binary and black hole binary populations of a milky way-like galaxy model for lisa. *arXiv preprint arXiv:2405.20484*.
- Toonen, S., Nelemans, G., & Zwart, S. P. (2012). Supernova type ia progenitors from merging double white dwarfs-using a new population synthesis model. *Astronomy & Astrophysics*, 546, A70.
- Verbunt, F., & Rappaport, S. (1988). Mass transfer instabilities due to angular momentum flows in close binaries. *The Astrophysical Journal*, 332, 193–198.

Webbink, R. F. (1984, February). Double white dwarfs as progenitors of R Coronae Borealis stars and type I supernovae. *ApJ*, *277*, 355-360. doi: 10.1086/161701

Weber, J. (1960). Detection and generation of gravitational waves. *Physical Review*, *117*(1), 306.

Woods, T. E., Ivanova, N., van der Sluys, M. V., & Chaichenets, S. (2011). On the formation of double white dwarfs through stable mass transfer and a common envelope. *The Astrophysical Journal*, *744*(1), 12.

Appendix A

Redshift Contribution Figures

The following figures show the redshift contributions and number of systems per frequency bin for all four different population synthesis models and all six different metallicities.

A.1 Effect of Different Population Synthesis Models and Metallicities on the AGWB

The following figures show the contributions of each redshift bin to the total AGWB for the four population synthesis models and for the six metallicities, respectively. Figure A.1 shows the redshift contribution plots for $\alpha\alpha$, with $\alpha = 1$. Figure A.2 shows the redshift contribution plots for $\alpha\alpha$, with $\alpha = 4$. Figure A.3 shows the redshift contribution plots for $\gamma\alpha$, with $\alpha = 1$. Lastly, Figure A.4 shows the redshift contribution plots for $\gamma\alpha$, with $\alpha = 4$. As can be seen in all four figures, there are no significant differences between the population synthesis models. The most distinct differences come from the different metallicities.

A.2 Comparing Different Types of Metallicity Dependent SFRDs

The figures in this section show the redshift contributions for each population synthesis model for each of the five different metallicity dependent SFRD models, respectively. Figure A.5 shows the redshift contribution plots for the LZ19 model. Figure A.6 shows the redshift contribution plots for the MZ19 model. Figure A.7 shows the redshift contribution plots for the HZ19 model. Lastly, Figure A.8 and Figure A.9 show the redshift contributions plots for the LZ21 and HZ21 model, respectively. The differences between the first three figures are negligible. However, comparing the first three figures to the last two figures does show some differences, namely the LZ21 and HZ21 models having contributions from slightly higher redshifts at lower frequencies. However, the differences are very marginal. The differences between these last two figures are again extremely small.

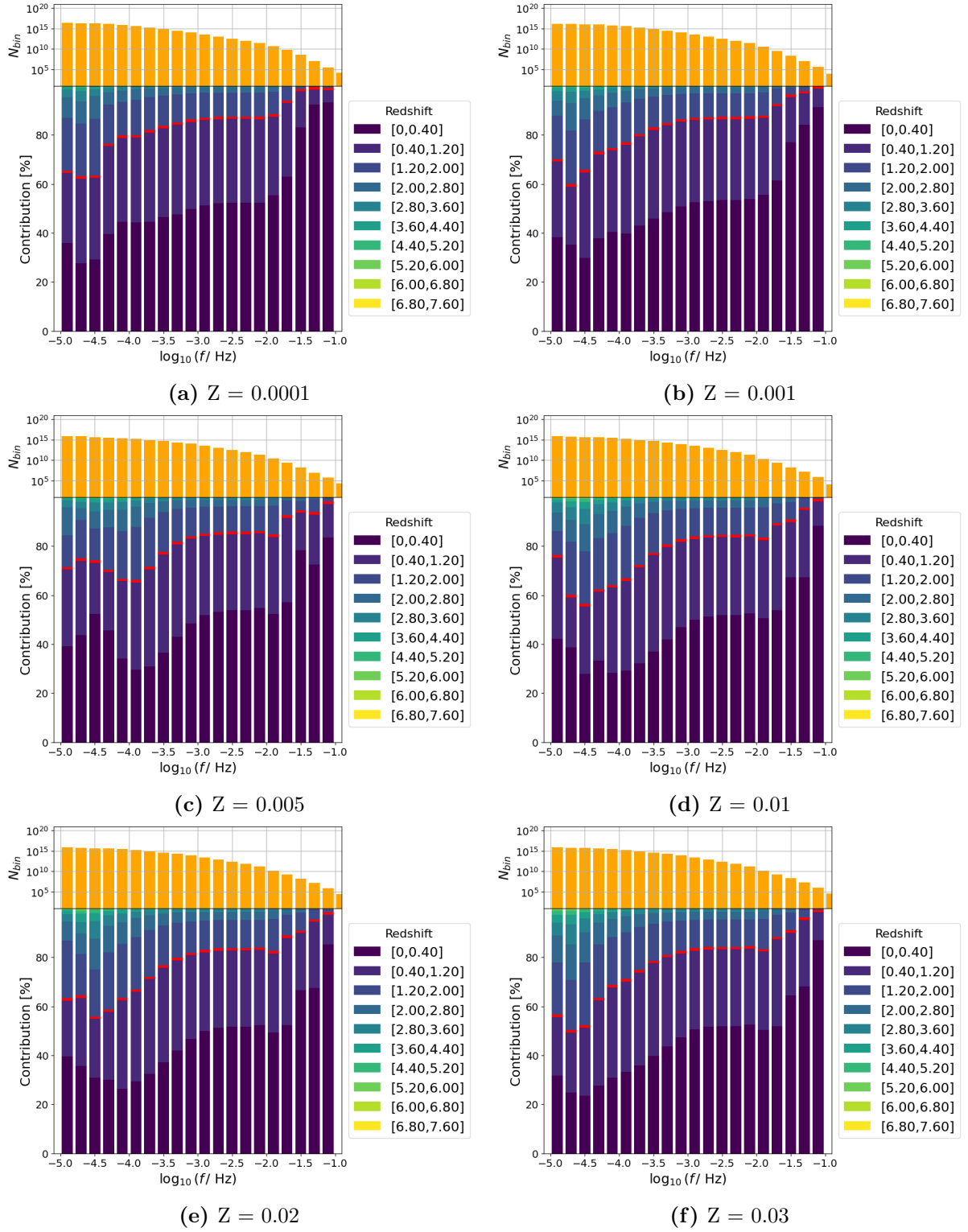


Figure A.1: The bottom panel shows the contribution (in percentage) of each redshift bin to the AGWB signal. The red line represents a redshift of 0.46. The AGWB signal's contribution are binned in 20 frequency bins. The top panel shows the number of systems present in each of the frequency bins, respectively. The population synthesis model plotted here is $\alpha\alpha$ with $\alpha = 1$. The SFH by Madau & Dickinson (2014) was used.

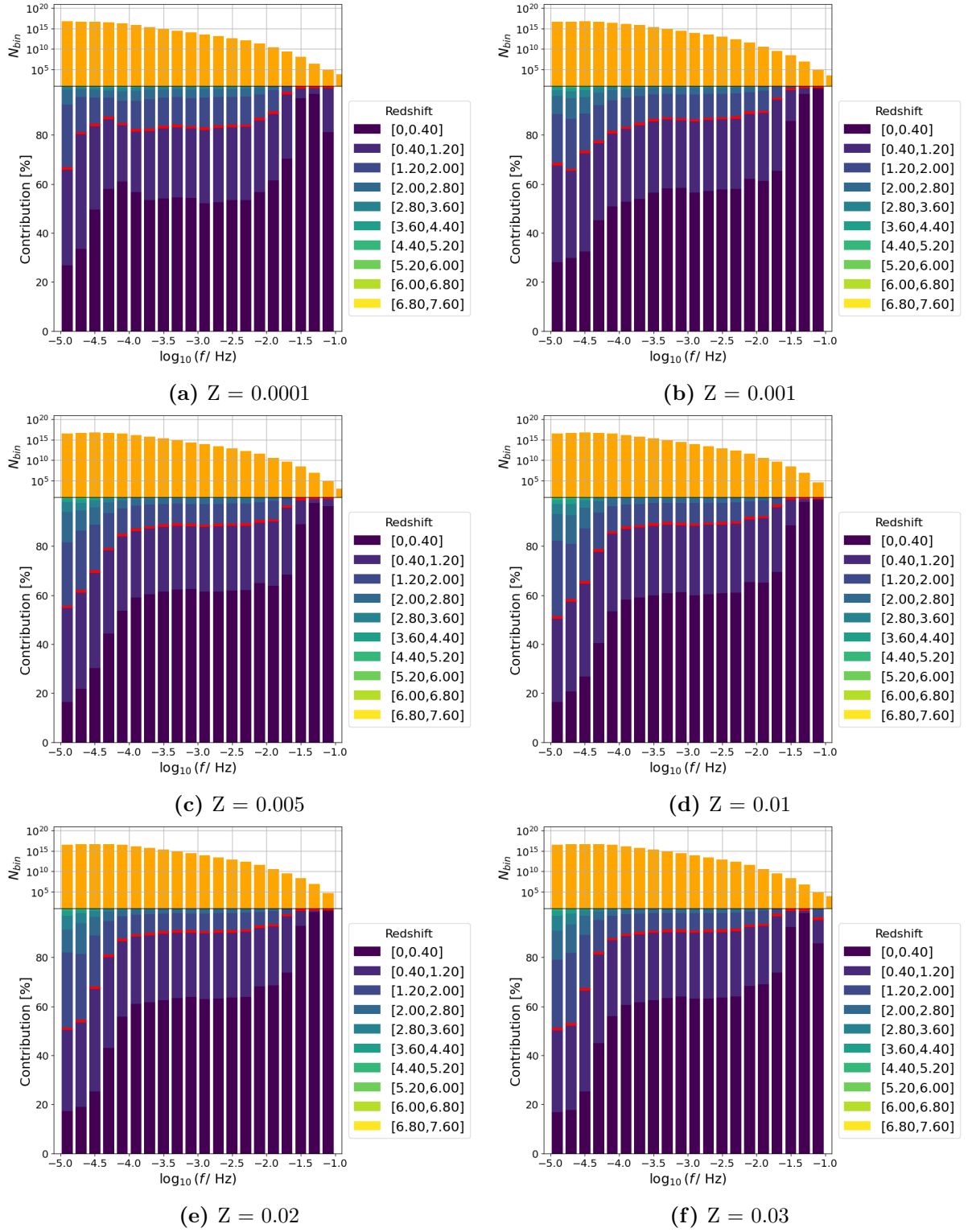


Figure A.2: The bottom panel shows the contribution (in percentage) of each redshift bin to the AGWB signal. The red line represents a redshift of 0.46. The AGWB signal's contribution are binned in 20 frequency bins. The top panel shows the number of systems present in each of the frequency bins, respectively. The population synthesis model plotted here is $\alpha\alpha$ with $\alpha = 4$. The SFH by Madau & Dickinson (2014) was used.

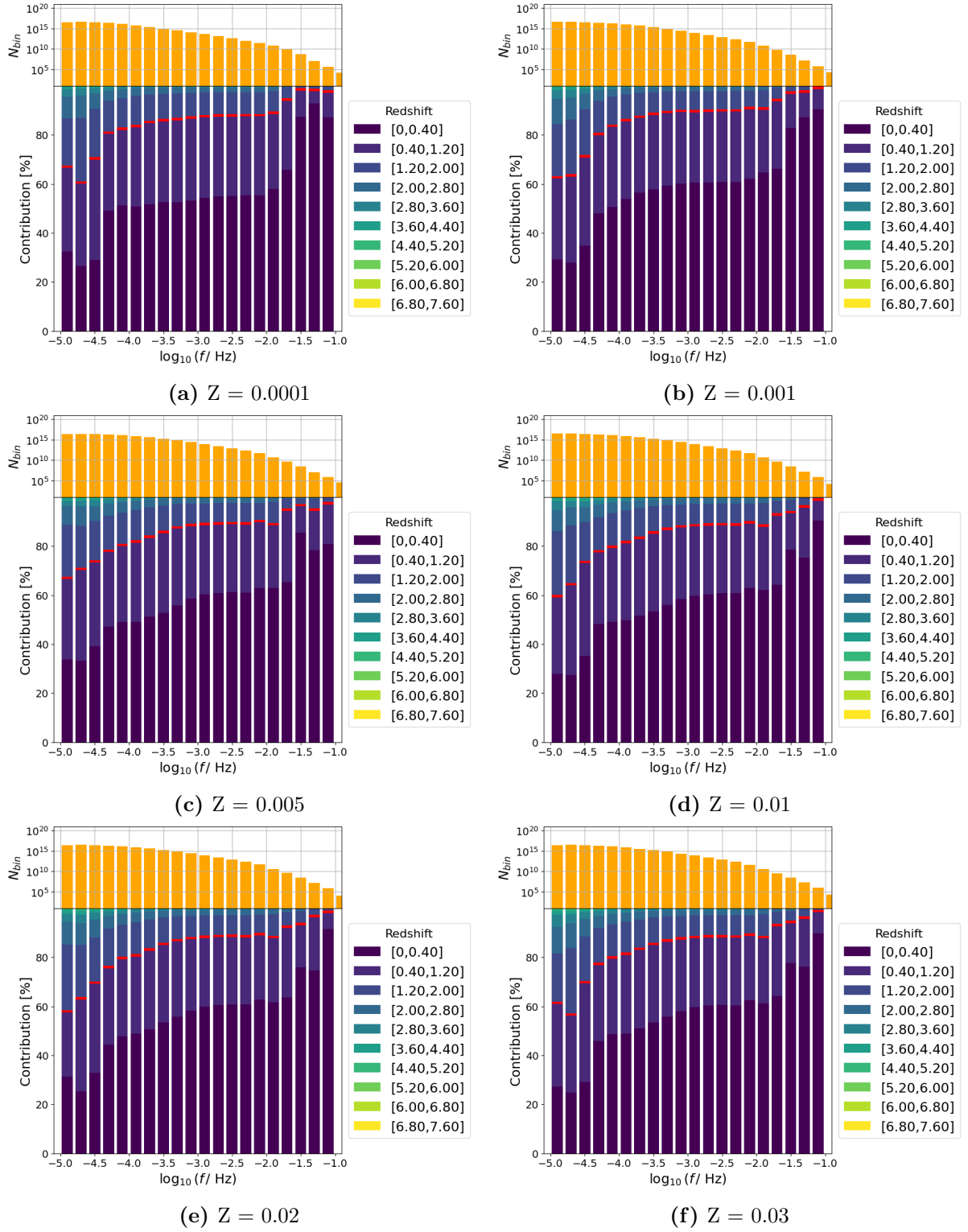


Figure A.3: The bottom panel shows the contribution (in percentage) of each redshift bin to the AGWB signal. The red line represents a redshift of 0.46. The AGWB signal's contribution are binned in 20 frequency bins. The top panel shows the number of systems present in each of the frequency bins, respectively. The population synthesis model plotted here is $\gamma\alpha$ with $\alpha = 1$. The SFH by Madau & Dickinson (2014) was used.



Figure A.4: The bottom panel shows the contribution (in percentage) of each redshift bin to the AGWB signal. The red line represents a redshift of 0.46. The AGWB signal's contribution are binned in 20 frequency bins. The top panel shows the number of systems present in each of the frequency bins, respectively. The population synthesis model plotted here is $\gamma\alpha$ with $\alpha = 4$. The SFH by Madau & Dickinson (2014) was used.

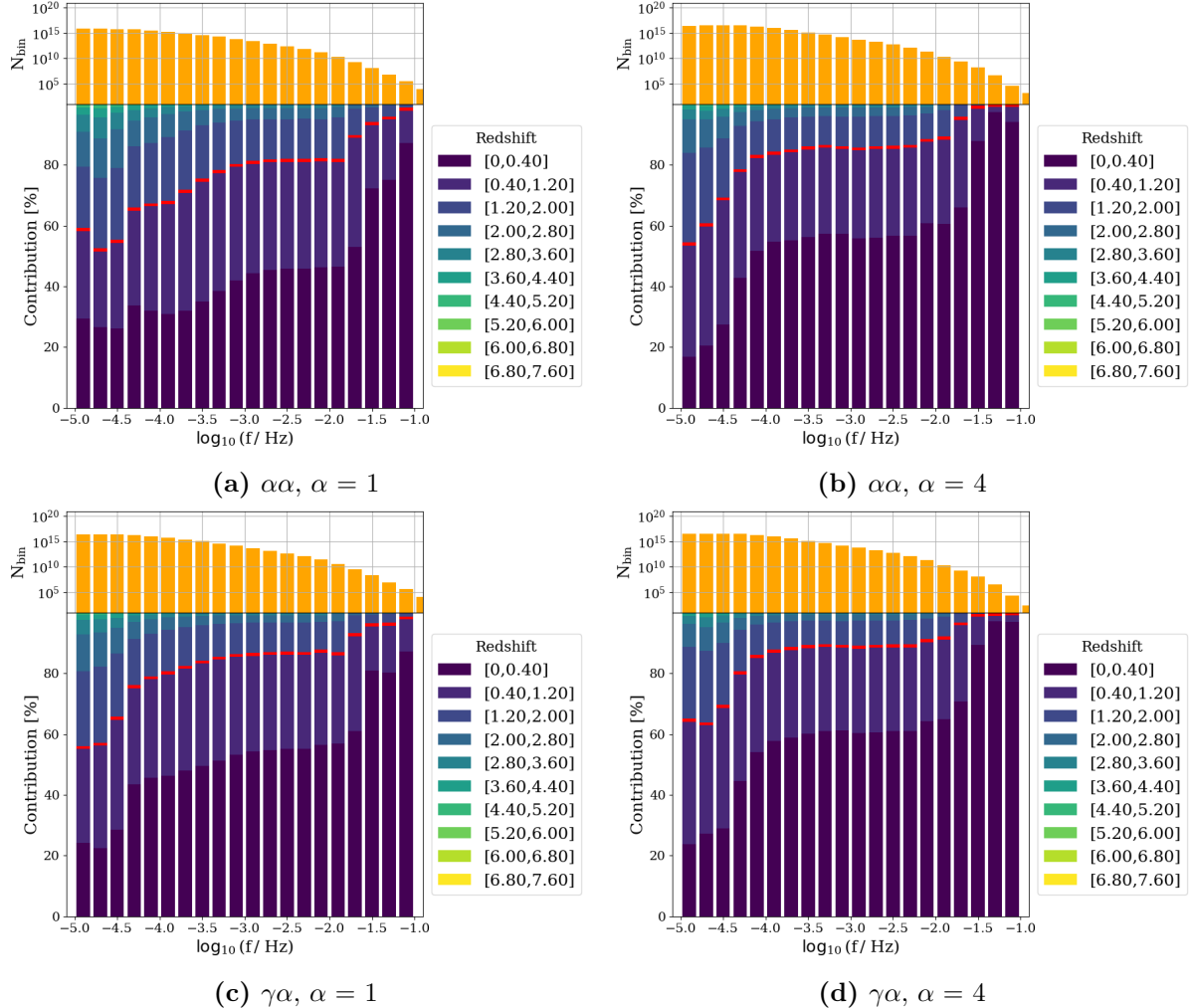


Figure A.5: The bottom panel shows the contribution (in percentage) of each redshift bin to the AGWB signal. The red line represents a redshift of 0.46. The AGWB signal's contribution are binned in 20 frequency bins. The top panel shows the number of systems present in each of the frequency bins, respectively. The four plots show the four population synthesis models when a SFRD model of LZ19 is used.

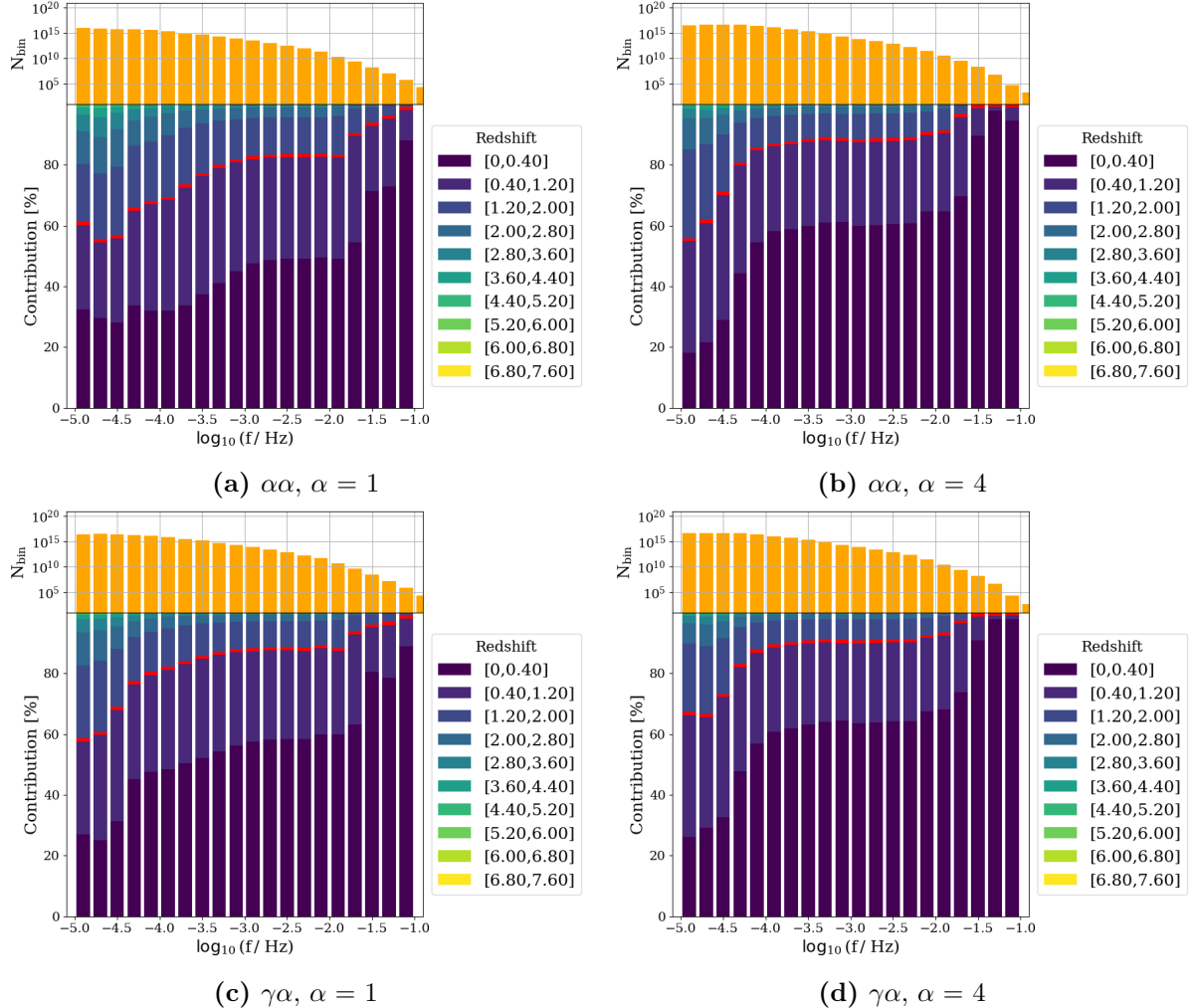


Figure A.6: The bottom panel shows the contribution (in percentage) of each redshift bin to the AGWB signal. The red line represents a redshift of 0.46. The AGWB signal's contribution are binned in 20 frequency bins. The top panel shows the number of systems present in each of the frequency bins, respectively. The four plots show the four population synthesis models when a SFRD model of MZ19 is used.

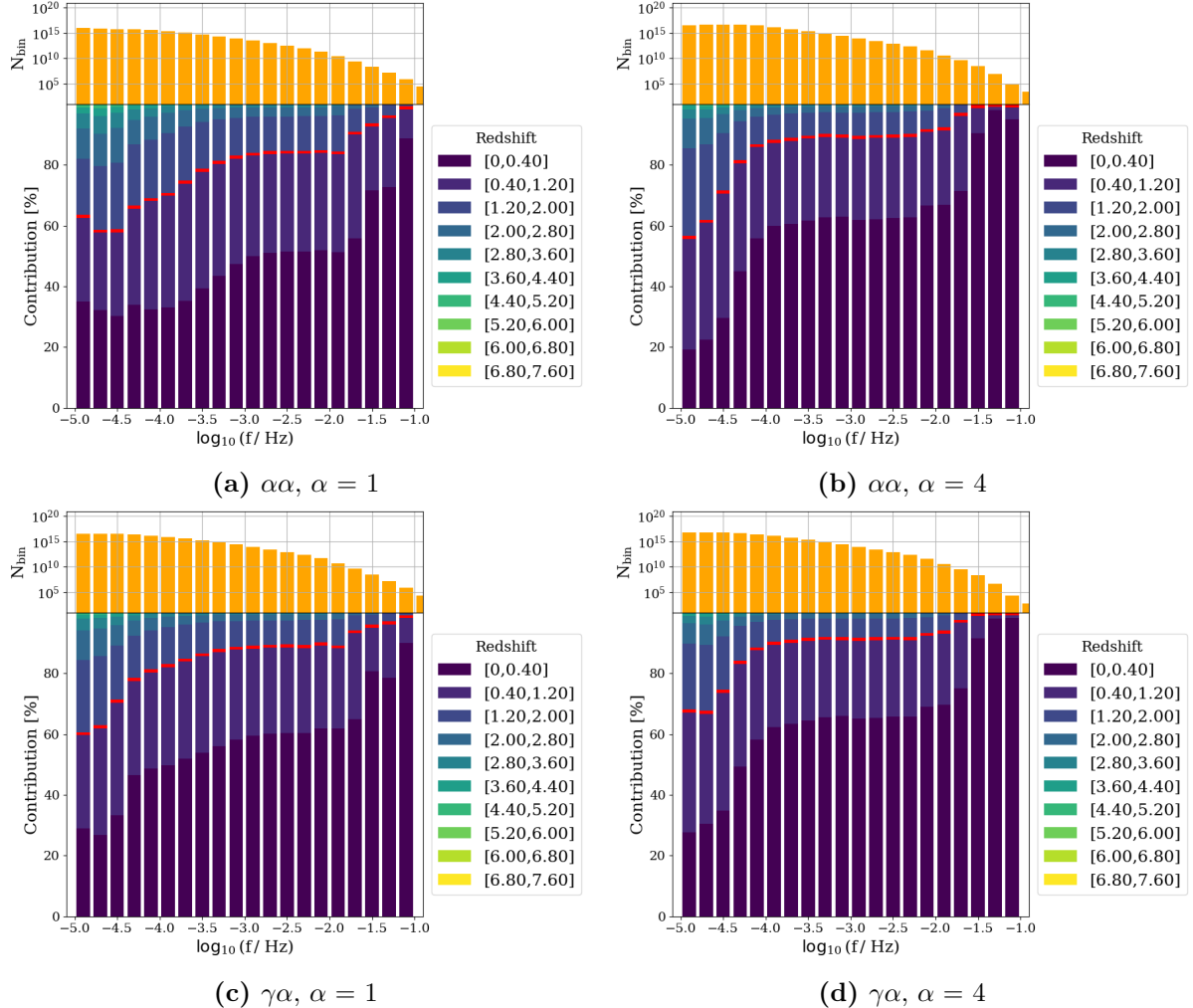


Figure A.7: The bottom panel shows the contribution (in percentage) of each redshift bin to the AGWB signal. The red line represents a redshift of 0.46. The AGWB signal's contribution are binned in 20 frequency bins. The top panel shows the number of systems present in each of the frequency bins, respectively. The four plots show the four population synthesis models when a SFRD model HZ19 is used.

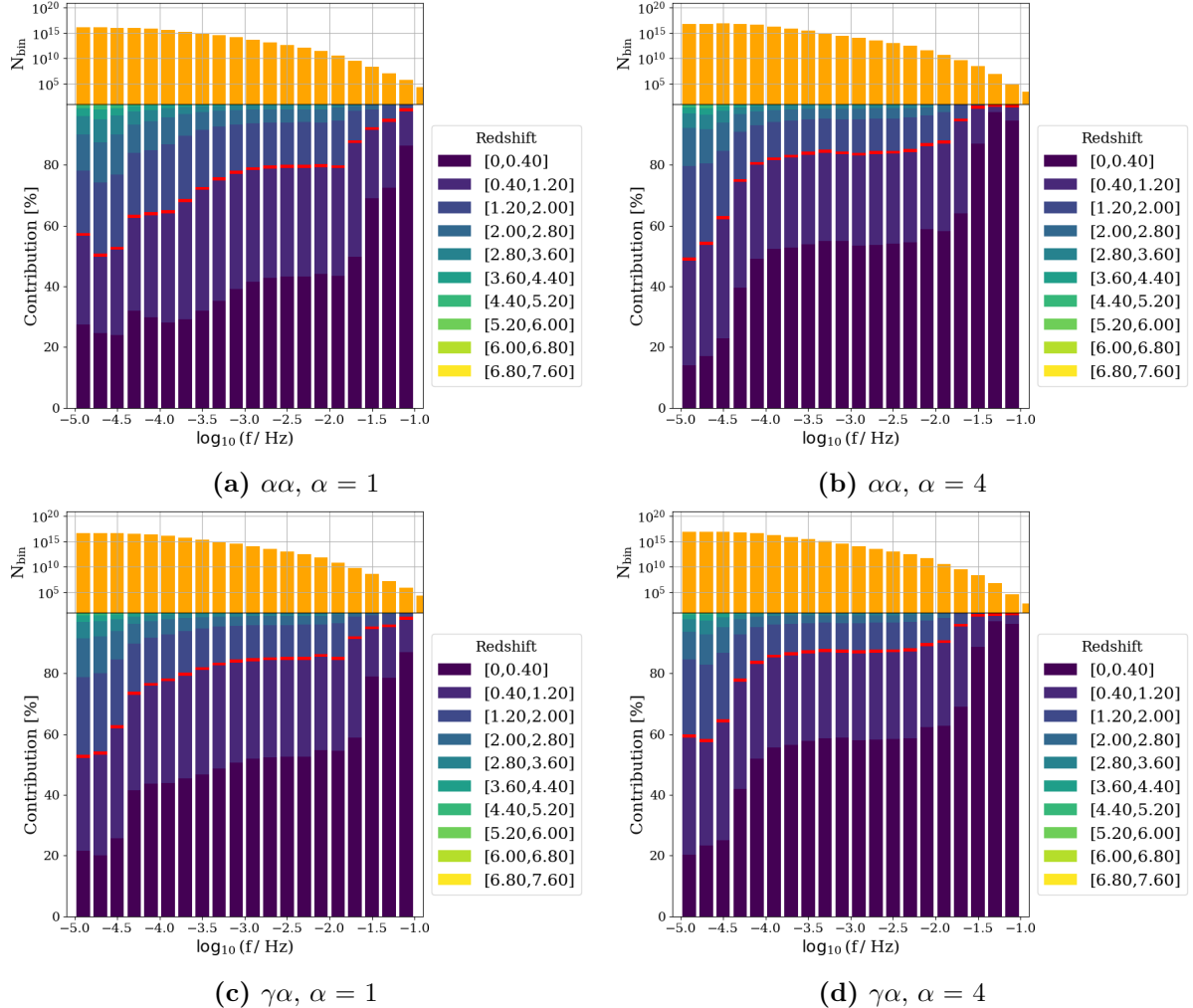


Figure A.8: The bottom panel shows the contribution (in percentage) of each redshift bin to the AGWB signal. The red line represents a redshift of 0.46. The AGWB signal's contribution are binned in 20 frequency bins. The top panel shows the number of systems present in each of the frequency bins, respectively. The four plots show the four population synthesis models when a SFRD model of LZ21 is used.

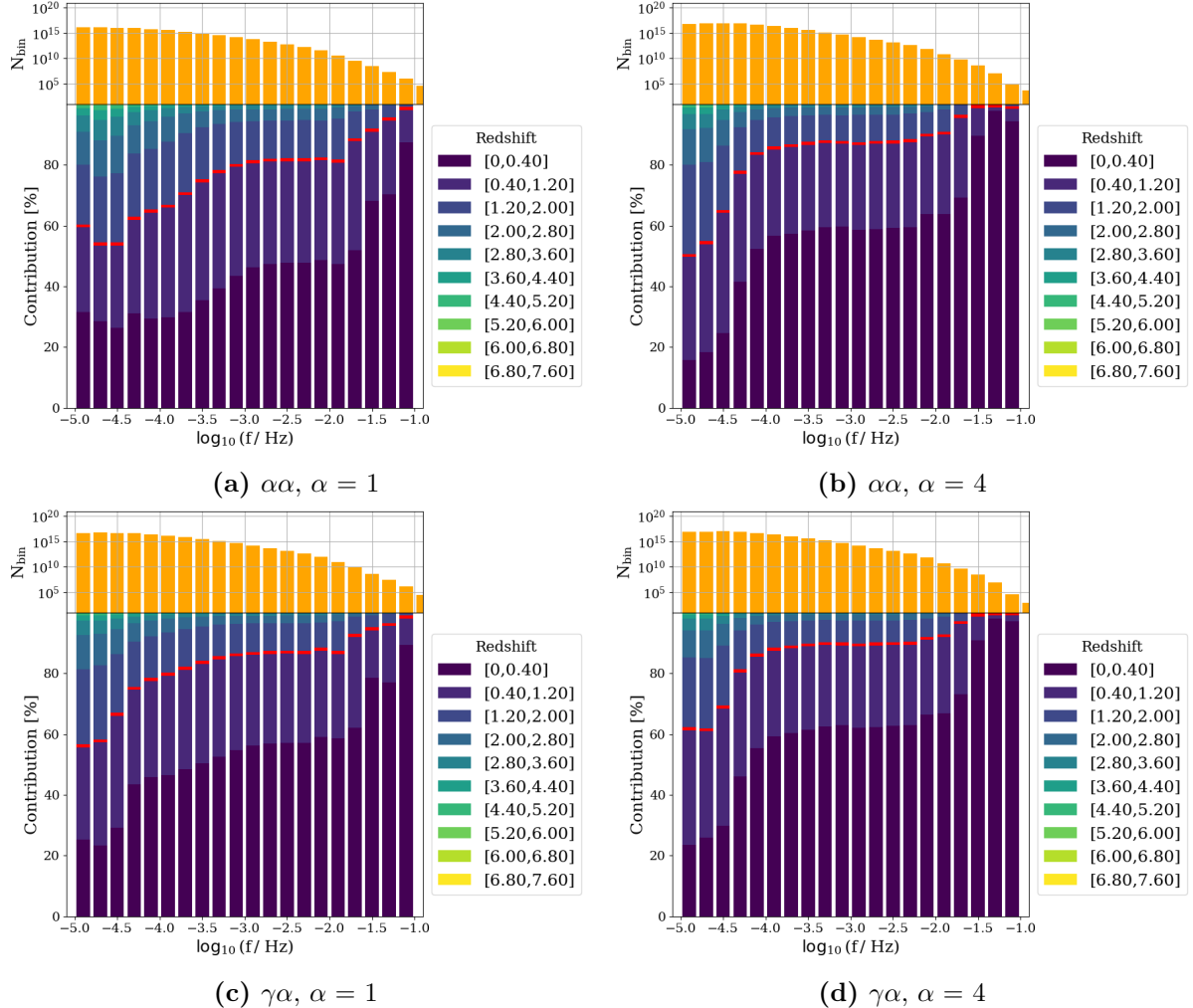


Figure A.9: The bottom panel shows the contribution (in percentage) of each redshift bin to the AGWB signal. The red line represents a redshift of 0.46. The AGWB signal's contribution are binned in 20 frequency bins. The top panel shows the number of systems present in each of the frequency bins, respectively. The four plots show the four population synthesis models when a SFRD model HZ21 is used.

Appendix B

Research Data Management

The data that was used as well as the code used to determine the AGWB and make the plots in this thesis, can be found on: https://gitlab.science.ru.nl/shofman/bwd_agwb